

Article

Mouse-Derived Isograft (MDI) In Vivo Tumor Models I. Spontaneous sMDI Models: Characterization and Cancer Therapeutic Approaches

Peter Jantscheff ^{1,*†}, Janette Beshay ^{1,†,‡}, Thomas Lemarchand ², Cynthia Obodozie ¹,
Christoph Schächtele ¹ and Holger Weber ^{1,*}

¹ In Vivo Pharmacology, ProQinase GmbH, Breisacher Str. 117, 79106 Freiburg, Germany; Janette_Beshay@web.de (J.B.); c.obodozie@proqinase.com (C.O.); c.schaechtele@proqinase.com (C.S.)

² TPL Pathology Labs, Sasbacher Str. 10, 79111 Freiburg, Germany; lemarchand@tpl-path-labs.com

* Correspondence: peter.jantscheff@t-online.de (P.J.); h.weber@proqinase.com (H.W.); Tel.: +49-7666-913-0396 (P.J.); +49-761-769996-1733 (H.W.)

† These authors contributed equally to this work.

‡ Current address: Charles River Discovery Research Services Germany GmbH, Am Flughafen 12-14, 79108 Freiburg, Germany.

Received: 1 December 2018; Accepted: 15 February 2019; Published: 19 February 2019



Abstract: Syngeneic in vivo tumor models are valuable for the development and investigation of immune-modulating anti-cancer drugs. In the present study, we established a novel syngeneic in vivo model type named mouse-derived isografts (MDIs). Spontaneous MDIs (sMDIs) were obtained during a long-term observation period (more than one to two years) of naïve and untreated animals of various mouse strains (C3H/HeJ, CBA/J, DBA/2N, BALB/c, and C57BL/6N). Primary tumors or suspicious tissues were assessed macroscopically and re-transplanted in a PDX-like manner as small tumor pieces into sex-matched syngeneic animals. Nine outgrowing primary tumors were histologically characterized either as adenocarcinomas, histiocytic carcinomas, or lymphomas. Growth of the tumor pieces after re-transplantation displayed model heterogeneity. The adenocarcinoma sMDI model JA-0009 was further characterized by flow cytometry, RNA-sequencing, and efficacy studies. M2 macrophages were found to be the main tumor infiltrating leukocyte population, whereas only a few T cells were observed. JA-0009 showed limited sensitivity when treated with antibodies against inhibitory checkpoint molecules (anti-mPD-1 and anti-mCTLA-4), but high sensitivity to gemcitabine treatment. The generated sMDI are spontaneously occurring tumors of low passage number, propagated as tissue pieces in mice without any tissue culturing, and thus conserving the original tumor characteristics and intratumoral immune cell populations.

Keywords: mouse tumor models; experimental cancer; mouse-derived isografts (MDIs); spontaneous tumors; carcinogen-induced tumors; therapy; immune checkpoint inhibitors; immunocompetent animals; syngeneic

1. Introduction

In the late 1990s and the early 2000s, the blockade of inhibitory immune checkpoint molecules was found to result in the rejection of established tumors and to induce immunity in the secondary exposure to tumor cells [1–5]. These studies led to the stronger focus of experimental studies on the drug development of immune-modulating drugs with syngeneic tumor models in immunocompetent animals. However, the availability of such models is limited to the commonly used murine and cell-line based syngeneic standard tumor models [5].

The establishment of inbred mouse strains in the 1930s, 1940s, and 1950s was an important step in studying the various causes and mechanisms of tumor development as well as new therapeutic approaches in syngeneic animal models [6–8]. These can be divided into three groups: subcutaneous or orthotopic grafts of tumor material into syngeneic animals, physically (e.g., ultraviolet (UV) light) or carcinogen-induced primary tumors, and genetically engineered mice (GEM) reflecting specific cancer genotypes known to be involved in tumor development or therapeutic intervention in patients [9–11]. These models mainly focused on the interaction between the immune system and the developing tumors [6,7,12]. In parallel, these animal models have been used to determine efficacies and toxicities of novel anti-cancer agents before entering clinical trials. Unfortunately, preclinical drug development was often followed by failure in clinical trials [13,14].

In the 1970s, the possibility of transplanting human tumor material into immunodeficient mouse strains [15,16] raised the hope of enhancing the predictability and reproducibility of preclinical results in patients [17,18]. This hope was only partially fulfilled [19]. One important reason for this is the cell line-based approach. The patient's primary tumor tissue was disrupted enzymatically or mechanically and the cells were adapted to grow in artificial tissue culture media. Cells often undergo a process of developing genetic alterations [20]. Based on the selection of *in vitro* cell survival, cell cultures become phenotypically homogeneous with tumor resident stroma cells or proteins interacting with the cancer cells being eliminated [21].

To overcome some of these limitations, in the 1990s, another type of human tumor engraftment was created: patient-derived xenografts (PDXs). Here, solid patient-derived tumor pieces are implanted into immunodeficient mice without prior tissue culture, thus conserving the original tumor characteristics [22]. The tumor pieces include parts of the human stroma [23–26] and are therefore more physiologically relevant [22,27,28]. PDX tumor cells show lower genetic alterations after *in vivo* passaging in mice over multiple generations compared with *in vitro* cell culturing [29–31]. Hence, the implanted tumor tissues generally better maintain the genetic and epigenetic abnormalities found in patients [32]. A remaining limitation of PDX models is the growth of the tumor pieces solely in immunodeficient animals [33], which disables the study of immune-modulating drugs or anti-cancer agents interacting with the immune system [22,29]. Currently, this limitation is overcome by the reconstitution of a functional human immune system in animals, e.g., NOD/SCID or NSG mice [33–35], through the generation of humanized mice [36–38]. Immune or hematopoietic stem cells of various healthy donors, often accompanied by adding fetal thymus or liver cells, are being used for implantation to mimic natural variations in the immune response in patients. However, the high variability and cost renders this model unsuitable for efficacy testing during the early drug discovery phase [39]. Whether the reconstituted, often allogeneic, immune system behaves the same as in the autologous tumor patient has to be addressed [37,40]. The implanted human immune cells may become hyper-activated due to exposure to xenogeneic mouse tissues in a similar fashion as during the alloreactive graft versus host disease [41].

The goal of our present study was to create a cancer model that combines the positive aspects of the current models: the functional immune system of syngeneic mice and the conserved tumor characteristics as well as the wide tumor diversity of PDX. Although mouse and human immune systems may differ in certain aspects [42–46], they display many common and phylogenetically conserved cellular and molecular mechanisms [38,43,44,46]. Therefore, syngeneic models are valuable for the investigation of immunotherapeutic drugs [5,47,48]. This includes the creation of various tumor entities in genetically diverse mouse strains [49–53], for example, in C57BL/6N or BALB/c, prototypically Th1- and Th2-type mouse strains [54–58]. We established a total of 17 new tumor models that were derived from nine spontaneous and eight carcinogen-induced tumors [59] of various immunocompetent mouse strains. The tumors were propagated as tissue pieces in mice only in a PDX-like manner without any *in vitro* tissue culturing, which guarantees mostly conserved tumor characteristics and intratumoral immune cell populations. These models were named mouse-derived isografts (MDIs) and are suitable for studying the interactions between the stroma, immune cells,

and tumor environment in cancer progression, metastasis, and therapy in a completely natural host. The MDI models include adenocarcinomas, carcinomas, sarcomas, or lymphomas.

Here, we outline the establishment and characterization of the spontaneous MDIs and assess their implications for future research. Carcinogen-induced MDIs are introduced in the accompanying paper [59].

2. Results

2.1. sMDI Establishment History

For the establishment of spontaneous mouse-derived isografts (sMDIs), 36 naïve and untreated animals were monitored for more than two years (Figure 1). During the entire observation period, six mice (two female C57Bl/6N, two male C57BL/6N, and two female DBA/2N) were found dead for unknown reasons. Four mice had to be euthanized for ethical reasons other than tumor signs (three with strong skin irritations and one with signs of paralysis). In two (female C3H/HeJ and female albino C57Bl/6N), suspicious tissues (uterus, abdominal cyst, pancreas, diaphragm, or liver) were found and re-transplanted. Tumor growth was only observed for the diaphragm tissue transplants of female C57Bl/6N albino mouse JA-0013 (Figure 2).

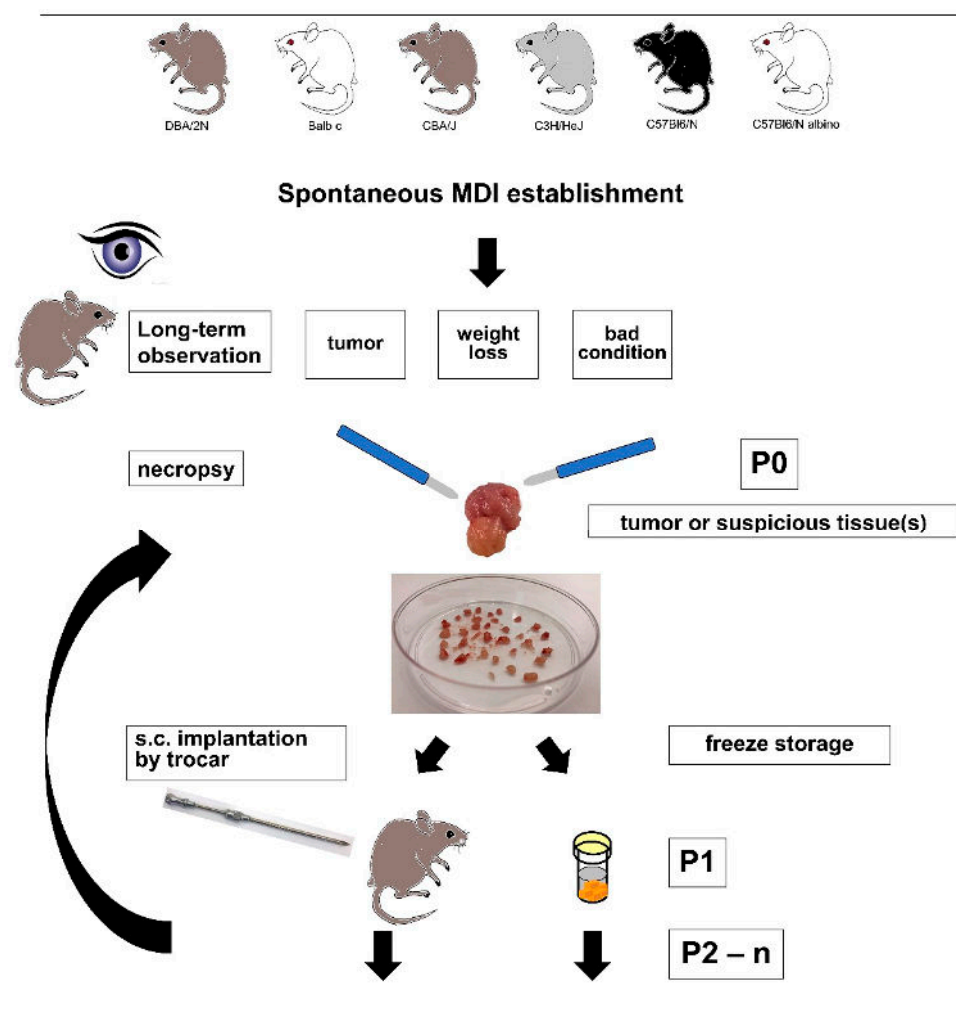


Figure 1. Schematic schedule of spontaneous mouse-derived isografts (sMDI) detection, selection, and establishment. The figure schematically shows the included mouse strains as well as the termination criteria and further handling of the tumor or other suspicious tissue samples. (s.c. = subcutaneous implantation).

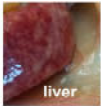




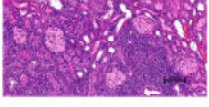

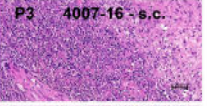


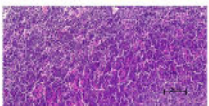


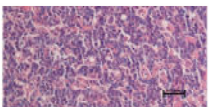


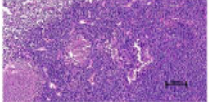
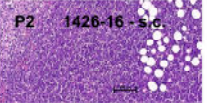
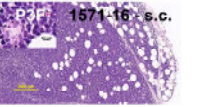
Mouse strain - sex	Tumor name	Diagnosis	Location of appearance in situ	HE staining of primary isolate	HE staining of re-transplanted tumor(s)
DBA/2N ♀	JA-0011	histiocytic Sarcoma (HS) or histiocyte-associated Lymphoma (HAL)	 liver  gut  kidney	  	 P4F 0339-17 - s.c.  P3 4007-16 - s.c.  P5F 0052-17 - spleen
C57BL/6N albino ♀	JA-0013	malignant Lymphoma			 P3 0028-17 - s.c.
CBA/J ♀	JA-0018	malignant Lymphoma			 P1 0113-17 - s.c.
C57BL/6N albino ♂	JA-0034	malignant Lymphoma	no in situ foto 		 P2 1426-16 - s.c.
SCID/bg (C3H/HeJ) ♀	JA-0021	malignant Lymphoma	no in situ foto	SCID/bg THY - nd	 P3F 1571-16 - s.c.

Figure 2. Histopathological characterization of five lymphoma or HAL/HS sMDI. In situ location as well as hematoxylin and eosin (H&E) staining of primary isolated tumor or suspicious tissue and of re-transplanted subcutaneous (s.c.) or spleen tumors (passages P1–P3), or frozen tumor tissue pieces (passages P2F–P5F) were documented by photographs of five hematopoietic sMDIs (JA-0011, JA-0013, JA-0018, JA-0034, and JA-0021). Three tumors were isolated from the gut, liver, or kidney of JA-0011. The histological finding that primary C3H/HeJ isolated lymph node of the sMDI lymphoma named JA-0021 showed a questionable lymphoma or even non-malignant morphology (see Supplementary Materials, Doc.S1-sMDI) indicates that malignant tissue might probably originate from the suspicious, re-transplanted SCID/bg thymus (THY) tissue (HE nd = not done) of the primary recipient H-2^d × H-2^b SCID/bg mouse 1205-16 and not from the primary C3H/HeJ mouse JA-0021. For more details see: Doc. S1-sMDI.

In the other mice, the first tumorous growth was detected after about one year in the female C3H/HeJ mouse JA-0021, which was euthanized for ethical reasons (bad general conditions). Starting from various suspicious tissues (not shown), an enlarged lymph node derived from a female C3H/HeJ mouse was re-transplanted. The transplanted lymph node tissue showed only weak growth in the immunodeficient SCID/bg mouse 1205-16 with a steady state size of 130 mm³ at day 177. At necropsy, an enlarged thymus was found in this mouse. Re-transplanting the SCID/bg thymus tissue led to subcutaneous growth in SCID/bg mice, but not in the C3H/HeJ mice. Re-transplanted primary C3H/HeJ lymph node tissue did not grow anymore and was histologically assessed as a questionable lymphoma or even non-malignant morphology (see below and Doc. S1-sMDI). Consequently, this tumor most probably originated from the re-transplanted thymus tissue of the first SCID/bg recipient.

After about one and a half years, palpable tumors in the left and right region of the axillary lymph nodes were detected in the female DBA/2N mouse JA-0009 (Figure 3). During necropsy, splenomegaly

was also observed in this animal. Transplantation of the tumor tissues led to stable outgrowth between days 21 and 23 in syngeneic mice.


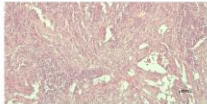


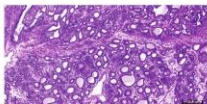


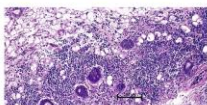
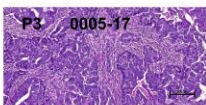

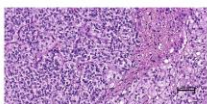
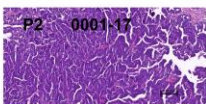

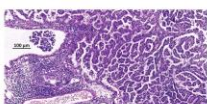

Mouse strain - sex	Tumor name	Diagnosis	Location of appearance in situ	HE staining of primary isolate	HE staining of re-transplanted tumor(s)
DBA/2N ♀	JA-0009	solid invasive Adenocarcinoma (ADC - NOS)			P1 1286-16 
CBA/J ♀	JA-0017	complex Adenocarcinoma/ Mixed Tumor (cADC - MT)			P2F 0096-17 
C3H/HeJ ♀	JA-0023	mammary invasive Adenocarcinoma (ADC - NOS)			P3 0005-17 
	- kidney*	mammary invasive Adenocarcinoma (ADC - NOS)			P2 0001-17 
BALB/c ♂	JA-0032	papillary lung Adenocarcinoma (ADC)			P1 0055-17 

Figure 3. Histopathological characterization of four adenocarcinoma sMDI. In situ location as well as H&E staining of primary isolated tumor or suspicious tissues and of re-transplanted subcutaneous tumors (passages P1–P3), or frozen tumor tissue pieces (passage P2F) were documented by photographs for four selected non-hematopoietic tumor models (JA-0009, JA-0017, JA-0023, and JA-0032). For JA-0023, two malignant primary tissues were isolated from the back and kidney. Original diagnosis of kidney tumor was a clear cell-like renal adenocarcinoma. Re-transplanted kidney tumors (e.g., 0001-17), however, displayed the same histology as the primary back tumor of mammary invasive ADC. For more details see: Doc. S1-sMDI.

Simultaneously, a slowly growing tumor was detected in the left hind leg in the female CBA/J mouse JA-0017. At necropsy, the tumor was completely encapsulated and was about 2 cm in diameter (Figure 3). Frozen tumor pieces displayed stable growth in 12 recipient mice between days 81 and 158 (two animals died for unknown reasons at days 53 and 74).

About one month later, the female DBA/2N mouse JA-0011 had to be sacrificed due to ethical reasons. During necropsy, a suspicious and enlarged liver and kidney as well as a gut tumor were detected (Figure 2). The growth of re-transplanted JA-0011 tissue pieces (ranging from 27 to 72 days) was very aggressive. The gut and kidney tissue showed stable growth. However, in some cases, the transplanted tissue(s) did not grow subcutaneously but massively invaded the spleen and/or liver of the recipient mice. Sometimes, this led to unexpected death without any signs of previous heavy tumor burden in the animals. The invaded spleens and livers showed similar histopathology to the primary and subcutaneous tumors (Figure 2). These tissues were successfully re-transplanted.

Another month later, the male C57BL/6N albino mouse JA-0034 had to be sacrificed due to ethical reasons. Different suspicious tissues (gut, liver, lymph nodes, spleen, and salivary gland tissue) were detected during necropsy (Figure 2). Various re-transplanted tissue pieces of JA-0034 grew in the recipient mice. Gut tissue displayed the most homogeneous growth (about 45 days) and was not pursued any further.

Twenty-three months after starting our observations, a big node was palpated on the back of the female C3H/HeJ mouse JA-0023. During necropsy, the tumor was found to be a blood-filled cyst (Figure 3). The tissue was re-transplanted and grew between days 29 and 45 with moderate final

tumor volumes of less than 1000 mm³ and again displayed a blood-filled, cyst-like phenotype in three out of seven recipient animals. In parallel, a solid kidney-enveloping tumor was detected in JA-0023 (Figure 3). After re-transplantation, tumor pieces grew well within 60 days and reached tumor volumes of more than 1000 mm³ in the recipient mice.

Due to significant weight loss and general bad condition, a male BALB/c mouse JA-0032 was sacrificed after two years of observation and a necropsy was performed. Both lungs displayed large solid tumors that grew 45–59 days after re-transplantation in syngeneic animals (Figure 3).

Another month later, the female CBA/J mouse JA-0018 displayed noticeable respiratory problems and was terminated. Different suspicious tissues (lung metastases, enlarged lymph nodes, spleen, and genitourinary tract tissue) were detected during necropsy (Figure 2). Various re-transplanted tumor tissues of JA-0018 grew in recipient mice. The most stable outgrowth (about 60 days) was found with lung metastatic tissue, which was not pursued any further.

The mouse strains, sex, tumor types, and general growth characteristics of the established sMDI models as well as the general histopathological diagnoses are summarized in Table 1 and Figures 2 and 3.

During the studies that lasted for more than two years (total observation time was about 28 months), nine sMDI tumors were finally established, i.e., a stable re-transplantation into syngeneic recipients was performed using frozen tumor pieces. Suspicious tissues were detected and the primary isolates were re-transplanted in seven other mice (female BALB/c, female C57BL/6N albino, female C3H/HeJ, male C57BL/6N, male BALB/c, male BALB/c, and male C57BL/6N albino). The tumor and tissue pieces were frozen until further use. Therefore, in about 16 of the 36 investigated mice, primary spontaneous malignant growth was observed. However, in the latter seven cases a stable outgrowth of potential frozen sMDI samples has to be verified as the basis for further development.

2.2. sMDI: Histological and Pathological Analysis

To characterize the pathological phenotypes of sMDIs and to verify their phenotypic stability after several rounds of re-transplantation, a hematoxylin and eosin (H&E) stain was performed on the tissue sections. For this purpose, primary isolates (tumor or suspicious tissue) and subcutaneous follow-up re-transplants were compared. Whether the tumor/suspicious tissues from the primary isolates actually represented the primary tumor or secondary metastatic tissue could not be determined for most cases. Therefore, the organ of origin remains to be determined, for example by immunohistochemistry or other methods, in future studies. Histologically, we differentiated two main groups of sMDI solid tumor models: of hematopoietic or of non-hematopoietic origin (Table 1). Figure 2 summarizes four various lymphoma sMDIs and one histiocytic sarcoma/histiocyte-associated lymphoma (HS/HAL) model, whereas Figure 3 shows four adenocarcinoma (ADC) sMDI (JA-0023, with two different primary localizations) models in various mouse strains. Single models are described below.

Table 1. Established spontaneous mouse-derived isograft (sMDI) models, summarizing the characteristics of established sMDIs.

Spontaneous MDI										
Tumor Name	JA-0009	JA-0011	JA-0013	JA-0017	JA-0018	JA-0023		JA-0032	JA-0034	JA-0021
						(back)	(kidney)			
Hematopoietic (y/n)	no	yes (?)	yes	no	yes	no	no	no	yes	yes
Histopathological Diagnosis	low differentiated ADC	HS or HAL	malignant lymphoma	ADC	malignant lymphoma	mammary invasive ADC	clear cell-like ADC of kidney	papillary ADC lung	malignant lymphoma	malignant lymphoma
Mouse Strain	DBA/2N	DBA/2N	C57BL/6N albino	CBA/J	CBA/J	C3H/HeJ	C3H/HeJ	BALB/c	C57BL/6N albino	thymus (THY) SCID/bg 1205-16
Sex	♀	♀	♀	♀	♀	♀	♀	♂	♂	♀
Estimated Growth Time (In Days)	21–23	27–72 problem: liver-/splenomegaly	45	81 to ≥158	60	29–45	60	45–59	45	24
Included Animals	growth curve (12) *	frozen/directly (12/10) *** Pool §	frozen (11) **	growth curve (12)	frozen/directly (3/3)	growth curve (12)	frozen/directly (3/4)	growth curve (12)	frozen (12) only gut	frozen/directly (3/6) only SCID/bg
Take Rate	92% 11/12	63% 14/22 &	100% 11/11	75% 9/12	100% 6/6	100% 12/12	71% 5/7	66% 8/12	92% 11/12	78% 7/9
Appearance (AP) Day	6–7	nd	nd	49–56	nd	13–20	nd	31–41	nd	nd
Real Running Time (RRT) Day (% Alive Animals)	21 (75%) 23 (67%)	nd	nd	81 (58%) 105 (50%)	nd	29 (92%) 45 (42%)	nd	45 (67%) 59 (42%)	nd	nd has to be done in H-2 ^a × H-2 ^b hybrid mouse

Tumors were of non-hematopoietic (no) ADC and hematopoietic (yes) HS/HAL or lymphoma origin from various mouse strains. In the case of tumor JA-0023, two histopathologically different original tumors that were initially back- and kidney-derived were observed. Estimated growth time is the mean (or range) of tumor growth until termination of at least 12 tumor-bearing animals * using frozen tumor pieces (growth curves). In the hematopoietic and the JA-0023 kidney ADC models, ** growth times were calculated from the outgrowth of frozen tumor pieces in various experiments (or if the number of these animals was six or less) of *** frozen or directly re-transplanted tumor pieces. The number of animals is provided in brackets. The take rates reflect the percentage of the animals of respective models developing a tumor within the estimated growth time. In the case of JA-0011, a HS/HAL, a § pool of primary kidney and gut tumor isolates grown on the left and right flank in the DBA/2 mouse 1307-16 was used. Since several animals did not show local s.c. tumor growth but developed spleno- and/or hepatomegaly causing death, a & higher number of animals was included to calculate the take rates. In the case of lymphoma JA-0034, suspicious tissues from a different origin grew, but the most stable outgrowth was observed with tissue initially isolated from a gut tumor (used here). *Appearance* is defined as the earliest time point(s) allowing for robust randomization at mean tumor volumes between 40 and 150 mm³ in re-transplanted animals. *Real running time (RRT)* determines the time difference from implantation to the time point when the remaining animal number reaches ~60% of the starting group size. Therefore, it defines the *treatment time window (TTW)*, i.e., the maximal time range to treat animals after randomization (AP) to the potential study end. This allowed us to calculate the realistic study length as well as necessary group size for statistically reliable analysis for testing the anti-cancer agents. Grey columns are not yet characterized by growth curves (below-6) or the tumor grows only in another mouse strain or because is of other strain origin (1), or differentiates hematopoietic (grey) and non-hematopoietic tumors.

2.2.1. Hematopoietic Tumor Models

Tumor JA-0011/and others (Figure 2, Doc. S1-sMDI–page 15 ff) was indexed as a histiocytic sarcoma (HS) or histiocyte-associated lymphoma (HAL) in several tissues (liver, gut, reproductive tract, kidney, and spleen), with both histiocytic and lymphocytic components. Re-transplanted subcutaneous tumors 0339-17, 4007-16, or 0057-17 (Figure 2, Doc. S1-sMDI) also invaded the spleens or livers of recipient mice, e.g., 0052-17 or 1298-16, and displayed a similar histopathological outcome, except for case 1298-16 which had features of malignant lymphoma. Hence, in two re-transplanted cases, a phenotypical HAL (1298-16) and a very typical HS (0052-17) with minimal lymphoid component were diagnosed from the primary index HS/HAL case. To determine any actual HS/HAL phenotype drifting, immunohistochemistry has to be performed in future experiments [60]. Tumors showed partially extramedullary hematopoiesis and a significant infiltration of neoplastic cells by polymorphonuclear leukocytes (neutrophils and eosinophils), lymphoid cells, or lymphoma-like appearance with abundant histiocytic and macrophagic recruitment.

The phenotype of tumor JA-0013/0028-17 (Figure 2, Doc. S1-sMDI–page 23 ff) was most consistent with malignant lymphoma, which were probably of B-cell lineage with the presence of cells differentiating towards a plasma cell phenotype and presence of few Mott cells containing Russell bodies. Another re-transplanted tumor, 0027-17, had a few uncommon non-neoplastic multinucleate giant cells and syncytial macrophages leading us to suspect an opportunistic infection or alternatively histiocytic differentiation, thus possibly displaying characteristics of a histiocytic lymphoma. Special stains are necessary for a definitive diagnosis of this particular case.

The female CBA/J-derived tumor JA-0018/0113-17 tissue was isolated from the lung, and was probably a secondary localization, since it was characterized as a malignant lymphoma. The same histology was observed in the re-transplanted tumors. Primary in situ location, typical H&E stains of tumor tissues, and primary diagnoses are shown in Figure 2 and Doc.S1-sMDI–page 28 ff.

In index case JA-0034/1426-16 (Figure 2, Doc. S1-sMDI–p32 ff) of a lymphoma, minimal phenotypic differences were observed between the primary and secondary tumors. Original and daughter tumors invaded into adjacent and/or adipose tissues. For further lineage definition (B cells versus T cells versus other), characterization by immunohistochemistry has to be used.

In the case of tumor JA-0021/1571-16, re-transplanting suspicious thymus tissue from primary host animal 1205-16 resulted in further growth in SCID/bg mice. Histology represented a malignant lymphoma in the thymus-derived s.c. tumors, which suggests the origin of the sMDI lymphoma named JA-0021 as the SCID/bg mouse 1205-16 thymus and not the C3H/HeJ lymph node which showed a questionable lymphoma or even non-malignant morphology in the skin mammary teat (see Doc.S1-sMDI–page 32 ff).

2.2.2. Non-Hematopoietic Tumor Models

Female JA-0009 DBA/2N mice displayed enlarged axillary lymph nodes and splenomegaly. Despite the gross aspects of this index mouse at necropsy suggesting a hematopoietic tumor, an adenocarcinoma (ADC) was diagnosed.

The epithelial origin of these tumors (see also JA-0009/1286-16, Figure 3, Doc.S1-sMDI–page 36 ff), was most likely exocrine, such as mammary gland (breast), apocrine sweat, or possibly less likely pancreas, salivary, prostate, or other epithelium, with adenoid or tubular structures such as what could be observed in the lung, bile duct, airways, or kidney. Invasion of more neutrophils than small lymphocytes in the carcinomatous tissue was observed. Both samples showed infiltrative growth, low to moderate stroma host response, coagulative and disintegrative but overall minimal grade necrosis, and occasional abortive mitosis (mito-necrosis) with abnormal spindle (mitotic index: 3.2). There were areas of neoplasia, suggesting an epithelium to mesenchymal transition and cytoplasmic eosinophilia possibly being epidermoid differentiation, which would have to be confirmed by immunohistochemistry.

Index case JA-0017/0096-17 (Figure 3, Doc. S1-sMDI–page 41 ff) an ADC seemed upon first analysis to exhibit some significant degree of phenotypic drifting. Tumors derived from the two daughter mice (1234-16 and 0096-17) were morphologically different. However, the primary index complex type ADC was a mixed cell tumor (of glandular and myoepithelial components) with two neoplastic differentiations. Thus, the re-transplanted tumors might have had various degrees of each of the two components, which could be further characterized using immunohistochemistry.

Different histological diagnoses of index case JA-0023 (Figure 3, Doc. S1-sMDI–page 45 ff) were obtained for growing primary tumors with either mammary invasive ADC in JA-0023 (back tumor) and a possible clear cell-like adenocarcinoma (CCA) in JA-0023 (kidney tumor) mimicking renal clear cell carcinoma in humans (Doc. S1-sMDI–page 46). The re-transplanted tumors of the kidney sMDI, e.g., 0001-17, had a morphology very similar to the mammary index tumor of the back JA-0023 as well as its daughter sMDI 0005-17 (Doc. S1-sMDI–page 48). Therefore, the tumor of origin was likely a mammary ADC. The primary JA-0023 back tumor may mimic a CCA by invading the kidney tissue, or alternatively are 2 different tumors of 2 distinct cell origin (renal tubular cells vs. mammary gland cell). Nevertheless, the index subcutaneous tumor, which was invading vessels and developed from mammary gland and invading into the sub-cutaneous adipose tissue with intense lymphoid infiltration, was also characterized by a lineage with invasive properties and vascular embolization and mild to moderate peripheral mononuclear cell infiltration, mostly by lymphoid cells.

One exception regarding the conserved original tumor characteristics as well as intratumoral immune cell populations after re-transplantation seemed to be tumors JA-0032 and 0055-17 (Figure 3, Doc. S1-sMDI–page 55 ff). The original sample was identified as a typical bronchioloalveolar papillary adenocarcinoma invasive in bronchus associated lymphoid tissue, whereas the daughter tumor was a solid trabecular adenocarcinoma with clear cells (cuboidal jointed cells with clear cytoplasm in 0055-17) with small areas of columnar cells, exactly like the index case. The primary proliferative alveolar tissue of JA-0032 invaded the nearby main bronchus. The alveolar walls were obscured by the proliferative tissue. The delicate stroma induced by the neoplastic tissue was variably thickened by collagenous tissue and infiltrated by moderate numbers of small mononuclear cells. In contrast, a solid and very fragile (due to nearly absent supportive stroma and secondary tearing and hemorrhage) proliferation of mid-sized polyhedral to cuboidal epithelial cells was observed in the 0055-17 sMDI with a characteristically clear (rarefied) cytoplasm. Anisopoikilocytosis and nuclear variability was slight to moderate. These differences have to be further analyzed and confirmed by immunohistochemistry, but a likely explanation is type 2 pneumocyte differentiation with surfactant in a heterotopic subcutaneous localization.

More detailed histopathological characterization, as well as larger microphotographs of hematopoietic as well as ADC sMDI models, are shown in Doc. S1-sMDI. Preliminary assessment of the histological analysis of the host stroma reaction and the inflammatory response including the tumor infiltrating leukocyte index (Doc. S1-sMDI) of some of the sMDI models indicated that sMDI tumor models might be categorized into the recently defined “inflamed” and “noninflamed” tumor immune infiltrate phenotypes [5,61,62]. This was confirmed and refined by flow cytometry and RNA-Seq analysis of sMDI JA-0009.

2.3. sMDI: Take Rates and Growth Curves

After the model was established, the growth curves and take rates of frozen tumor pieces in four ADC sMDI models (JA-0009, JA-0017, JA-0023 (back), and JA-0032) were determined (Table 1, Figure 4). In contrast, the probable growth times and take rates of the other five established hematopoietic models were calculated from subsequent experiments of various frozen or directly re-transplanted tumor pieces (Table 1). In order to also use the hematopoietic models in efficacy studies, first, their exact growth curves and take rates were determined.

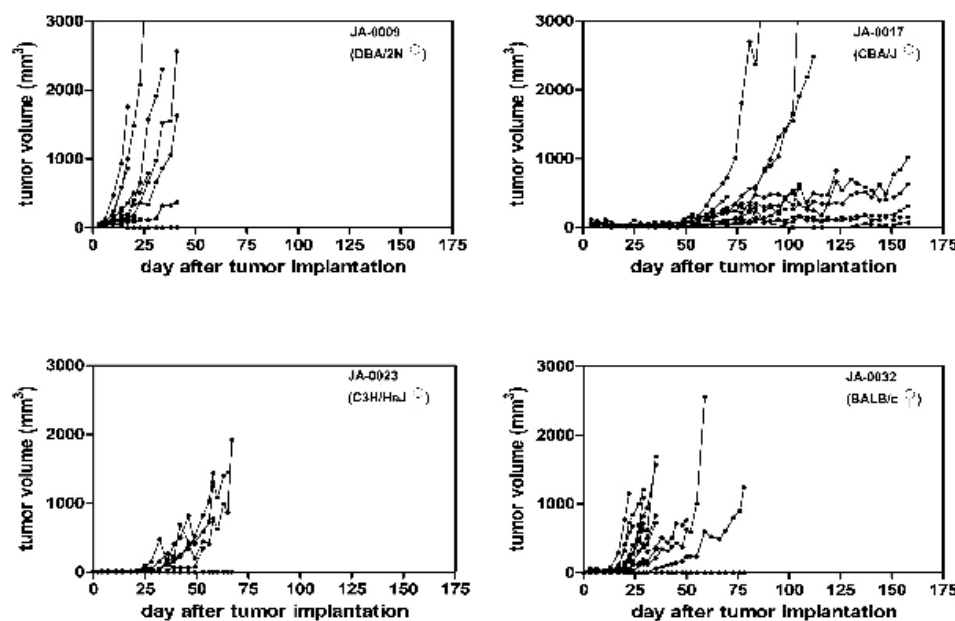


Figure 4. Take rates and growth curves of the selected sMDI models. Growth curves of 12 individual mice each implanted with previously frozen tumor pieces are shown for the sMDI models JA-0009, JA-0017, JA-0032, and JA-0023 (with tissue originating from a primary back tumor) in syngeneic female DBA/2N, CBA/J, BALB/c, and C3H/HeJ mice, respectively. Tumor growth was measured twice weekly with calipers.

The growth curves of the four ADC models, JA-0009, JA-0017, JA-0023 (back), and JA-0032, showed very variable individual tumor growth periods within 21–23, 81–158, 29–45, and 45–59 days, respectively, and take rates varying from 66 to 100% (Table 1, Figure 4). *Appearance (AP)*, i.e., the earliest time points allowing robust randomization at mean tumor volumes between 40 and 150 mm³ in the 12 (or less, depending on the take rate) animals varied from 6–7, 49–56, 13–20, and 31–41 days, respectively (Table 1, Figure 4). The resulting observation period and *treatment time window (TTW)*, were not simply the difference between *appearance* and the determined tumor growth period. Since a varying quantity of animals in the single tumor models had to be sacrificed due to fast tumor growth or ulcerations (ethics), or were found dead for unknown reasons, the number of alive animals had already critically decreased before the end of the growth periods. Therefore, we defined *real running time (RRT)* of the models. *RRT* determines the time difference from implantation to the time point when the remaining animal number reaches ~60% of the starting animal group size. Therefore, *RRT* defines *TTW*, i.e., the maximal time range to treat animals after randomization (*AP*) to the potential study end. This allowed us to calculate the realistic study length as well as the necessary group size for statistically reliable analysis for testing, such as the immune checkpoint inhibitors. For the four ADC sMDI models, we outlined potential study endpoints, with *RRTs* (and actual *TTWs*) of about 21–23 (15–16), 81 (25–31), 29 (9–16), or 45 (4–14) days (Table 1).

The models were characterized by variable growth periods and variable growth properties. Heterogeneous growth was impressive in the case of the two slow growing models, JA-0017 (take rate 75%) and JA-0032 (take rate 66%). In both models, some tumors appeared to be slow growing while others grew fast or moderate. It remains unclear if these properties reflect differences between re-transplanted tumor pieces, between individual mice, or if they are caused by chance. The heterogeneous tumor growth allowed us to include at least 6–9 mice from 12 animals after randomization to study the efficacy of anti-tumor treatments in both sMDIs. Models JA-0009 and JA-0023 (back) grew within 21–23 and 29–45 days, respectively, and were more homogeneous (Figure 4). Thus, sMDI JA-0009 was chosen for further detailed model analysis by flow cytometry, RNA-Seq, and efficacy studies.

2.4. sMDI: Flow Cytometric Analysis

The material of re-transplanted and outgrown JA-0009 was isolated and processed for flow cytometry analysis. Obtained single cell suspensions were stained with master antibody mixes for T cell panel, myeloid cell panel, and macrophage cell panel. Results of the flow cytometry analysis are shown in Figure 5A.

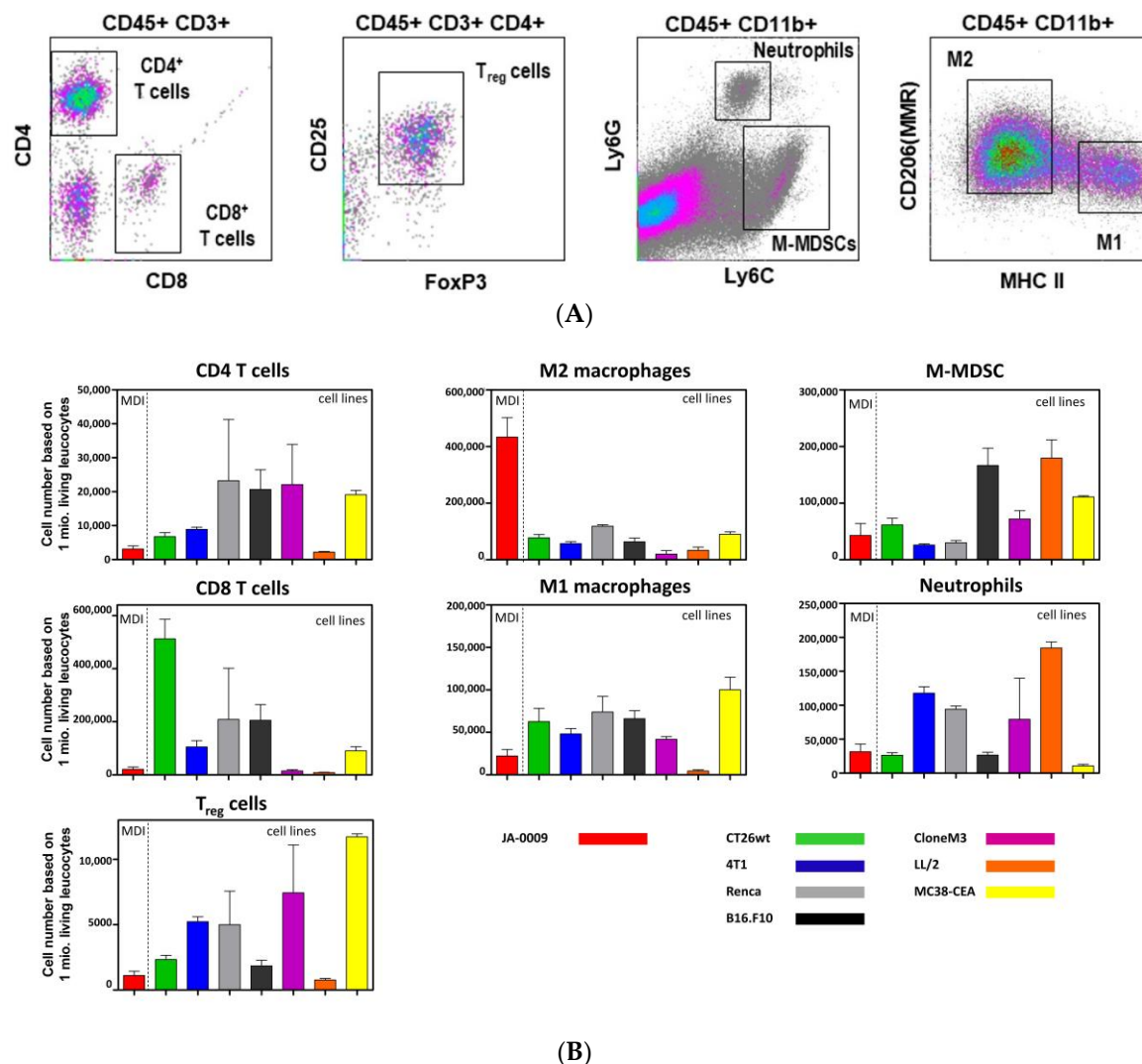


Figure 5. (A) Flow cytometric analysis of tumor infiltrating leukocytes (density dot plots) in sMDI JA-0009. Representative flow cytometry blots of tumor infiltrating CD4⁺/CD8⁺ T-cells, Treg cells, M-MDSCs, neutrophils/G-MDSC (cells of CD11b⁺, Ly6G⁺, Ly6G^{int} phenotype), and M1/M2 macrophage subpopulations isolated from untreated syngeneic adenocarcinoma mouse model JA-0009 sMDI. M-MDSC = monocytic myeloid-derived suppressor cells, MMR = macrophage mannose receptor, Treg = regulatory T cells. (B) Quantitative flow cytometric analysis of tumor infiltrating leukocytes in sMDI JA-0009 in comparison to seven cell-line based syngeneic standard tumor models. The flow cytometry analysis of tumor infiltrating leukocytes in sMDI JA-0009 was compared to seven established cell-line based syngeneic mouse standard models for CD4⁺/CD8⁺ T-cells, M-MDSCs, neutrophils, M1/M2 macrophages, and Treg cell subpopulations were isolated from the untreated tumor tissue. For the antibodies and procedure used here, see Materials and Methods. The graphs depict the number of cells of each subpopulation per 1×10^6 living leukocytes. Further information regarding the used cell line-based syngeneic standard tumor models is provided in Doc. S2-sMDI and Figure S2-sMDI.

A quantitative comparison of the immune cell subpopulations in sMDI JA-0009 and the established cell line-based syngeneic standard in vivo tumor models (MC38-CEA, CT26.WT, LL/2, Clone M3, 4T1, RENCA, B16.F10) is shown in Figure 5B. The most striking difference between the newly established sMDI JA-0009 and all other formerly tested syngeneic standard models was a massive infiltration of M2 macrophages and a low T cell number, especially of CD8⁺ T cells.

2.5. sMDI/cMDI: Preliminary Results of RNA-Seq

RNA-isolation and RNA-Seq were performed by StarSeq (Mainz, Germany) as whole transcriptome shotgun sequencing analysis (Materials and Methods) of two samples each of sMDI JA-0009 as well as of cMDI JA-2011 and JA-2042, two carcinogen-induced sarcomas [59]. RNA-Seq analysis was mainly conducted to obtain an overview of the target expression for potential new drug development and to identify potential mutations.

As mentioned in Section 2.2, the definite tissue origin of the most outgrowing MDI tumor models could not be identified. Therefore, the gene expression pattern determined by complete RNA-Seq whole transcriptome shotgun sequencing analysis will also provide an additional tool—together with the histological data—to better localize the tumor tissue origin, e.g., by a comparison with the gene expression in different tissues of normal mice available from the mouse ENCODE transcriptome data (METD) database [63] or immunohistochemistry. However, this will be the subject of future investigation. Missing identification of the tumor origin complicated the search for tumor-specific changes related to the respective initial normal tissues.

Therefore, as a first step, the expression profiles of various genes of only three gene families related to tumor malignancy or anti-tumor immune response were created: tyrosine kinase receptors, immune population markers, and an IFN- γ signature, which was composed of multiple interferon-responsive genes involved in innate and adaptive immune activities. The gene expression profiles displayed striking differences in the absolute as well as relative expression patterns ≥ 500 -fold for the various genes of one gene family (Table S1a–c, Figure S1 a_{i–iii}, and Figure S1 b_{i–iii}) within the individual tumor model (sMDI ADC JA-0009 and the two cMDI sarcomas, JA-2011 and JA-2042).

A direct comparison of gene expression between the individual MDI models was not possible since the FPKM (fragments per kilobase million) values were not determined in simultaneous experiments. However, comparing the individual gene expression related to one common internal, low expression reference gene (Figure S1 b_{i–iii}) showed different expression patterns within each MDI, not only when comparing sMDI ADC JA-0009 and the two cMDI sarcomas JA-2011 and JA-2042, but also between the cMDIs themselves (Table S1a–c; Figure S1 b_{i–iii}). The IRE (internal relative expression) gives one an impression on the strength and variabilities of single gene expression within one gene family of the individual MDI models. This indicates that the relative expression of single genes is different in the individual MDI tumor models; e.g., with an overexpression of Met, CD44, or Ly6C in sMDI JA-0009, of Irf1 in cMDI JA-2011, or Cd4, Axl and Ccl5 in cMDI JA-2042 (Figure S1 b_{i–iii}, and inserts). However, whether these differences are model-, tissue-, or mouse strain-specific remains unclear at the moment.

Therefore, RNA-Seq data further supported or confirmed findings already obtained by other methods. For example, the high CD44 gene expression (mean FPKM: 186.078) of the immune population marker gene family in sMDI JA-0009 (Figure S1 a_{i–iii}, and Figure S1 b_{i–iii}) well agreed with the strong intratumoral invasion of M2 macrophages found by the flow cytometry analysis (Figure 5B). The high expression of Ly6C in the same gene family supports the histological finding of the possible mammary origin of this tumor (METD database [63]). Similarly, CD4 expression was found to be enhanced in cMDI JA-2042 (Inserts Figure S1 a_{i–iii}, and Figure S1 b_{i–iii}), confirming the flow cytometry data showing a strong CD4⁺ T cell infiltration in this cMDI (Figure 4 in Beshay et al. [59]). This relatively high CD4⁺ T cell infiltration might also be responsible for the moderate effects regarding the immune checkpoint inhibitors observed for JA-2042, and displayed a significant tumor reduction by a combination antibody treatment [59]. In contrast, the data do not provide any evidence what might cause the resistance to antibody treatment e.g., in ICPI non-responder JA-2011.

The preliminary data confirmed that RNA-Seq could generally be used to address various questions regarding MDI tumor models. A more detailed characterization of the gene expression of the whole transcriptome shotgun sequencing analysis of further gene families and in further sMDI and cMDI tumor models will be the focus of subsequent investigations. This may also help to determine the tissue of origin and further characterize the various MDI tumor models.

2.6. sMDI: Efficacy Studies

JA-0009 was used in two independent efficacy studies. In the first study, JA-0009 tumors were treated with antibodies against the inhibitory checkpoint molecule (mPD-1) or against the chemotherapeutic gemcitabine (Figure 6A). After randomization at day seven, treatment was performed three times with gemcitabine (300 mg/kg) or with anti-mPD-1 antibodies (10 mg/kg). The study was terminated at day 22 due to a critical tumor burden in the vehicle group (tumor volumes in four animals were $>2000 \text{ mm}^3$). Gemcitabine treatment resulted in significant tumor growth inhibition ($p = 0.0012$) with nearly complete tumor regression in all mice on day 22; anti-mPD-1 treatment showed only a moderate effect that was statistically not significant ($p = 0.0654$).

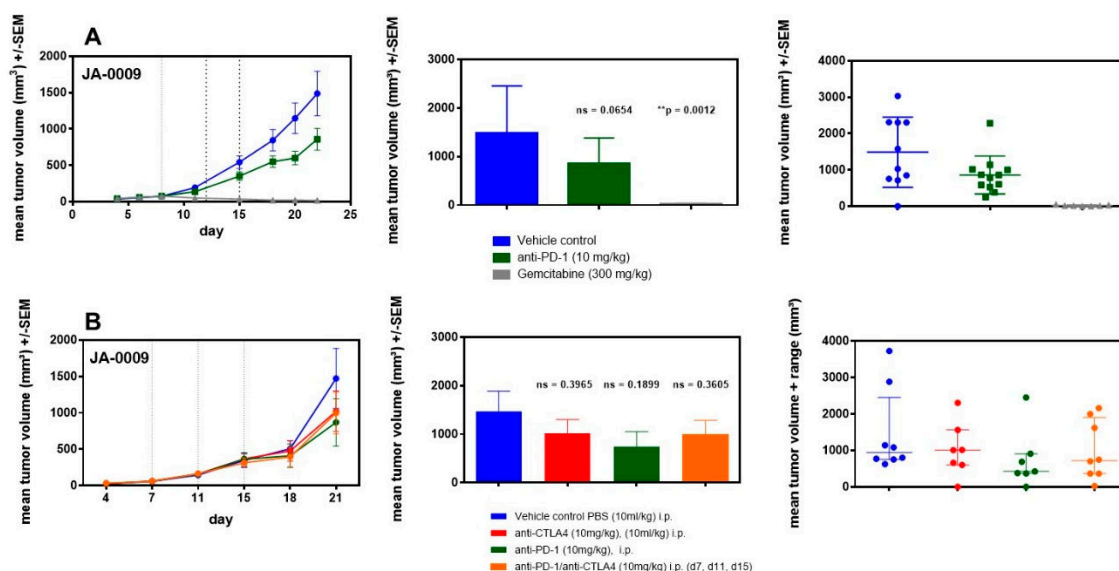


Figure 6. (A). Two independent efficacy studies with chemotherapeutic gemcitabine or antibodies against the inhibitory checkpoint molecules mPD-1 and mCTLA-4 in the sMDI JA-0009 tumor model. Efficacy study of the sMDI JA-0009 tumor model characterized the effects of antibodies against the immune checkpoint inhibitor mPD-1 as well as gemcitabine as a chemotherapeutic agent. (B). In the second study treatment, the effects of antibodies against the immune checkpoint inhibitor mPD-1, mCTLA-4, or both were tested. Mice were randomized on day 7. Dotted lines show the timepoints of treatment. Results are shown as growth curves (curve chart), mean of groups (bar graphs), and individual values of a single mouse per group at the study termination (dot plots). Probability (P) was tested with the parametric unpaired t -test (GraphPad Prism 5.04, GraphPad Software, San Diego, CA 92108, USA) compared to PBS vehicle control. Differences were determined as not significant with $ns > 0.050$ and significant with * $p < 0.050$, ** $p < 0.010$, or *** $p < 0.001$.

In the second study, we investigated whether anti-mCTLA-4 treatment showed similar inhibitory effects when compared to anti-mPD-1 treatment, as well as if the anti-mPD-1 effect could be amplified through a combination with anti-mCTLA-4 treatment (Figure 6B). Anti-mPD-1 treatment again resulted in moderate but not significant tumor growth inhibition ($p = 0.1899$). The trend observed in the first study was confirmed. Treatment with anti-mCTLA-4 antibodies resulted in marginal tumor growth inhibition ($p = 0.3965$). The combination of both antibodies did not result in additive effects and

showed similar weak effects on tumor growth ($p = 0.3605$) as those shown for the anti-mCTLA-4 antibody treatment alone.

3. Discussion

Mouse in vivo tumor models are important tools for studying the various causes and molecular mechanisms of tumor development as well as for investigating new therapeutic approaches [5,10,12,13,47,48]. Limitations of the current mouse models include the differences between the structure and function of the human and mouse immune system and physiology [42–46]. Therefore, these variances must be considered when designing and performing in vivo experiments with the goal of clinical translation [46]. The immunoglobulin-superfamily-based adaptive and innate immune system of humans, mice, and other vertebrates has co-evolved in common ancestors [42]. Therefore, the general structures of the immune system in humans and mice are phylogenetically sufficiently closely related, and also display many common, conserved cellular and molecular mechanisms that enable the use of syngeneic mouse tumors in immunocompetent mice as relevant experimental in vivo cancer models [38,42–44,46]. Further selection and studies on relevant syngeneic mouse tumor models are valuable for characterizing new tumor therapeutic and immunotherapeutic approaches [5,47,48].

Here, we established a novel type of spontaneously appearing syngeneic primary tumors from naïve and untreated animals with low passage number that were propagated as tissue pieces in mice only without any prior or subsequent in vitro manipulation, showing mostly conserved original tumor characteristics and intratumoral immune cell populations (Figures 2 and 3, Doc. S1-sMDI). The use of tumor tissue pieces to establish or amplify tumor growth is a valuable procedure in patient-derived xenografting (PDX) and has also been used as an intermediate step in transplanting syngeneic or semi-allogeneic mouse tumors [22–28,64–66]. In the syngeneic mouse situation, this procedure was commonly used as an auxiliary means to establish tumor cell lines from primary tumor pieces either by in vivo manipulation (e.g., intraperitoneal application) or in vitro artificial tissue culture of enzymatic or mechanical disrupted tumor tissues. Cell line-based mouse models have been preferred for a long time, e.g., with Ehrlich Ascites or L1210 cells, since they are good to handle [67,68]. The manipulated cells often show enhanced tumorigenicity when compared to the original tissues [66], and such tumor cell lines additionally allow for the possibility to be used for in vitro investigations of tumor properties, behavior, and therapeutic sensitivity [69].

To the best of our knowledge, we used this technique for the first time to create a novel and separate syngeneic in vivo model type. The primary spontaneous mouse-derived-isograft (sMDI) in vivo cancer models (Table 1) displayed new model quality and properties not available with standard syngeneic or xenograft tumor models. One main advantage of this model is that it is very close to the real clinical situation in patients, representing actual outgrowing spontaneous primary tumors or metastases that have overcome the body's own regulatory mechanisms. The models are transplantable; they are tumorigenic not only in the primary tumor-bearing animal, but also in other syngeneic fully immunocompetent hosts without any prior or subsequent additional in vivo or in vitro manipulation (Figure 1). We expected that, depending on the mouse strain, sex, or age, about 15–100% of the animals would develop spontaneous solid tumors of non-hematopoietic and hematopoietic origin of different organogenesis at the age of one to two years [70–74]. Only in the case of female C3H/HeJ was a preference of mammary carcinoma or hepatoma anticipated [70]. Finally, in this first study, we were able to establish nine different sMDI tumor models in five different inbred strains, with different sexes (7 female and 2 male) and in three different H-2 MHC class I haplotypes (Table 1, Figures 1 and 2), enhancing the number of available syngeneic tumor models. The apparent dominance of female sMDIs was not confirmed by further outgrowing tumor/suspicious tissue isolates in seven other mice with a female to male ratio of three to four.

In most cases, we could not differentiate whether tumor or suspicious tissues from primary isolates actually represented the primary tumor or the secondary metastatic tissues. Tumorous tissue derived from the lung of JA-0018 CBA/J (lymphoma) or the enlarged axillary lymph nodes and

splenomegaly found in JA-0009 DBA/2N mice (adenocarcinoma) are exemplary illustrations of this issue (Figures 2 and 3). In the case of sMDI JA-0021, the mouse strain of the tumor origin also remained unclear for a time, since it was outgrowing from secondary SCID/bg thymus tissue and only growing in immune-deficient mice. As the primary C3H/HeJ lymph node itself showed a questionable lymphoma or even non-malignant morphology (see Supplementary Materials, Doc.S1-sMDI), it is likely that we established by chance a primary SCID/bg lymphoma/thymoma (Figure 2), as already described in NOD-SCID mice [75]. However, whether the lymphoma also grows in H-2^d × H-2^b immunocompetent F1 hybrids has to be verified.

In summary, during these studies that lasted for more than two years, nine sMDI tumors were finally established, and suspicious tissues from seven other mice were isolated. Therefore, a total of 16 out of 36 (i.e., 16/26 alive, long-term monitored) animals developed primary transplantable spontaneous tumors within the more than two years of observation. This indicates that this method seems to be a valuable tool for the development of novel tumor models to enhance model variety.

The established tumors showing intense vascularization or invasive growth in some models displayed the histopathological properties of solid tumors (Doc. S1-sMDI – page 11 ff) [76] such as adenocarcinomas ($n = 4$), lymphomas ($n = 4$), or histiocytic sarcomas or histiocyte-associated lymphomas, HS/HAL ($n = 1$) (Figures 2 and 3, Doc. S1-sMDI). The tumors showed various host stromal or inflammatory reactions and varying numbers of tumor infiltrating leukocytes, which seem to be similar when comparing the primary and re-transplanted tumor pieces (Figures 2 and 3, and Doc. S1-sMDI). First, the flow cytometric analyses confirmed and refined the histopathological findings of tumor infiltrating leukocytes (Figure 5A,B). With regard to the host stroma reaction and inflammatory responses (Doc. S1-sMDI), sMDI tumor models also displayed the defined inflamed or noninflamed tumor immune infiltrate phenotypes [5,61,62]. Therefore, the sMDI models seem to reflect the classical clinical situation in patients as well as heterogeneous tumor types, individual immunological response pattern, and varying phenotypes of the tumor immune infiltrates.

As in patients [77], a histologically heterogeneous intratumoral composition of malignant cells appeared in some sMDIs, e.g., in cases JA-0017, or JA-0032 (Figure 3). The trabecular epithelial carcinoma cells found in one secondary JA-0017 tumor (0096-17, P2F) might have resulted from the actual differentiation of the primary complex mixed adenocarcinoma cells of an unidentified exocrine gland. Whether multiple re-transplantation itself (passage 2) or of frozen material triggers the differentiation remains to be verified since second re-transplantation (1234-16, P1) showed an identical complex mixed histology with primary ADC. The histologically indicated instability of the tumor, i.e., losing the balance of the complex mixed primary ADC, which results in the possible preference of one or another tumor cell population in the follow-up daughter tumors. Whether this imbalance in JA-0017 tumor heterogeneity is able to explain the heterogeneous growth remains to be verified (Figure 4). sMDI JA-0032, a primary papillary lung adenocarcinoma composed of tubule and papillary proliferations, and its secondary (0055-17, P1) tumor, in this case not derived from previously frozen material, also displayed histological heterogeneous phenotypes and heterogeneous tumor growth (Figure 4). Therefore, it must be further verified if growth and histological heterogeneity are general or particularly changing properties of some sMDIs. In addition, whether homogeneous follow-up daughter tumors originating from heterogeneous primary tumors could be established as possibly stable sMDI subtypes should be determined. Regarding the histological variability, whether the heterogeneity in some tumors coincides with the changing numbers and compositions of tumor infiltrating leukocytes should be examined (as indicated by histological findings, e.g., in JA-0017).

sMDI JA-0009 is an adenocarcinoma originating from the exocrine gland of either the mammary gland, pancreas, salivary, prostate, or bile duct. The histologically homogeneous and invasive tumor was characterized by the consistent and fast growth of subcutaneous re-transplants after about 22 days (Figure 4). To obtain insights into the mechanisms and interactions of tumor growth, immune system, and physiological background of the novel sMDI, a detailed analysis of the model was performed. This will be the basis to create or analyze new therapeutic (immunological) approaches.

Mosely et al. extensively characterized six commonly used syngeneic standard tumor models by array comparative genomic hybridization, whole-exome sequencing, exon microarray analysis, and flow cytometry [5] to enable investigators to select appropriate models to gauge the activity of feasible immunotherapeutic concepts as well as combinations with targeted therapies for the given *in vivo* situation. We used a similar approach (flow cytometric analyses, chemotherapeutic or immunotherapeutic, immune checkpoint inhibitor intervention, and preliminary gene expression analysis by RNA-Seq) to characterize sMDI model JA-0009. However, the gene expression pattern determined by complete RNA-Seq whole transcriptome shotgun sequencing were here analyzed merely for various genes of only three gene families related to tumor malignancy or anti-tumor immune response: tyrosine kinase receptors, immune population markers, and an IFN- γ signature. Since the definite tissue origin of the most outgrowing MDI tumor models could not be identified (Section 2.2) a more detailed characterization of the gene expression of the whole transcriptome shotgun sequencing analysis of further gene families and in further sMDI and cMDI tumor models will be the focus of subsequent investigations.

As expected from previous ADC xenograft models and clinical data [78–81], chemotherapeutic intervention with gemcitabine completely inhibited the growth of primary mouse malignant epithelial tissue of exocrine gland origin (Figure 6A,B). In the future, such complete regression could allow the establishment of therapy-resistant MDI sublines. We established such a subline from a primarily regressed and further relapsed PD-1-sensitive cell line-derived MC38-CEA tumor (Doc.S3 sMDI, Figure S3 sMDI), which not only changed the antigenic profile (loss of CEA expression), but also became completely PD-1-resistant (Doc.S3 sMDI, Figure S3 sMDI). In contrast to gemcitabine, JA-0009 was completely insensitive to immune checkpoint inhibitor intervention by PD-1 or CTLA-4 antibodies (Figure 6). Since several syngeneic standard models were also completely insensitive to immune checkpoint inhibitor intervention (Doc.S2, Figure S2) [82], we compared the JA-0009 flow cytometry data with the respective results from our syngeneic standard tumor models (colon carcinoma MC38-CEA, colon carcinoma CT26.WT, lung carcinoma LL-2, melanoma Clone M3, breast carcinoma 4T1, renal carcinoma RENCA, and melanoma B16.F10) to determine possible similarities. As expected, anti-immune checkpoint inhibitor treatment of sensitive syngeneic tumors (Doc. S2, Figure S2), such as CT26.WT or MC38-CEA, showed a completely different immune cell composition (Figure 5B). However, in the insensitive models (e.g., LL/2, 4T1 or RENCA), the composition of tumor infiltrating leukocytes was also completely different to sMDI JA-0009 (Figure 5B). Histologically, the JA-0009 tumor showed a different situation with few infiltrates of small lymphocytes and neutrophils, with more neutrophils than small lymphocytes in carcinomatous tissue (Doc.S1 sMDI–page 34 ff). Flow cytometric analyses confirmed the weak infiltration with CD8⁺ or CD4⁺ T cells, but showed a massive invasion of M2 macrophages into the JA-0009 tumor (>70% of tumor infiltrating leukocytes) (Figure 5B) [5,82]. Since M2 macrophages can act as anti-inflammatories due to the production of immunosuppressive factors such as IL-10, transforming growth factor β (TGF β), or prostaglandin E2 (PGE2), and the recruitment of immunosuppressive regulatory T cells [83], immune checkpoint inhibitor treatment only moderately affected the tumor growth of JA-0009. Therefore, a tumor promoting function by M2 macrophages can be assumed [84,85], which has been reported in some patients [86–88]. Therefore, further studies should try to influence the polarization and differentiation of M2 macrophages in the JA-0009 tumor using antibiotics, shifting gut dysbiosis, or by coumarins [84,89], to verify the actual role of M2 macrophages in this model. Enhanced expression of CD44, CD45, Ly6C1, Granzyme, CXCL10, and CCR5 as confirmed by the RNA-Seq analyses demonstrated the massive macrophage infiltration (Tables S1b,c, Figures S1 a_{i-iii}, and S1 b_{i-iii}). However, e.g., abnormal c-Met activation in the epithelial tumor cells (Table S1a, and Figures S1 a_{iii}, and b_{iii}) indicates that additional factors might be involved in the poor immunotherapeutic prognosis in sMDI JA-0009 [90].

As in the case of JA-0009, after more detailed histological, immunohistochemical, flow cytometric, genetic, and functional characterization, it will be applicable to determine the individual intratumoral invasion and immunological parameters. This would allow the characterization of therapeutic

interventions related to the respective tumor entities, tumor infiltrating leukocyte composition, gene expression, and general immunity stage in the spleen, lymph node, or blood, and enables the selection of suitable models to evaluate the activity of new therapeutic concepts. The four sMDI ADCs derived from three female and one male of four different mouse strains as well, as the four sMDI lymphomas derived from three females and one male of three mouse strains, already provide the possibility of comparing the various characteristics of one tumor type and to test their sensitivity in various mouse strains. The four sMDI ADCs will also allow a preliminary investigation to determine if eventual resemblances or pronounced disparities in the outcome of different therapeutic concepts might reflect strain-dependent, tumor-type (e.g., ADC) related, or individual tumor-specific properties.

However, the currently available sMDIs appear insufficient to answer further questions, e.g., whether tumors (1) of different histopathological classification (e.g., adenocarcinomas, sarcomas, or lymphomas), or (2) of similar histopathology (e.g., various adenocarcinomas) within one single mouse strain display similar or variant genetic, cell biological, or immunological characteristics. Additionally, (3) questions whether these tumors are therefore differentially sensitive or insensitive to certain therapeutic approaches, or (4) if such differences may depend on a distinct MHC class background, remain unanswered, since only one or two tumors per individual mouse strain are accessible, which are even mostly of different histopathological diagnosis.

To address some of these questions, we developed another type of MDI induced by carcinogens, the cMDI [59]. Using carcinogen induction, we established a larger number of individual tumors of a more histologically-related origin in a manageable number of animals and a shorter time frame.

Our newly established MDI models increase the pool of available syngeneic *in vivo* tumor models, not only in quantity (plus nine), but also in quality (primary, spontaneous, in five to six various mouse strains, few passages, neither *in vitro* nor *in vivo* manipulated), and provide the ability to characterize new experimental and translational *in vivo* cancer therapeutic concepts.

Future Outlook

The novel sMDI and cMDI models [59] are promising tools for characterizing new therapeutic approaches in the presence of a functional immune system. New possibilities for the syngeneic MDI tumor models have been provided. The inclusion of further inbred mouse strains will enhance the range of models with immunological differences [49–52], genetic heterogeneity in angiogenesis [91], various susceptibility to certain drugs [92], or strain-specific susceptibility for metastasis [93]. The inclusion of mouse strains with the not-yet-considered phylogenetic H-2 class I and the different class 2 antigenic background, of further carcinogens, or of physical tumor induction, e.g., by ultraviolet (UV)-light or radioactive irradiation, will additionally increase the model range. Finally, it is possible to include histologically stable sMDI subtypes established from homogeneous re-transplanted tumors or therapy-resistant sublines derived from relapsing tumors (Doc. S3, Figure S3) after various kinds of treatments (immunological, chemotherapeutic, irradiation or combinations thereof).

4. Materials and Methods

4.1. Mouse Strains

All *in vivo* experiments were performed in accordance with the German Animal License Regulations (Tierschutzgesetz) identical to the UKCCCR Guidelines for the Welfare of Animals in Experimental Neoplasia (licenses G-15/99, sMDI, Regierungspräsidium, Freiburg, Germany) [94]. Mice of different strains and sexes (Table 2) were purchased from Charles River Laboratories, Sulzfeld, Germany, at 6 to 14 weeks of age.

Table 2. Mouse strains and sex included in generation of sMDI.

Mouse Strain	CRL Nomenclature	Sex	H-2 Haplotype	Tumor Growth	
				<i>n</i>	(<i>n</i>)
Black 6	C57BL/6NCrI	♂ ♀	H-2 ^b	-	(1)
Black 6 albino	C57BL/6N-Tyrc-Brd / BrdCrCrI	♂	H-2 ^b	1	(1)
		♀		1	(1)
Balb/c	BALB/cAnNCrI	♂	H-2 ^d	1	(2)
		♀		-	(1)
CBA/J	CBA/J-Pde6brd1	♀	H-2 ^k	2	-
DBA/2	DBA/2NCrI	♀	H-2 ^d	2	-
C3H/HeJ	C3H/HeJ-Pde6brd1	♀	H-2 ^k	1	(1)
SCID beige	CB17.Cg-PrkdcscidLystbg/CrI	♀	H-2 ^d × H-2 ^b	1 *	-

Note: Four animals from each of the specified strains and sexes were included for long term observation. Ten mice were found dead for unknown reasons ($n = 6$) or had to be euthanized for ethical reasons ($n = 4$) other than tumor signs. SCID/bg mice were used as the recipient hosts only to avoid eventual tumor rejection in immunocompetent mice. Tumor growth is reported for n = number of animals with finally established sMDI tumors as well as for (n) = number of candidates, i.e., potential frozen sMDI samples. * The thymus of one SCID/bg recipient mouse was found to be malignant after re-transplantation. CRL—Charles River Laboratories (Sulzfeld, Germany).

They were kept under pathogen-free conditions in conventional cages stored in Scantainer Ventilated Cabinets (Scanbur, Denmark), holding four animals with autoclaved nesting material, and cardboard tunnels. If the animals exceeded 30 g body weight, they were separated and only 2–3 animals were housed in one cage. Mice were subjected to a 12/12 h light/dark cycle, with ad libitum autoclaved water and a M-Zucht rodent diet (ssniff Spezialdiäten GmbH, Soest, Germany).

4.2. sMDI: Establishment and Re-Transplantation

To establish spontaneous tumors from naïve and untreated animals, four mice of each strain, as shown in Table 2, were monitored long-term (≥ 2 years) for spontaneous tumor appearance or other critical signs indicating spontaneous tumor development (Figure 1). Animal weights were recorded twice weekly (Monday and Friday) during long-term observations and three times weekly (Monday, Wednesday, and Friday) after re-transplantation and during treatment studies. Animal behavior was monitored daily.

Termination criteria: Tumors exceeding 2000 mm³ or an edge length of 2 cm, tumor ulceration, weight $\geq 20\%$, cachectic phenotype (tumor cachexia), abnormal, non-physiological posture as a sign of pain, apathy (severe inactivity), strongly reduced feed and water intake, severe dyspnea, motor deficit manifestations or paralysis, ascites, persisting diarrhea, massive behavioral changes, or other unexpected signs indicating tumor burden.

Mice were sacrificed according to the ATBW/GV-SOLAS (Arbeitsgemeinschaft der Tierschutzbeauftragten in Baden-Württemberg/Gesellschaft für Versuchstierkunde, Society of Laboratory Animal Science), and all tissues were assessed macroscopically and cut in sterile phosphate-buffered solution (PBS) in petri dishes by scalpels into small pieces (2–3 mm³). The tumor pieces were implanted subcutaneously into the flank of 5- to 6-week-old sex-matched syngeneic and/or female immunodeficient SCID/bg mice using a trocar. Implantation was performed under anesthesia with 2–3 volume percent isoflurane in combination with an oxygen flow rate of 0.6 L/min. If possible, tumor pieces were also frozen and stored in 10% dimethyl sulfoxide (DMSO) freezing medium at -80 °C or colder. Outgrowing tumor volumes were determined by caliper measurements two times a week. Tumor sizes were calculated according to the formula $W^2 \times L/2$ (L = length and W = the perpendicular width of the tumor, $L > W$). During necropsy, tumor tissue and other suspicious tissues were collected. In the next step, non-necrotic tissue areas were cut into small pieces

(2–3 mm³), and amplified once again by re-transplantation into syngeneic, sex-matched, and/or female immunodeficient SCID/bg mice. Excess tumor/tissue pieces were frozen stored until further use. Amplification and sample collection were repeated several times, and samples were called F1–Fn ($n = \text{max. } 5\text{--}10$ amplifications) [95]. Certain tumor pieces (primary and re-transplanted) were directly fixed in formalin during necropsy for further analysis. The main part of model establishment was the re-transplantation and stable outgrowth of previously frozen and stored tumor pieces into syngeneic animals. To this end, the frozen tumor pieces were thawed at 37 °C and washed twice in ice-cold PBS, and then implanted by trocar as described above.

4.3. sMDI: Histological and Pathological Analysis

Wet tissues were collected in embedding cassettes and formalin-fixed in 4% neutral buffered formaldehyde (Engelbrecht, Edermünde, Germany) at room temperature for about 24 h, followed by automatic dehydration and embedding in IHC-grade paraffin using a Leica TP 1020 (Leica Biosystems, Nussloch, Germany) and Leica Histo Core Arcadia H/C (Leica Biosystems). FFPE tissue blocks were stored at room temperature. Sections of the paraffin blocks were cut into slices of approximately 2–3 µm thickness and stained with H&E at TPL Path Labs (Freiburg, Germany).

Histopathological examinations were then performed blind using a Zeiss Axioscope microscope (Carl Zeiss, Jena, Germany) at a magnification of up to 400×, by one of the authors (TL). Digital microphotographs were taken using a Nikon Digital Sight DS-Fi camera (Nikon Instruments Europe B.V., Amsterdam, Netherlands). Whole slide imaging using an Axioscan Z1 (Carl Zeiss) were also performed from all case, for the purpose of comprehensive iconography.

4.4. sMDI: Establishment and Efficacy Studies

To assess the growth and take rates of the re-transplanted and histopathologically characterized sMDIs, frozen tumor pieces were re-transplanted by trocar into 12 sex- and strain-matched animals. Primary tumor volumes were determined by caliper measurements. The health status was documented, and animals were euthanized individually before study termination when the above-mentioned ethical termination criteria were reached. The take rate is defined as a percentage of total tumor-bearing/developing versus all re-transplanted animals during the observation period. Tumor growth appearing only outside the observation period was not included in the analysis.

Frozen tumor pieces of the sMDIs were thawed at 37 °C and washed twice in ice-cold PBS, and then implanted by trocar into an appropriate number of sex- and strain- matched animals for efficacy studies. Implantation and health monitoring were performed as previously described in Section 4.2. In the following, the primary tumor volumes were determined by caliper measurements. After the primary tumors reached the sMDI respective mean volume (defining randomization criteria), tumor-bearing animals were randomized into three or four groups of 10 to 12 animals. For randomization, a robust automated random number generation within individual blocks was used (Excel 2016, Microsoft, Redmond, WA 98052, USA). Treatment was initiated on the same day or the day after, according to the following schedules: vehicle control (PBS or isotype control antibodies) or antibodies anti-mPD-1, anti-mCTLA-4, or a combination thereof [96] were injected intraperitoneally three times every third or fourth working day with a dosage of 10 mg/kg and an injection volume of 10 mL/kg or 5 mL/kg. Anti-mPD-1 antibody clone RMP1-14, rat IgG2a, and anti-mCTLA-4 antibody clone 9D9, mouse IgG2a were used. All antibodies for treatment were purchased by BioXCell, Lebanon, NH 03784. Chemotherapeutic drug gemcitabine (Pharmacy, University Medical Center Freiburg, Germany) was injected intravenously every fourth day with a dosage of 300 mg/kg and injection volume of 5 mL/kg [78,79]. Tumor growth and effects regarding tumor growth reduction due to therapeutic intervention were followed by caliper measurements until the end of observation. The study was finalized by necropsy, and the tumor volumes and wet weights were determined. In some cases, parts of tumors from various experimental groups were also formalin-fixed and paraffin embedded and used for flow cytometry analysis and/or for RNA-sequencing. Probability (P) was

tested with the parametric unpaired *t*-test (GraphPad Prism 5.04) when compared to the PBS vehicle control. Differences were determined as not significant with $ns > 0.050$ and as significant when $p < 0.050$, $p < 0.010$, and $p < 0.001$.

4.5. Flow Cytometric Analysis of sMDI Infiltrating-Immune Cells

At least 300 mg of tumor material was disrupted using gentleMACS™ C Tubes (Miltenyi Biotec, Bergisch Gladbach, Germany) containing the enzyme mix of the Tumor Dissociation Kit (mouse), according to the manufacturer's instructions. Erythrocytes were removed with the Red Blood Cell Lysis Solution (Miltenyi Biotec). Single cell suspensions were counted and dispensed in 96-well plates if possible at 3×10^6 cells/well (if there were less than 2×10^6 single cells in total in a tumor sample, the T cell panel was preferred for staining). The single cells were washed with PBS (Capricorn, Ebsdorfergrund, Germany) and stained for live cells with eBioscience™ Fixable Viability Dye (Thermo Fisher, Nidderau, Germany). After washing and centrifugation (400 *g*) the samples were incubated with 50 µL/well Fc block (anti-mouse CD16/CD32, 1:50) for 30 min in FACS™ buffer. Thereafter, a 2× concentrated master antibody mix (T cell panel with antibodies against murine CD45, CD3, CD4, CD8a, CD25, CD44, myeloid cell panel with antibodies against murine CD45, CD11b, CD11c, Ly6G, and Ly6C, and MΦ panel CD45, CD11b, F4/80, MHC II, CD206) was added to each well (50 µL) and incubated for 30 min in the dark. After washing, cells stained with the myeloid or macrophage antibody panel were fixed with 2% paraformaldehyde in PBS. Cells stained with the T cell antibody panel were prepared for intracellular staining. Intracellular staining was primed by adding 50 µL fix/perm buffer for 30 min. Thereafter, 1× permeabilization buffer (1:10 diluted with water; 100 µL) (Thermo Fisher Scientific) was added and cells were centrifuged at 836× *g*. The cell pellet was resuspended in 1× permeabilization buffer containing the anti-FoxP3 antibody and incubated for 30 min in the dark. After washing twice with 1× permeabilization buffer, cells were washed with the FACS™ buffer. The samples were analyzed by flow cytometry using a BD LSR Fortessa™ (Becton Dickinson, Heidelberg, Germany). All antibodies were purchased from Thermo Fisher with the exception of CD3 and CD206 (BioLegend, San Diego, CA 92121, USA) and CD8a (Becton Dickinson).

4.6. sMDI: RNA-Seq

Total RNA integrity and quantity was analyzed (StarSeq, Mainz, Germany) using the RNA Nano chip assay on an Agilent Bioanalyzer 2100 (Santa Clara, CA 95051, USA) and the Qubit RNA HS assay (Thermo Fisher Scientific). Poly-A+ isolation from total RNA, fragmentation of mRNA, and synthesis of double stranded cDNA was performed according to the NEB Next Ultra II Directional RNA Library Prep Kit for the Illumina protocol (New England Biolabs, Ipswich, UK). End-repaired, A-tailed, and double indexed adaptor-ligated cDNA was polymerase chain reaction (PCR)-amplified by 14 cycles. The libraries with an average size of 450 bp were sequenced in paired-end mode (2×151 bp) on an Illumina NextSeq 500 System (50 million paired-end reads of each library). Fragments per kilobase million (FPKM), from the double determination of two independent tumor samples each, were determined and depicted for a number of genes. The values from a single RNA-Seq experiment, i.e., from a single MDI model, thus reflected the objective gene expression pattern within the individual MDI tumor model.

However, FPKM values are not directly comparable across separate RNA-Seq experiments, i.e., across the different independently analyzed MDI tumor models [97]. However, if the majority of analyzed genes in various MDI samples display very similar, either low or high, FPKM patterns (Tables S1a–c, Figures S1 a_{i–iii}, and b_{i–iii}), an indirect, careful quantitative comparison of the expression patterns among these tumors is acceptable. Internal Relative Expression (IRE) of RNA-Seq determined FPKM-Values was calculated as quotient comparing individual gene expression within individual MDI models each, related to the expression of an internal, low FPKM-value reference gene (red triangle-Figure S1 b_{i–iii}). Data are shown as n-fold of expression of respective reference gene. For each

gene family one common reference gene, *Ctla4* (IFN γ signature), *Cd8b1* (immune population marker), and *Flt4* (tyrosine kinase receptor) was selected within the MDI models.

In contrast, a quantitative comparison with publicly available FPKM or RPKM values for different adult tissues of normal mice, for example from the METD database [63], was not performed since a definite characterization of primary tumor origin was not possible in most cases with the present histopathological analysis (Section 2.2).

5. Conclusions

The sMDI and carcinogen-induced MDI (cMDI) [59] models are promising new *in vivo* tools representing primary tumors with conserved tumor characteristics and intratumoral immune cell populations that were histologically and genetically characterized. Spontaneous tumor models do not represent any malignant degeneration, but instead represent outgrowing tumors (or metastases) that have overcome the body's own regulatory mechanisms, thus corresponding to clinically manifested tumors without any manipulation.

Inclusion of both sexes and various mouse strains with different MHC haplotypes and immunological background increase the therapeutic possibilities. The established sMDI and cMDI models can be further refined. Use of relapsing tumors from original tumors after various kinds of treatments (immunological, chemotherapeutic, irradiation, or combinations thereof) or strains with specific immunologic deficits, such as knockouts and transgenics, could provide further possibilities for finding treatments for such therapy-resistant re-growing tumors. Our models provide a broad experimental range for *in vivo* cancer therapeutic concepts.

Supplementary Materials: The following are available online at <http://www.mdpi.com/2072-6694/11/2/244/s1>, manuscript-supplementary.pdf: Table S1a sMDI_RNA-Seq: Expression of tyrosine kinase receptor (TKR) genes in selected sMDI JA-0009, and cMDI JA-201, and JA-2042, Table S1b sMDI_RNA-Seq: Expression of immune population marker genes (T-, B-, NK-cells, M Φ , and myeloid cells) in selected sMDI JA-0009, and cMDI JA-2011 and JA-2042, Table S1c sMDI_RNA-Seq: Expression of IFN- γ signature genes in selected sMDI JA-0009, and cMDI JA-2011 and JA-2042, Figure S1–sMDI_RNA-Seq: Figure S1a_{i-iii}–sMDI_RNA-Seq: FPKM-Values, Figure S1b_{i-iii}–sMDI_RNA-Seq: Internal Relative Expression, Doc. S1–sMDI: sMDI Histological and pathological analysis. This document summarizes the detailed histopathological analysis of primary and derived tumors of various sMDI models inclusive of respective large microphotographs, Doc. S2–sMDI: Material, Methods & Results: Efficacy studies with anti-mPD-1 and anti-mCTLA-4 in seven syngeneic standard mouse tumor models, Figure S2–sMDI: Efficacy studies with anti-mPD-1 and anti-mCTLA-4 in seven syngeneic standard mouse tumor models, Doc. S3–sMDI: Methods & Results: Establishment, efficacy study, and flow cytometric characterization of mPD-1-resistant MC38-CEA relapsed subline. Figure S3–sMDI: Establishment, efficacy study, and flow cytometric characterization of the mPD-1-resistant MC38-CEA relapsed subline.

Author Contributions: P.J. conceived the MDI studies (spontaneous and carcinogen-induced); P.J. and C.O. designed the animal experimental application; P.J., C.S., and H.W. designed the experimental setup; P.J., J.B., and H.W. performed the animal experiments; C.O. performed the veterinary monitoring; TL completed the histological and pathological analyses; H.W. performed the in-house RNA-Seq analysis; J.B. and H.W. performed flow cytometry analysis; J.B. and P.J. completed the establishment and efficacy studies; P.J., J.B., H.W., and C.S. wrote the manuscript, with input from all authors. All authors read and approved the final manuscript.

Funding: The research did not receive external funding. These R&D studies were fully financed by ProQinase GmbH (Freiburg, Germany).

Acknowledgments: Our thanks go to our colleagues Bianca Giesen, Ulrike Leisegang, Sandra Moor, Susanne Ruf, and Gojko Bijelic for their excellent technical support during our work. Special thanks to Katrin Schlie for critical reading and final editing of the manuscript.

Conflicts of Interest: ProQinase GmbH is the owner and provider of the established MDI models and will use them for their own commercial applications in tumor therapy and for testing new substances or strategies concomitant with cancer treatment. An MTA-restricted availability of the models for academic investigations and purposes will be possible. All authors declare that they have no competing individual interests.

Abbreviations

ADC	adenocarcinoma
AP	<i>appearance</i>
bg	beige mutation
cMDI	carcinogen-induced mouse-derived isografts
CRL	Charles River Laboratories
DMSO	Dimethyl sulfoxide
FACS	fluorescence activated cell sorter
FPKM	fragments per kilobase million
HS/HAL	histiocytic sarcoma/ /histiocyte-associated lymphoma
ICPI	immune checkpoint inhibitors
IFN	interferon
IHC	immunohistochemistry
IRE	internal relative expression
LN	lymph node
MCA	3-methylcholanthrene
mCTLA-4	mouse cytotoxic T-lymphocyte-associated protein 4
MDI	Mouse-derived isografts
cMDI	carcinogen-induced mouse-derived isograft
sMDI	spontaneous mouse-derived isograft
MDSC	myeloid-derived suppressor cells
MΦ	macrophage
MHC	major histocompatibility complex
M-MDSC	monocytic MDSC
MMR	macrophage mannose receptor
MNU	N-methyl-N-nitrosourea
mPD-1	mouse programmed cell death protein 1
NOD	non-obese diabetic
NOD mice	non-obese diabetic mice
NOS	not otherwise specified
NSG mice	NOD SCID gamma mice
PBS	phosphate-buffered saline
PDX	patient-derived xenografts
RNA	ribonucleic acid
RNA-Seq	RNA whole transcriptome shotgun sequencing
RPKM	reads per kilobase million
RRT	<i>real running time</i>
SCID	severe combined immunodeficiency disease
SCID mice	severe combined immunodeficiency mice
SCID/bg	SCID beige mutation
SCID/bg mice	severe combined immunodeficiency beige mice
TATA	tumor-associated transplantation antigens
Treg	regulatory T-cells
TTW	<i>treatment time window</i>
UKCCCR	United Kingdom Coordinating Committee of Cancer Research

References

1. Brahmer, J.R.; Tykodi, S.S.; Chow, L.Q.; Hwu, W.J.; Topalian, S.L.; Hwu, P.; Drake, C.G.; Camacho, L.H.; Kauh, J.; Odunsi, K.; et al. Safety and activity of anti-pd-l1 antibody in patients with advanced cancer. *N. Engl. J. Med.* **2012**, *366*, 2455–2465. [[CrossRef](#)]
2. Ribas, A. Tumor immunotherapy directed at pd-1. *N. Engl. J. Med.* **2012**, *366*, 2517–2519. [[CrossRef](#)] [[PubMed](#)]

3. Topalian, S.L.; Hodi, F.S.; Brahmer, J.R.; Gettinger, S.N.; Smith, D.C.; McDermott, D.F.; Powderly, J.D.; Carvajal, R.D.; Sosman, J.A.; Atkins, M.B.; et al. Safety, activity, and immune correlates of anti-pd-1 antibody in cancer. *N. Engl. J. Med.* **2012**, *366*, 2443–2454. [[CrossRef](#)] [[PubMed](#)]
4. Leach, D.R.; Krummel, M.F.; Allison, J.P. Enhancement of antitumor immunity by ctla-4 blockade. *Science* **1996**, *271*, 1734–1736. [[CrossRef](#)] [[PubMed](#)]
5. Mosely, S.I.; Prime, J.E.; Sainson, R.C.; Koopmann, J.O.; Wang, D.Y.; Greenawalt, D.M.; Ahdesmaki, M.J.; Leyland, R.; Mullins, S.; Pacelli, L.; et al. Rational selection of syngeneic preclinical tumor models for immunotherapeutic drug discovery. *Cancer Immunol. Res.* **2017**, *5*, 29–41. [[CrossRef](#)]
6. Prehn, R.T.; Main, J.M. Number of mouse histocompatibility genes involved in skin grafting from strain balb/can to strain dba/2. *J. Natl. Cancer Inst.* **1958**, *20*, 207–209. [[PubMed](#)]
7. Snell, G.D. Antigenic differences between the sperm of different inbred strains of mice. *Science* **1944**, *100*, 272–273. [[CrossRef](#)] [[PubMed](#)]
8. Strong, L.C. The establishment of the c(3)h inbred strain of mice for the study of spontaneous carcinoma of the mammary gland. *Genetics* **1935**, *20*, 586–591. [[CrossRef](#)] [[PubMed](#)]
9. Ngiow, S.F.; Loi, S.; Thomas, D.; Smyth, M.J. Mouse models of tumor immunotherapy. *Adv. Immunol.* **2016**, *130*, 1–24. [[PubMed](#)]
10. Teicher, B.A. Tumor models for efficacy determination. *Mol. Cancer Ther.* **2006**, *5*, 2435–2443. [[CrossRef](#)]
11. Hanahan, D.; Wagner, E.F.; Palmiter, R.D. The origins of oncomice: A history of the first transgenic mice genetically engineered to develop cancer. *Genes Dev.* **2007**, *21*, 2258–2270. [[CrossRef](#)] [[PubMed](#)]
12. Prehn, R.T.; Main, J.M. Immunity to methylcholanthrene-induced sarcomas. *J. Natl. Cancer Inst.* **1957**, *18*, 769–778. [[PubMed](#)]
13. Li, A.; Walling, J.; Kotliarov, Y.; Center, A.; Steed, M.E.; Ahn, S.J.; Rosenblum, M.; Mikkelsen, T.; Zenklusen, J.C.; Fine, H.A. Genomic changes and gene expression profiles reveal that established glioma cell lines are poorly representative of primary human gliomas. *Mol. Cancer Res.* **2008**, *6*, 21–30. [[CrossRef](#)] [[PubMed](#)]
14. Paul, S.M.; Mytelka, D.S.; Dunwiddie, C.T.; Persinger, C.C.; Munos, B.H.; Lindborg, S.R.; Schacht, A.L. How to improve r&d productivity: The pharmaceutical industry’s grand challenge. *Nat. Rev. Drug Discov.* **2010**, *9*, 203–214. [[PubMed](#)]
15. Bosma, M.J.; Carroll, A.M. The scid mouse mutant: Definition, characterization, and potential uses. *Annu. Rev. Immunol.* **1991**, *9*, 323–350. [[CrossRef](#)] [[PubMed](#)]
16. Flanagan, S.P. ‘Nude’, a new hairless gene with pleiotropic effects in the mouse. *Genet. Res.* **1966**, *8*, 295–309. [[CrossRef](#)] [[PubMed](#)]
17. Rygaard, J.; Povlsen, C.O. Heterotransplantation of a human malignant tumour to “nude” mice. *Acta Pathol. Microbiol. Scand.* **1969**, *77*, 758–760. [[CrossRef](#)] [[PubMed](#)]
18. Zamecnik, P.C.; Long, J.C. Growth of cultured cells from patients with hodgkin’s disease and transplantation into nude mice. *Proc. Natl. Acad. Sci. USA* **1977**, *74*, 754–758. [[CrossRef](#)]
19. Voskoglou-Nomikos, T.; Pater, J.L.; Seymour, L. Clinical predictive value of the in vitro cell line, human xenograft, and mouse allograft preclinical cancer models. *Clin. Cancer Res.* **2003**, *9*, 4227–4239.
20. Daniel, V.C.; Marchionni, L.; Hierman, J.S.; Rhodes, J.T.; Devereux, W.L.; Rudin, C.M.; Yung, R.; Parmigiani, G.; Dorsch, M.; Peacock, C.D.; et al. A primary xenograft model of small-cell lung cancer reveals irreversible changes in gene expression imposed by culture in vitro. *Cancer Res.* **2009**, *69*, 3364–3373. [[CrossRef](#)]
21. Williams, S.A.; Anderson, W.C.; Santaguida, M.T.; Dylla, S.J. Patient-derived xenografts, the cancer stem cell paradigm, and cancer pathobiology in the 21st century. *Lab. Investig.* **2013**, *93*, 970–982. [[CrossRef](#)] [[PubMed](#)]
22. Tentler, J.J.; Tan, A.C.; Weekes, C.D.; Jimeno, A.; Leong, S.; Pitts, T.M.; Arcaroli, J.J.; Messersmith, W.A.; Eckhardt, S.G. Patient-derived tumour xenografts as models for oncology drug development. *Nat. Rev. Clin. Oncol.* **2012**, *9*, 338–350. [[CrossRef](#)] [[PubMed](#)]
23. Bradford, J.R.; Wappett, M.; Beran, G.; Logie, A.; Delpuech, O.; Brown, H.; Boros, J.; Camp, N.J.; McEwen, R.; Mazzola, A.M.; et al. Whole transcriptome profiling of patient-derived xenograft models as a tool to identify both tumor and stromal specific biomarkers. *Oncotarget* **2016**, *7*, 20773–20787. [[CrossRef](#)] [[PubMed](#)]

24. Delitto, D.; Pham, K.; Vlada, A.C.; Sarosi, G.A.; Thomas, R.M.; Behrns, K.E.; Liu, C.; Hughes, S.J.; Wallet, S.M.; Trevino, J.G. Patient-derived xenograft models for pancreatic adenocarcinoma demonstrate retention of tumor morphology through incorporation of murine stromal elements. *Am. J. Pathol.* **2015**, *185*, 1297–1303. [[CrossRef](#)] [[PubMed](#)]
25. Julien, S.; Merino-Trigo, A.; Lacroix, L.; Pocard, M.; Goere, D.; Mariani, P.; Landron, S.; Bigot, L.; Nemati, F.; Dartigues, P.; et al. Characterization of a large panel of patient-derived tumor xenografts representing the clinical heterogeneity of human colorectal cancer. *Clin. Cancer Res.* **2012**, *18*, 5314–5328. [[CrossRef](#)] [[PubMed](#)]
26. Schneeberger, V.E.; Allaj, V.; Gardner, E.E.; Poirier, J.T.; Rudin, C.M. Quantitation of murine stroma and selective purification of the human tumor component of patient-derived xenografts for genomic analysis. *PLoS ONE* **2016**, *11*, e0160587. [[CrossRef](#)] [[PubMed](#)]
27. Coleman, C.N.; Higgins, G.S.; Brown, J.M.; Baumann, M.; Kirsch, D.G.; Willers, H.; Prasanna, P.G.; Dewhurst, M.W.; Bernhard, E.J.; Ahmed, M.M. Improving the predictive value of preclinical studies in support of radiotherapy clinical trials. *Clin. Cancer Res.* **2016**, *22*, 3138–3147. [[CrossRef](#)] [[PubMed](#)]
28. Unger, C.; Kramer, N.; Walzl, A.; Scherzer, M.; Hengstschlager, M.; Dolznig, H. Modeling human carcinomas: Physiologically relevant 3d models to improve anti-cancer drug development. *Adv. Drug Deliv. Rev.* **2014**, *79–80*, 50–67. [[CrossRef](#)] [[PubMed](#)]
29. Malaney, P.; Nicosia, S.V.; Dave, V. One mouse, one patient paradigm: New avatars of personalized cancer therapy. *Cancer Lett.* **2014**, *344*, 1–12. [[CrossRef](#)]
30. Pimiento, J.M.; Larkin, E.M.; Smalley, K.S.; Wiersma, G.L.; Monks, N.R.; Fedorenko, I.V.; Peterson, C.A.; Nickoloff, B.J. Melanoma genotypes and phenotypes get personal. *Lab. Invest.* **2013**, *93*, 858–867. [[CrossRef](#)]
31. Rey, F.; Guyader, C.; Decraene, C.; Lucchesi, C.; Auger, N.; Assayag, F.; De Plater, L.; Gentien, D.; Poupon, M.F.; Cottu, P.; et al. Molecular profiling of patient-derived breast cancer xenografts. *Breast Cancer Res.* **2012**, *14*, R11. [[CrossRef](#)] [[PubMed](#)]
32. Aparicio, S.; Hidalgo, M.; Kung, A.L. Examining the utility of patient-derived xenograft mouse models. *Nat. Rev. Cancer* **2015**, *15*, 311–316. [[CrossRef](#)] [[PubMed](#)]
33. Racki, W.J.; Covassin, L.; Brehm, M.; Pino, S.; Ignatz, R.; Dunn, R.; Laning, J.; Graves, S.K.; Rossini, A.A.; Shultz, L.D.; et al. Nod-scid il2rgamma(null) mouse model of human skin transplantation and allograft rejection. *Transplantation* **2010**, *89*, 527–536. [[CrossRef](#)] [[PubMed](#)]
34. Siolas, D.; Hannon, G.J. Patient-derived tumor xenografts: Transforming clinical samples into mouse models. *Cancer Res.* **2013**, *73*, 5315–5319. [[CrossRef](#)] [[PubMed](#)]
35. Shultz, L.D.; Ishikawa, F.; Greiner, D.L. Humanized mice in translational biomedical research. *Nat. Rev. Immunol.* **2007**, *7*, 118–130. [[CrossRef](#)] [[PubMed](#)]
36. Herndler-Brandstetter, D.; Shan, L.; Yao, Y.; Stecher, C.; Plajer, V.; Lietzenmayer, M.; Strowig, T.; de Zoete, M.R.; Palm, N.W.; Chen, J.; et al. Humanized mouse model supports development, function, and tissue residency of human natural killer cells. *Proc. Natl. Acad. Sci. USA* **2017**, *114*, E9626–E9634. [[CrossRef](#)] [[PubMed](#)]
37. Huang, D.; Song, S.J.; Wu, Z.Z.; Wu, W.; Cui, X.Y.; Chen, J.N.; Zeng, M.S.; Su, S.C. Epstein-barr virus-induced vegf and gm-csf drive nasopharyngeal carcinoma metastasis via recruitment and activation of macrophages. *Cancer Res.* **2017**, *77*, 3591–3604. [[CrossRef](#)] [[PubMed](#)]
38. Wang, M.; Yao, L.C.; Cheng, M.; Cai, D.; Martinek, J.; Pan, C.X.; Shi, W.; Ma, A.H.; De Vere White, R.W.; Airhart, S.; et al. Humanized mice in studying efficacy and mechanisms of pd-1-targeted cancer immunotherapy. *FASEB J.* **2018**, *32*, 1537–1549. [[CrossRef](#)]
39. Fu, J.; Sen, R.; Masica, D.L.; Karchin, R.; Pardoll, D.; Walter, V.; Hayes, D.N.; Chung, C.H.; Kim, Y.J. Autologous reconstitution of human cancer and immune system in vivo. *Oncotarget* **2017**, *8*, 2053–2068. [[CrossRef](#)] [[PubMed](#)]
40. Tormo, A.; Khodayarian, F.; Cui, Y.; Al-Chami, E.; Kanjarawi, R.; Noe, B.; Wang, H.; Rafei, M. Interleukin-21 promotes thymopoiesis recovery following hematopoietic stem cell transplantation. *J. Hematol. Oncol.* **2017**, *10*, 120. [[CrossRef](#)] [[PubMed](#)]
41. Sundarasetty, B.; Volk, V.; Theobald, S.J.; Rittinghausen, S.; Schaudien, D.; Neuhaus, V.; Figueiredo, C.; Schneider, A.; Gerasch, L.; Mucci, A.; et al. Human effector memory t helper cells engage with mouse macrophages and cause graft-versus-host-like pathology in skin of humanized mice used in a nonclinical immunization study. *Am. J. Pathol.* **2017**, *187*, 1380–1398. [[CrossRef](#)] [[PubMed](#)]

42. Bailey, M.; Christoforidou, Z.; Lewis, M.C. The evolutionary basis for differences between the immune systems of man, mouse, pig and ruminants. *Vet. Immunol. Immunopathol.* **2013**, *152*, 13–19. [[CrossRef](#)] [[PubMed](#)]
43. Mestas, J.; Hughes, C.C. Of mice and not men: Differences between mouse and human immunology. *J. Immunol.* **2004**, *172*, 2731–2738. [[CrossRef](#)] [[PubMed](#)]
44. Shay, T.; Jojic, V.; Zuk, O.; Rothamel, K.; Puyraimond-Zemmour, D.; Feng, T.; Wakamatsu, E.; Benoist, C.; Koller, D.; Regev, A.; et al. Conservation and divergence in the transcriptional programs of the human and mouse immune systems. *Proc. Natl. Acad. Sci. USA* **2013**, *110*, 2946–2951. [[CrossRef](#)] [[PubMed](#)]
45. Zschaler, J.; Schlorke, D.; Arnhold, J. Differences in innate immune response between man and mouse. *Crit. Rev. Immunol.* **2014**, *34*, 433–454. [[CrossRef](#)] [[PubMed](#)]
46. Haley, P.J. Species differences in the structure and function of the immune system. *Toxicology* **2003**, *188*, 49–71. [[CrossRef](#)]
47. Dranoff, G. Experimental mouse tumour models: What can be learnt about human cancer immunology? *Nat. Rev. Immunol.* **2012**, *12*, 61–66. [[CrossRef](#)] [[PubMed](#)]
48. Gould, S.E.; Junttila, M.R.; de Sauvage, F.J. Translational value of mouse models in oncology drug development. *Nat. Med.* **2015**, *21*, 431–439. [[CrossRef](#)]
49. Belzung, C.; Barreau, S. Differences in drug-induced place conditioning between balb/c and c57bl/6 mice. *Pharmacol. Biochem. Behav.* **2000**, *65*, 419–423. [[CrossRef](#)]
50. Chen, X.; Oppenheim, J.J.; Howard, O.M. Balb/c mice have more cd4+cd25+ t regulatory cells and show greater susceptibility to suppression of their cd4+cd25- responder t cells than c57bl/6 mice. *J. Leukoc. Biol.* **2005**, *78*, 114–121. [[CrossRef](#)]
51. Melgar, S.; Karlsson, A.; Michaelsson, E. Acute colitis induced by dextran sulfate sodium progresses to chronicity in c57bl/6 but not in balb/c mice: Correlation between symptoms and inflammation. *Am. J. Physiol. Gastrointest. Liver Physiol.* **2005**, *288*, G1328–G1338. [[CrossRef](#)] [[PubMed](#)]
52. Tucker, C.F.; Nebane-Ambe, D.L.; Chhabra, A.; Parnell, S.A.; Zhao, Y.; Alard, P.; Kosiewicz, M.M. Decreased frequencies of cd4+cd25+foxp3+ cells and the potent cd103+ subset in peripheral lymph nodes correlate with autoimmune disease predisposition in some strains of mice. *Autoimmunity* **2011**, *44*, 453–464. [[CrossRef](#)] [[PubMed](#)]
53. Petkov, P.M.; Ding, Y.; Cassell, M.A.; Zhang, W.; Wagner, G.; Sargent, E.E.; Asquith, S.; Crew, V.; Johnson, K.A.; Robinson, P.; et al. An efficient snp system for mouse genome scanning and elucidating strain relationships. *Genome Res.* **2004**, *14*, 1806–1811. [[CrossRef](#)]
54. Watanabe, H.; Numata, K.; Ito, T.; Takagi, K.; Matsukawa, A. Innate immune response in th1- and th2-dominant mouse strains. *Shock* **2004**, *22*, 460–466. [[CrossRef](#)]
55. Kuroda, E.; Sugiura, T.; Zeki, K.; Yoshida, Y.; Yamashita, U. Sensitivity difference to the suppressive effect of prostaglandin e2 among mouse strains: A possible mechanism to polarize th2 type response in balb/c mice. *J. Immunol.* **2000**, *164*, 2386–2395. [[CrossRef](#)] [[PubMed](#)]
56. Wang, H.; Hosiawa, K.A.; Min, W.; Yang, J.; Zhang, X.; Garcia, B.; Ichim, T.E.; Zhou, D.; Lian, D.; Kelvin, D.J.; et al. Cytokines regulate the pattern of rejection and susceptibility to cyclosporine therapy in different mouse recipient strains after cardiac allografting. *J. Immunol.* **2003**, *171*, 3823–3836. [[CrossRef](#)] [[PubMed](#)]
57. Sellers, R.S.; Clifford, C.B.; Treuting, P.M.; Brayton, C. Immunological variation between inbred laboratory mouse strains: Points to consider in phenotyping genetically immunomodified mice. *Vet. Pathol.* **2012**, *49*, 32–43. [[CrossRef](#)] [[PubMed](#)]
58. Jovicic, N.; Jeftic, I.; Jovanovic, I.; Radosavljevic, G.; Arsenijevic, N.; Lukic, M.L.; Pejnovic, N. Differential immunometabolic phenotype in th1 and th2 dominant mouse strains in response to high-fat feeding. *PLoS ONE* **2015**, *10*, e0134089. [[CrossRef](#)] [[PubMed](#)]
59. Beshay, J.; Jantscheff, P.; Lemarchand, T.; Obodozie, C.; Schächtele, C.; Weber, H. New mouse-derived isograft (mdi) tumor models ii. Carcinogen-induced cmdi models for immune as well as other therapeutic approaches. *Cancers* **2018**, in press.
60. Hao, X.; Fredrickson, T.N.; Chattopadhyay, S.K.; Han, W.; Qi, C.F.; Wang, Z.; Ward, J.M.; Hartley, J.W.; Morse, H.C., 3rd. The histopathologic and molecular basis for the diagnosis of histiocytic sarcoma and histiocyte-associated lymphoma of mice. *Vet. Pathol.* **2010**, *47*, 434–445. [[CrossRef](#)]
61. Gajewski, T.F.; Schreiber, H.; Fu, Y.X. Innate and adaptive immune cells in the tumor microenvironment. *Nat. Immunol.* **2013**, *14*, 1014–1022. [[CrossRef](#)] [[PubMed](#)]

62. Sharma, P.; Allison, J.P. The future of immune checkpoint therapy. *Science* **2015**, *348*, 56–61. [[CrossRef](#)] [[PubMed](#)]
63. METD Database: Whereby XX Was Taken for the Respective Gene Name. Available online: <https://www.ncbi.nlm.nih.gov/gene/?term=XX+mus+musculus> (accessed on 16 February 2019).
64. Juacaba, S.F.; Horak, E.; Price, J.E.; Tarin, D. Tumor cell dissemination patterns and metastasis of murine mammary carcinoma. *Cancer Res.* **1989**, *49*, 570–575. [[PubMed](#)]
65. McFarland, V.W.; Mora, P.T.; Schultz, A.; Pancake, S. Cell properties after repeated transplantation of spontaneously and of sv40 virus transformed mouse cell lines. I. Growth in culture. *J. Cell Physiol.* **1975**, *85*, 101–111. [[CrossRef](#)] [[PubMed](#)]
66. Medina, D.; Shepherd, F.; Gropp, T. Enhancement of the tumorigenicity of preneoplastic mammary nodule lines by enzymatic dissociation. *J. Natl. Cancer Inst.* **1978**, *60*, 1121–1126. [[CrossRef](#)] [[PubMed](#)]
67. Erenus, N.; Muller, J.H. Versuche uber Zuchtung von Tumorzellen aus Ascites. *Gynaecologia* **1948**, *126*, 13–18. [[PubMed](#)]
68. Nadel, E.M.; Greenberg, J. Synergistic inhibitory action of a-methopterin and a diaminopyrimidine upon leukemia l1210 in mice. *Cancer Res.* **1953**, *13*, 865–868. [[PubMed](#)]
69. Barretina, J.; Caponigro, G.; Stransky, N.; Venkatesan, K.; Margolin, A.A.; Kim, S.; Wilson, C.J.; Lehar, J.; Kryukov, G.V.; Sonkin, D.; et al. The cancer cell line encyclopedia enables predictive modelling of anticancer drug sensitivity. *Nature* **2012**, *483*, 603–607. [[CrossRef](#)] [[PubMed](#)]
70. Drake, W.P.; Pendergrast, W.J., Jr.; Kramer, R.E.; Mardiney, M.R., Jr. Enhancement of spontaneous c3h/hej mammary tumorigenesis by long-term polyadenylic-polyuridylic acid therapy. *Cancer Res.* **1975**, *35*, 3051–3053.
71. Mahler, J.F.; Stokes, W.; Mann, P.C.; Takaoka, M.; Maronpot, R.R. Spontaneous lesions in aging fvb/n mice. *Toxicol. Pathol.* **1996**, *24*, 710–716. [[CrossRef](#)]
72. Schechter, J.E.; Felicio, L.S.; Nelson, J.F.; Finch, C.E. Pituitary tumorigenesis in aging female c57bl/6j mice: A light and electron microscopic study. *Anat. Rec.* **1981**, *199*, 423–432. [[CrossRef](#)] [[PubMed](#)]
73. Anisimov, V.N.; Popovich, I.G.; Zabezhinski, M.A.; Egormin, P.A.; Yurova, M.N.; Semenchenko, A.V.; Tyndyk, M.L.; Panchenko, A.V.; Trashkov, A.P.; Vasiliev, A.G.; et al. Sex differences in aging, life span and spontaneous tumorigenesis in 129/sv mice neonatally exposed to metformin. *Cell Cycle* **2015**, *14*, 46–55. [[CrossRef](#)] [[PubMed](#)]
74. Baldrick, P.; Reeve, L. Carcinogenicity evaluation: Comparison of tumor data from dual control groups in the cd-1 mouse. *Toxicol. Pathol.* **2007**, *35*, 562–569. [[CrossRef](#)] [[PubMed](#)]
75. Prochazka, M.; Gaskins, H.R.; Shultz, L.D.; Leiter, E.H. The nonobese diabetic scid mouse: Model for spontaneous thymomagenesis associated with immunodeficiency. *Proc. Natl. Acad. Sci. USA* **1992**, *89*, 3290–3294. [[CrossRef](#)] [[PubMed](#)]
76. Nci Dictionary of Cancer Terms: Solid Tumor. Available online: <https://www.cancer.gov/publications/dictionaries/cancer-terms/def/solid-tumor> (accessed on 16 February 2019).
77. Koren, S.; Bentires-Alj, M. Breast tumor heterogeneity: Source of fitness, hurdle for therapy. *Mol. Cell* **2015**, *60*, 537–546. [[CrossRef](#)] [[PubMed](#)]
78. Jantscheff, P.; Esser, N.; Graeser, R.; Zirolu, V.; Kluth, J.; Unger, C.; Massing, U. Liposomal gemcitabine (gemlip)-efficient drug against hormone-refractory du145 and pc-3 prostate cancer xenografts. *Prostate* **2009**, *69*, 1151–1163. [[CrossRef](#)] [[PubMed](#)]
79. Jantscheff, P.; Zirolu, V.; Esser, N.; Graeser, R.; Kluth, J.; Sukolinskaya, A.; Taylor, L.A.; Unger, C.; Massing, U. Anti-metastatic effects of liposomal gemcitabine in a human orthotopic lncap prostate cancer xenograft model. *Clin. Exp. Metastasis* **2009**, *26*, 981–992. [[CrossRef](#)] [[PubMed](#)]
80. Graeser, R.; Bornmann, C.; Esser, N.; Zirolu, V.; Jantscheff, P.; Unger, C.; Hopt, U.T.; Schaechtele, C.; von Dobschuetz, E.; Massing, U. Antimetastatic effects of liposomal gemcitabine and empty liposomes in an orthotopic mouse model of pancreatic cancer. *Pancreas* **2009**, *38*, 330–337. [[CrossRef](#)] [[PubMed](#)]
81. Medscape: Gemzar-gemcitabine. 2018. Available online: <https://reference.medscape.com/drug/infugem-gemzar-gemcitabine-342218> (accessed on 16 February 2019).
82. Jantscheff, P.; Schaefer-Obodozie, C.; Moor, S.; Weber, H. Pd-1, anti-pd-l1 and anti-ctla-4 checkpoint inhibitor treatment leads to different responses in syngeneic tumor models. [abstract]. In *Proceedings of the 107th Annual Meeting of the American Association for Cancer Research, New Orleans, LA, USA, 16–20 April 2016*; AACR: Philadelphia, PA, USA, 2016; p. 76, abstract nr 3216.

83. Ostuni, R.; Kratochvill, F.; Murray, P.J.; Natoli, G. Macrophages and cancer: From mechanisms to therapeutic implications. *Trends Immunol.* **2015**, *36*, 229–239. [[CrossRef](#)]
84. Kimura, Y.; Sumiyoshi, M. Antitumor and antimetastatic actions of dihydroxycoumarins (esculetin or fraxetin) through the inhibition of m² macrophage differentiation in tumor-associated macrophages and/or g1 arrest in tumor cells. *Eur. J. Pharmacol.* **2015**, *746*, 115–125. [[CrossRef](#)]
85. Sugimoto, M.; Mitsunaga, S.; Yoshikawa, K.; Kato, Y.; Gotohda, N.; Takahashi, S.; Konishi, M.; Ikeda, M.; Kojima, M.; Ochiai, A.; et al. Prognostic impact of m² macrophages at neural invasion in patients with invasive ductal carcinoma of the pancreas. *Eur. J. Cancer* **2014**, *50*, 1900–1908. [[CrossRef](#)] [[PubMed](#)]
86. Lissbrant, I.F.; Stattin, P.; Wikstrom, P.; Damber, J.E.; Egevad, L.; Bergh, A. Tumor associated macrophages in human prostate cancer: Relation to clinicopathological variables and survival. *Int. J. Oncol.* **2000**, *17*, 445–451. [[CrossRef](#)] [[PubMed](#)]
87. Ma, Y.Y.; He, X.J.; Wang, H.J.; Xia, Y.J.; Wang, S.L.; Ye, Z.Y.; Tao, H.Q. Interaction of coagulation factors and tumor-associated macrophages mediates migration and invasion of gastric cancer. *Cancer Sci.* **2011**, *102*, 336–342. [[CrossRef](#)] [[PubMed](#)]
88. Yoshikawa, K.; Mitsunaga, S.; Kinoshita, T.; Konishi, M.; Takahashi, S.; Gotohda, N.; Kato, Y.; Aizawa, M.; Ochiai, A. Impact of tumor-associated macrophages on invasive ductal carcinoma of the pancreas head. *Cancer Sci.* **2012**, *103*, 2012–2020. [[CrossRef](#)] [[PubMed](#)]
89. Kim, Y.G.; Udayanga, K.G.; Totsuka, N.; Weinberg, J.B.; Nunez, G.; Shibuya, A. Gut dysbiosis promotes m2 macrophage polarization and allergic airway inflammation via fungi-induced pge(2). *Cell Host Microbe* **2014**, *15*, 95–102. [[CrossRef](#)] [[PubMed](#)]
90. Ho-Yen, C.M.; Jones, J.L.; Kermorgant, S. The clinical and functional significance of c-met in breast cancer: A review. *Breast Cancer Res.* **2015**, *17*, 52. [[CrossRef](#)] [[PubMed](#)]
91. Rohan, R.M.; Fernandez, A.; Udagawa, T.; Yuan, J.; D'Amato, R.J. Genetic heterogeneity of angiogenesis in mice. *FASEB J.* **2000**, *14*, 871–876. [[CrossRef](#)] [[PubMed](#)]
92. Marmiroli, P.; Riva, B.; Pozzi, E.; Ballarini, E.; Lim, D.; Chiorazzi, A.; Meregalli, C.; Distasi, C.; Renn, C.L.; Semperboni, S.; et al. Susceptibility of different mouse strains to oxaliplatin peripheral neurotoxicity: Phenotypic and genotypic insights. *PLoS ONE* **2017**, *12*, e0186250. [[CrossRef](#)] [[PubMed](#)]
93. Vikis, H.G.; Jackson, E.N.; Krupnick, A.S.; Franklin, A.; Gelman, A.E.; Chen, Q.; Piwnica-Worms, D.; You, M. Strain-specific susceptibility for pulmonary metastasis of sarcoma 180 cells in inbred mice. *Cancer Res.* **2010**, *70*, 4859–4867. [[CrossRef](#)] [[PubMed](#)]
94. Workman, P.; Balmain, A.; Hickman, J.A.; McNally, N.J.; Rohas, A.M.; Mitchison, N.A.; Pierrepont, C.G.; Raymond, R.; Rowlatt, C.; Stephens, T.C.; et al. Ukcccr guidelines for the welfare of animals in experimental neoplasia. *Lab. Anim.* **1988**, *22*, 195–201. [[CrossRef](#)]
95. Rubio-Viqueira, B.; Jimeno, A.; Cusatis, G.; Zhang, X.; Iacobuzio-Donahue, C.; Karikari, C.; Shi, C.; Danenberg, K.; Danenberg, P.V.; Kuramochi, H.; et al. An in vivo platform for translational drug development in pancreatic cancer. *Clin. Cancer Res.* **2006**, *12*, 4652–4661. [[CrossRef](#)] [[PubMed](#)]
96. Mangsbo, S.M.; Sandin, L.C.; Anger, K.; Korman, A.J.; Loskog, A.; Totterman, T.H. Enhanced tumor eradication by combining ctla-4 or pd-1 blockade with cpv therapy. *J. Immunother.* **2010**, *33*, 225–235. [[CrossRef](#)] [[PubMed](#)]
97. Pachter, L. Models for Transcript Quantification from RNA-Seq. *arXiv* **2011**, arXiv:1104.3889v2.



Type of the Paper (Article- Supplementary Data)

Mouse-Derived Isograft (MDI) *in vivo* Tumor Models

I. Spontaneous sMDI Models: Characterization and Cancer Therapeutic Approaches

- Supplementary Data -

Peter Jantscheff ^{1a*}, **Janette Beshay** ^{1a}, **Thomas Lemarchand** ², **Cynthia Obodozie** ¹, **Christoph Schächtele** ¹, **Holger Weber** ^{1,*}

¹In Vivo Pharmacology, Proqinase GmbH, Breisacher Str. 117, 79106 Freiburg, Germany, peter.jantscheff@t-online.de; Janette_Beshay@web.de; c.obodozie@proqinase.com; c.schaechtele@proqinase.com; h.weber@proqinase.com

²TPL Pathology Labs, Sasbacher Str. 10, 79111 Freiburg, Germany, lemarchand@tpl-path-labs.com

*Correspondence: peter.jantscheff@t-online.de; Tel: +49-7666-913-0396; h.weber@proqinase.com ; Tel.: +49-761-769996-17331733

^aPeter Jantscheff and Janette Beshay contributed equally to this work.

Received: date; Accepted: date; Published: date

1. Supplementary Data

Suppl_data_sMDI_cMDI_models – Cancers.docx – containing:

1.1 Tab. S1 – sMDI_RNA-Seq

p 02

Tab. S1a - sMDI_RNA-Seq: Expression of tyrosine kinase receptor (TKR) genes in selected sMDI JA-0009, and cMDI JA-2011 and JA-2042

Tab. S1b - sMDI_RNA-Seq: Expression of immune population marker genes (T-, B-, NK-cells, Mφ, myeloid cells) in selected sMDI JA-0009, and cMDI JA-2011 and JA-2042

Tab. S1c - sMDI_RNA-Seq: Expression of IFN-γ signature genes in selected sMDI JA-0009, and cMDI JA-2011 and JA-2042

1.2 Fig. S1 – sMDI_RNA-Seq

p 07

Fig. S1a i – iii – sMDI_RNA-Seq: FPKM-Values

Fig. S1b i – iii – sMDI_RNA-Seq: Internal Relative Expression

1.3 Doc. S1-sMDI: sMDI - Histological and Pathological Analysis

p 11

The document summarizes detailed histopathological analysis of primary and derived tumors of various sMDI models inclusive respective large microphotographs

1.4 Doc. S2-sMDI

p 58

Material, Methods & Results: Efficacy studies with anti-mPD-1 and anti-mCTLA-4 in seven syngeneic standard mouse tumor models

1.5 Fig. S2-sMDI

p 59

Efficacy studies with anti-mPD-1 and anti-mCTLA-4 in seven syngeneic standard mouse tumor models

1.6 Doc. S3-sMDI

p 61

Methods & Results: Establishment, efficacy study and flow cytometric characterization of mPD-1-resistant MC38-CEA relapsed subline

1.7 Fig. S3-sMDI

p 62

Establishment, efficacy study and flow cytometric characterization of mPD-1-resistant MC38-CEA relapsed subline

1.1 Tab. S1 – sMDI_RNA-Seq

Tab. S1a - sMDI_RNA-Seq: Expression of tyrosine kinase receptor (TKR) genes in selected sMDI JA-0009, and cMDI JA-2011 and JA-2042

Gene	Gene description	Gene expression (FPKM values)					
		JA-0009		JA-2011		JA-2042	
		sample 1	sample 2	sample 1	sample 2	sample 1	sample 2
Kdr	kinase insert domain protein receptor, VEGF-R2	8.579	10.474	7.432	13.084	6.298	8.009
Fgfr1	fibroblast growth factor receptor 1	122.697	138.217	166.383	137.789	112.092	118.213
Fgfr2	fibroblast growth factor receptor 2	1.146	0.031	4.227	2.491	0.937	1.072
Pdgfrb	platelet derived growth factor receptor, beta	40.534	34.803	60.614	51.228	62.505	72.651
Met	met proto-oncogene	120.096	83.597	24.139	30.064	33.087	36.542
Ret	ret proto-oncogene	0.225	0.179	1.058	0.653	0.076	0.084
Flt3	FMS-like tyrosine kinase 3	0.378	0.276	0.240	0.292	1.259	1.437
Axl	AXL receptor tyrosine kinase	172.031	163.433	203.023	210.440	261.356	242.636
Kit	KIT proto-oncogene receptor tyrosine kinase	2.162	1.856	4.323	5.736	5.162	6.012
Egfr	epidermal growth factor receptor	7.592	7.015	9.604	11.132	13.700	15.918
Alk	anaplastic lymphoma kinase	0.087	0.166	0.010	0.021	0.073	0.112
Ephb4	Eph receptor B4	28.023	25.817	13.665	10.399	22.000	24.307
ErbB2	erb-b2 receptor tyrosine kinase 2	7.034	6.063	9.046	7.539	7.018	6.076
ErbB4	erb-b2 receptor tyrosine kinase 4	0.000	0.000	0.000	0.000	0.000	0.000
Igf1r	insulin-like growth factor I receptor	9.052	9.258	8.474	7.896	8.069	8.482
Mst1r	macrophage stimulating 1 receptor (c-	1.309	0.488	4.416	3.608	1.397	0.656
Tek	TEK receptor tyrosine kinase, TIE2	3.116	4.038	12.923	14.449	1.985	2.598
Flt4	FMS-like tyrosine kinase 4, VEGF-R3	2.852	3.971	3.777	5.235	2.801	4.222

Whole transcriptome shotgun sequencing-based (RNA-Seq) Expression pattern of tyrosine kinase receptor (TKR) gene family

RNA-isolation and RNA-Seq were performed by StarSeq, Mainz, Germany as whole transcriptome shotgun sequencing analysis from samples of sMDI JA-0009 and cMDI JA-2011 and JA-2042. RNA-Seq comparisons were performed based on respective FPKM (fragments per kilobase million) values. Since we could not yet determine the definite tissue of origin of the outgrowing MDI tumors, it was not possible to compare tumor gene expression with its respective -unfortunately unknown- normal tissue equivalent. Thus, we performed these experiments as a means of proof of principle, using the example of three gene families which are related to tumor malignancy or anti-tumoral immune response in three different MDIs.

Table S1a summarizes duplicate FPKM values of eighteen genes of tyrosine kinase receptor (TKR) gene family separately determined from single RNA-Seq experiment raw data from two distinct, frozen stored tumor samples of one single passage of JA-0009, JA-2011 or JA-2042 MDI each.

Duplicate FPKM values do reflect an objective gene expression pattern within the individual MDI models. Up to 1,000-fold different expression patterns comparing FPKM values of individual TKR genes were observed. For example, anaplastic lymphoma kinase, Alk (mean FPKM: 0.126), showed very weak (less than 1,000-fold lower) expression, compared with AXL receptor tyrosine kinase, Axl (mean FPKM: 167.732), whereas erb-b2 receptor tyrosine kinase 4, Erbb4, was not expressed at all in sMDI JA-0009 model. However, since normal tissue equivalents of MDIs are unknown, one only could speculate about putative malignancy-dependent variances.

Tab. S1b– sMDI_RNA-Seq - Expression of immune population marker genes (T-, B-, NK-cells, MΦ, myeloid cells) in selected sMDI JA-0009, and cMDI JA-2011 and JA-2042

Gene	Gene description	Gene expression (FPKM values)					
		JA-0009		JA-2011		JA-2042	
		sample 1	sample 2	sample 1	sample 2	sample 1	sample 2
Ptprc	protein tyrosine phosphatase, receptor type, C, CD45	37.323	30.111	16.357	15.704	30.151	28.046
Cd19	CD19 antigen	0.017	0.086	0.025	0.000	0.245	0.111
Cd3d	CD3 antigen, delta polypeptide	0.793	0.873	0.447	0.267	3.658	3.015
Cd4	CD4 antigen	1.952	0.759	1.971	0.965	33.392	30.082
Cd8b1	CD8 antigen, beta chain 1	0.608	0.404	0.875	0.346	4.468	4.068
Foxp3	forkhead box P3	0.124	0.117	0.309	0.123	0.685	0.587
Cd44	CD44 antigen	217.964*	154.191*	80.282	88.770	113.863	115.516
Il2ra	interleukin 2 receptor, alpha chain, CD25	0.508	0.449	0.248	0.112	0.734	0.689

CD11b	integrin alpha M	59.742	47.742	33.733	44.577	22.264	21.607
Adgre1	adhesion G protein-coupled receptor E1, F4/80	35.325	30.841	25.396	23.390	75.824	67.878
Mrc1	mannose receptor, C type 1, CD206	40.398	32.636	70.140	91.794	95.140	82.647
Itgax	integrin alpha X, CD11c	7.283	3.457	3.435	3.349	7.650	7.708
Ncr1	natural cytotoxicity triggering receptor 1, NKp46	4.617	3.767	0.354	0.286	2.626	1.900
Itga2	integrin alpha 2, CD49b	5.220	3.428	1.137	1.731	1.189	1.887
Ly6C	lymphocyte antigen 6 complex, locus C1	303.057	337.000	41.151	51.858	41.983	36.347

Whole transcriptome shotgun sequencing-based (RNA-Seq) expression pattern of Immune Population Marker (IPM) gene family

Table S1b summarizes duplicate FPKM (fragments per kilobase million) values of fifteen genes of immune population marker (IPM) gene family separately determined from single RNA-Seq experiment raw data from two distinct, frozen stored tumor samples of a single passage of JA-0009, JA-2011 or JA-2042 MDI each.

Duplicate FPKM values do reflect an objective gene expression pattern within the individual MDI models (JA-0009, JA-2011, or JA-2042). Up to 1,000-fold different expression pattern comparing FPKM values of individual IPM genes were observed. For example, CD19 antigen, Cd19 (mean FPKM: 0.052), showed very weak (less than 1,000-fold lower) expression, compared with CD44 antigen, Cd44 (mean FPKM: 186.078), or lymphocyte antigen 6 complex, locus C1, Ly6C (mean FPKM: 320.029) in sMDI JA-0009 model. However, since normal tissue equivalents of MDIs are unknown, one only could speculate about putative malignancy-dependent variances.

Tab. S1c – sMDI_RNA-Seq - Expression of IFN- γ Signature genes in selected sMDI JA-0009, and cMDI JA-2011 and JA-2042

Gene	Gene description	Gene expression (FPKM values)					
		JA-0009		JA-2011		JA-2042	
		sample 1	sample 2	sample 1	sample 2	sample 1	sample 2
Il2rg	interleukin 2 receptor subunit gamma	42.246	39.482	19.460	20.503	62.764	49.006
Cxcr6	chemokine (C-X-C motif) receptor 6	1.257	0.773	1.433	0.318	9.097	6.613
Cd3d	CD3 antigen, delta polypeptide	0.793	0.873	0.447	0.267	3.658	3.015
Cd2	CD2 antigen	1.575	0.898	0.597	0.706	4.033	2.505
Itgal	integrin alpha L	6.752	4.789	3.783	3.901	12.127	11.312

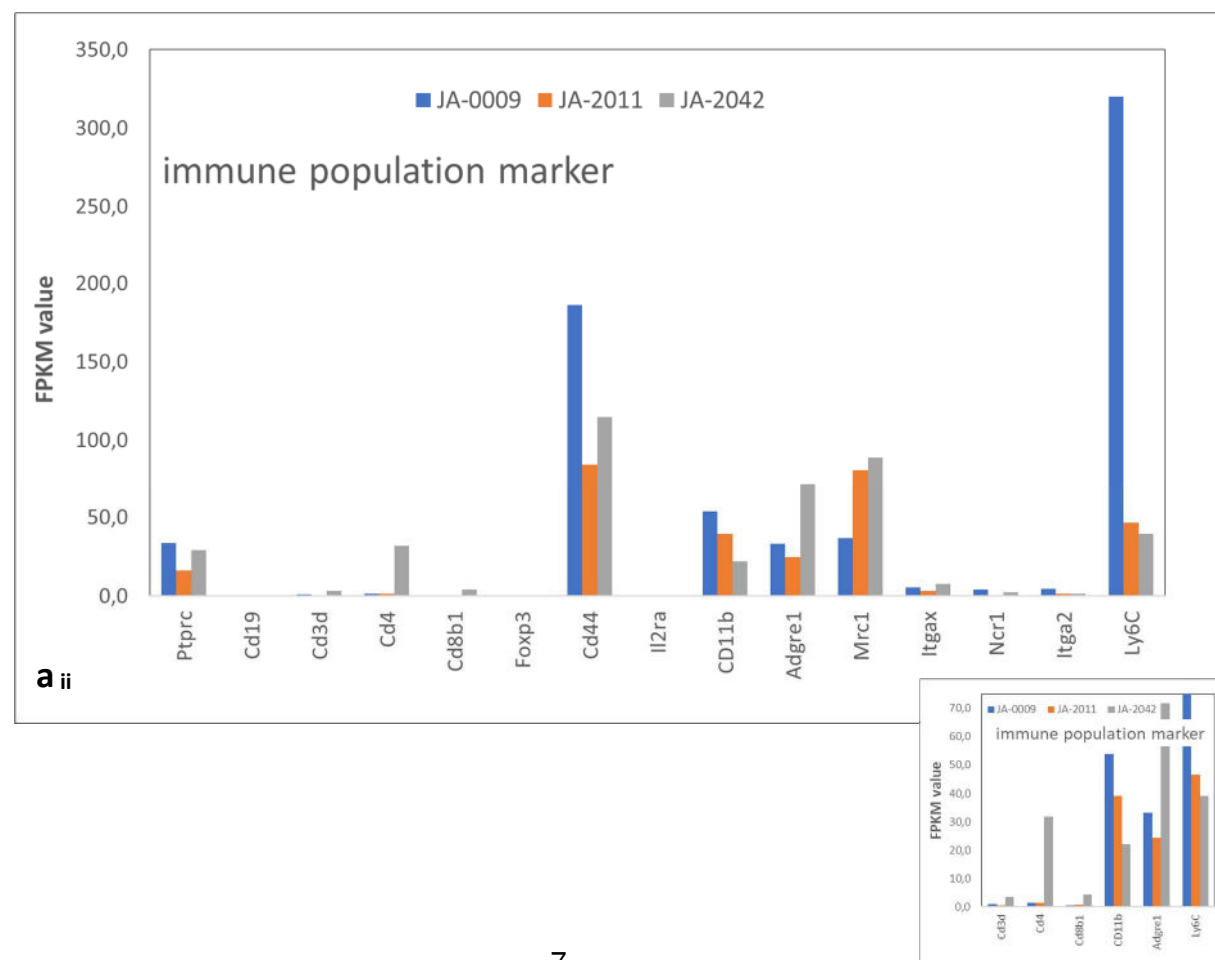
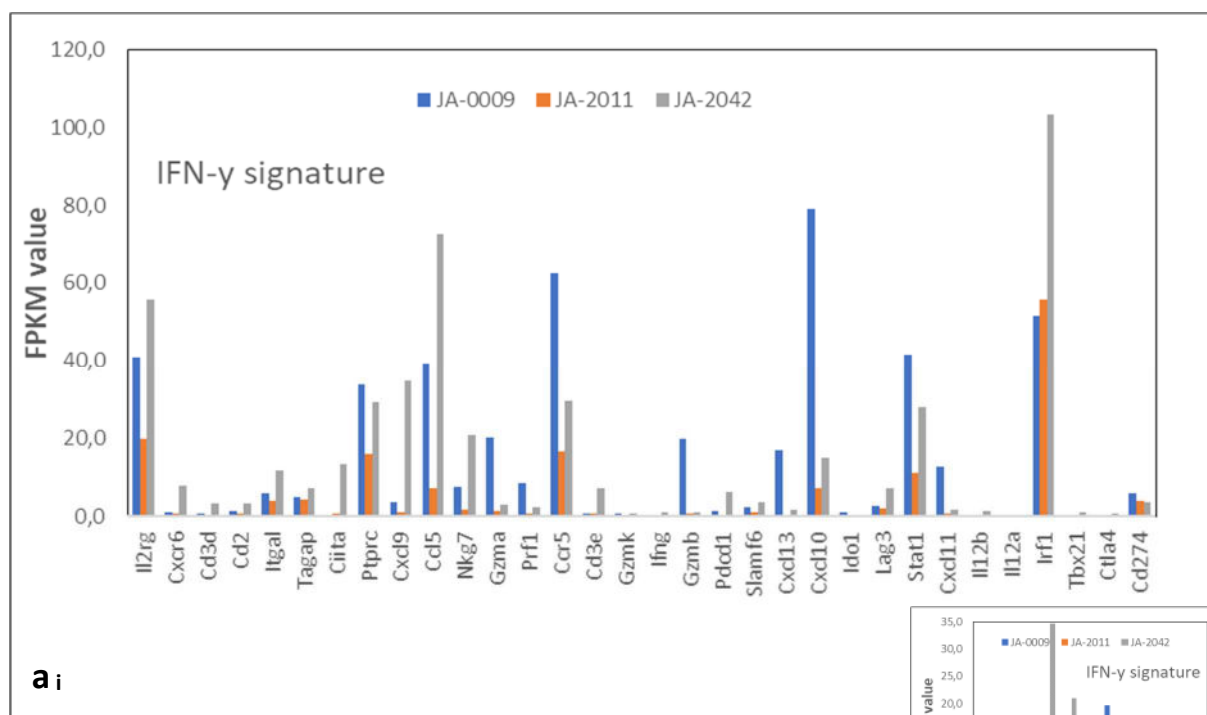
Tagap	T cell activation Rho GTPase activating protein	4.636	5.536	4.918	3.987	7.021	7.502
Ciita	class II transactivator	0.161	0.136	0.659	0.513	14.236	12.366
Ptpcr	protein tyrosine phosphatase, receptor	37.323	30.111	16.357	15.704	30.151	28.046
Cxcl9	chemokine (C-X-C motif) ligand 9	4.238	2.831	1.393	0.923	45.016	24.324
Ccl5	C-C motif chemokine ligand 5	41.223	36.996	7.127	7.141	79.711	65.278
Nkg7	natural killer cell group 7	7.640	7.409	2.421	1.104	21.513	20.296
Gzma	granzyme A	24.492	15.757	1.510	1.445	2.996	3.072
Prf1	perforin 1 (pore forming protein)	10.770	6.110	0.600	0.709	2.331	2.125
Ccr5	chemokine (C-C motif) receptor 5	63.335	62.056	15.800	17.280	30.596	28.809
Cd3e	CD3 antigen, epsilon polypeptide	0.818	0.675	1.223	0.438	7.494	6.838
Gzmk	granzyme K	0.940	0.437	0.290	0.000	0.587	1.035
Ifng	interferon gamma	0.039	0.099	0.112	0.000	1.273	0.848
Gzmb	granzyme B	26.809	12.568	0.783	0.792	1.399	0.905
Pdcd1	programmed cell death 1	1.520	1.512	0.676	0.380	6.870	5.895
Slamf6	SLAM family member 6	2.433	2.073	1.518	0.929	3.694	3.940
Cxcl13	chemokine (C-X-C motif) ligand 13	26.792	6.986	0.176	0.566	2.667	0.784
Cxcl10	chemokine (C-X-C motif) ligand 10	78.838	79.382	8.332	6.334	19.421	10.466
Ido1	indoleamine 2,3-dioxygenase 1	0.771	1.136	0.128	0.000	0.033	0.000
Lag3	lymphocyte-activation gene 3	3.108	2.039	2.392	1.374	8.097	6.592
Stat1	signal transducer and activator of transcription 1	44.663	38.088	11.567	10.864	31.248	24.513
Cxcl11	chemokine (C-X-C motif) ligand 11	14.251	11.497	0.686	0.563	2.390	0.793
Il12b	interleukin 12b	0.067	0.042	0.072	0.026	1.628	1.269
Il12a	interleukin 12a	0.218	0.092	0.052	0.056	0.119	0.000
Irf1	interferon regulatory factor 1	53.329	49.470	66.608	44.893	108.433	98.369
Tbx21	T-box 21	0.344	0.327	0.118	0.177	1.057	0.906
Ctla4	cytotoxic T-lymphocyte-associated protein 4	0.491	0.209	0.161	0.103	0.879	0.632
Cd274	CD274 antigen, PD-L1	6.746	4.850	3.991	4.090	4.693	2.803

Whole transcriptome shotgun sequencing-based (RNA-Seq) expression pattern of IFN- γ signature (IFNGS) gene family

Table S1c summarizes duplicate FPKM (fragments per kilobase million) values of thirty-two genes of IFN- γ signature (IFNGS) gene family separately determined from single RNA-Seq experiment raw data from two distinct, frozen stored tumor samples of a single passage of JA-0009, JA-2011 or JA-2042 MDI each.

Duplicate FPKM values do reflect an objective gene expression pattern within the individual MDI models (JA-0009, JA-2011, or JA-2042). Up to 1,000-fold different expression pattern comparing FPKM values of individual genes could be observed. For example, interleukin 12b, Il12b (mean FPKM: 0.054), showed very weak (less than 1,000-fold lower) expression, compared with chemokine (C-X-C motif) ligand 10, Cxcl10 (mean FPKM: 79.110) in sMDI JA-0009 model. However, since normal tissue equivalents of MDIs are unknown, one only could speculate about putative malignancy-dependent variances.

1.2 Fig. S1 – *sMDI_RNA-Seq*



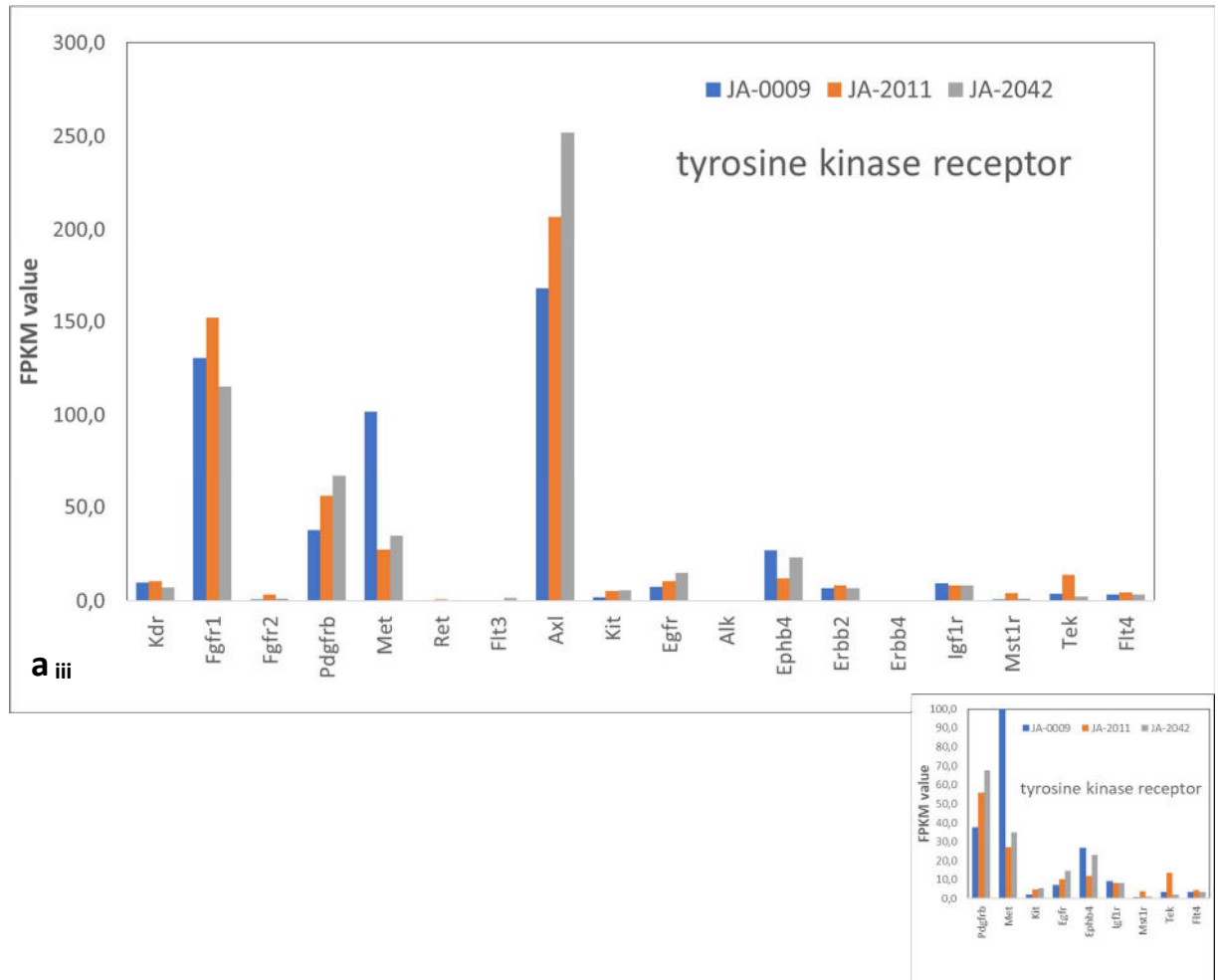
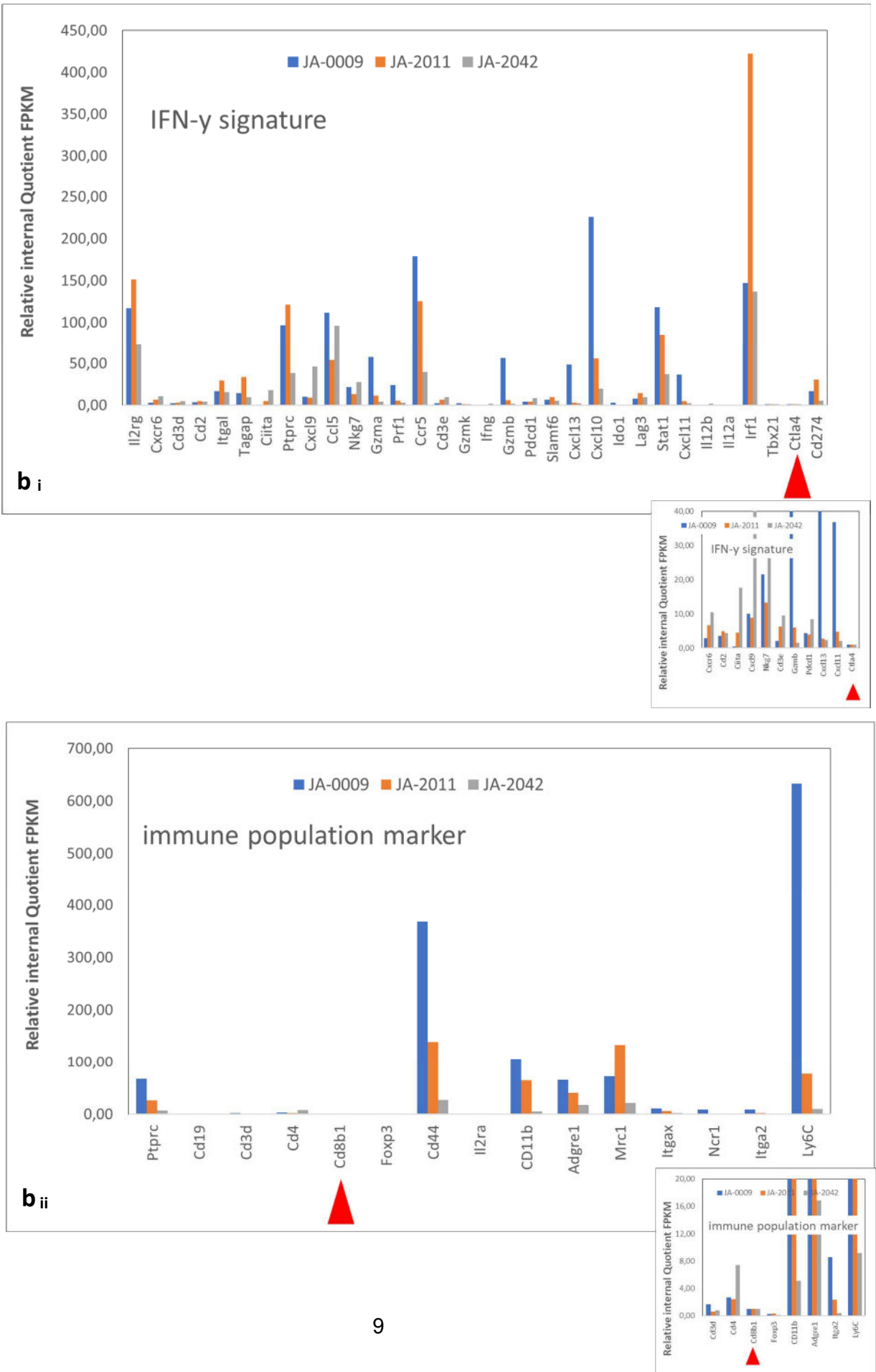


Fig. S1a – sMDI_RNA-Seq: FPKM-Values

Graphical presentation of RNA-seq determined FPKM-Values of various genes of three gene families in three MDI (one sMDI, and two cMDI) models. The observed expression pattern for most tested IFNGS (i), IPM (ii), and TKR (iii) genes was similar in all three MDI models, with high gene expression (FPKM values > 100) of some, low or moderate (FPKM values between 1 – 50) of most other, and not detectable expression (FPKM value = 0) of some further genes. Since the FPKM (fragments per kilobase million) values were not determined in simultaneous experiments a direct comparison of gene expression between the individual MDI models was not possible. Thus, we compared internal relative gene expression (Figs. S1b) in the various models. Small inserts show gene expression of selected gene with other y-axis scaling.

Fig. S1b – sMDI_RNA-Seq: Internal Relative Expression



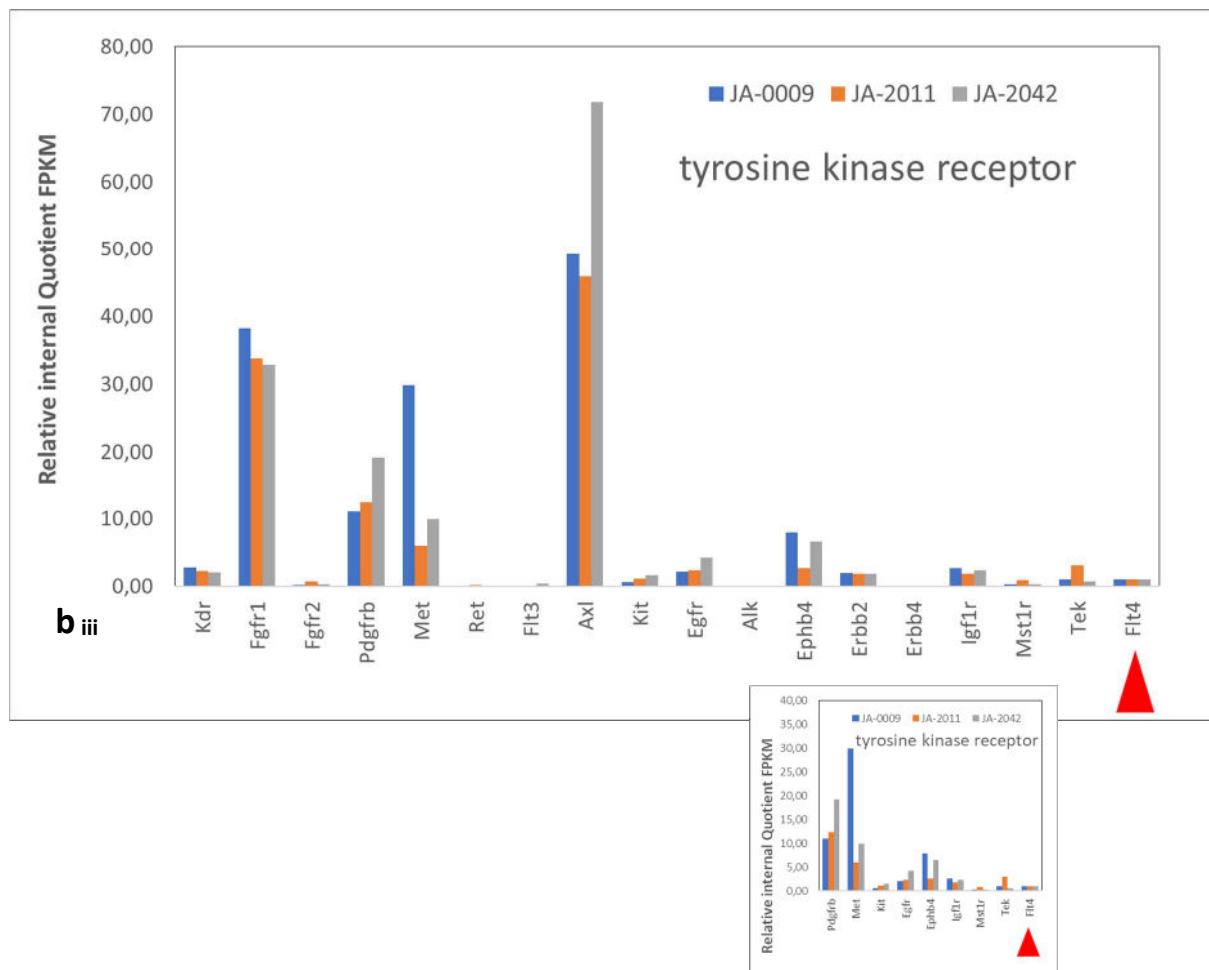


Fig. S1b – sMDI_RNA-Seq: Internal Relative Expression

Graphical presentation of Internal Relative Expression (IRE) of RNA-seq determined FPKM-Values of various genes of three gene families in the three (one sMDI, and two cMDI) MDI models. The IRE gives one an impression on the strength and variabilities of single gene expression within one gene family of the individual MDI models. IRE was calculated as quotient comparing individual gene expression (FPKM) within individual MDI models each, related to the expression of an internal, low FPKM-value reference gene (red triangle). Data are shown as n-fold of expression of respective reference gene. For each gene family one common reference gene, Ctl4 (IFN γ signature), Cd8b1 (immune population marker), and Flt4 (tyrosine kinase receptor) was selected within the MDI models. Relative tumor specific gene expression (IRE) in the individual MDI tumors, JA-0009, JA-2011, and JA-2042 shows that in some cases genes, i.e. Fgfr1 (TKR), display a very similar relative expression, whereas in other cases, i.e. Irfl (IFNGS), Ly6C (IPM), or Met and Axl (TKR), respectively, relative gene expression in the various models differs strikingly. Small inserts show gene expression of selected gene with other y-axis scaling.

1.3 Doc. S1 - sMDI: sMDI - Histological and Pathological Analysis

The document summarizes detailed histopathological analysis of primary and derived tumors of various sMDI models inclusive respective large microphotographs

Doc. S1-sMDI

Pathological investigations on index and recipient mice with the present sMDI tumors:

Table of Contents

JA-0011 sMDI: Histiocytic Sarcoma (HS) / Histiocyte-associated Lymphoma (HAL)	14
JA-0013 sMDI: Malignant Lymphoma (ML).....	22
JA-0018 sMDI: Malignant Lymphoma (ML).....	27
JA-0034 sMDI: Malignant Lymphoma (ML).....	29
JA-0021 sMDI: Malignant Lymphoma (ML).....	31
JA-0009 sMDI: Adenocarcinoma, anaplastic, invasive	35
JA-0017 sMDI: Adenocarcinoma, complex type	42
JA-0023 sMDI: Adenocarcinoma, mammary gland	46
JA-0032 sMDI: Adenocarcinoma, Lung.....	56
Literature cited:	58

List of Figures

Figure 1: Macroscopic aspects of the JA-0011 neoplasm index case.....	14
Figure 2: Index case 011-14, DBA/2N ♀, histiocytic tumor microscopic aspect in liver I.....	15
Figure 3: Index case 011-14, DBA/2N ♀, histiocytic tumor microscopic aspect in liver II.....	16
Figure 4: Index case 0011-14; aspects the histiocytic sarcoma in the kidney.....	17
Figure 5: Index case 011-14, DBA/2N ♀, histiocytic tumor aspect in oviduct.....	18
Figure 6: Case 011-14/1298-16, DBA/2N ♀, tumor microscopic aspect in spleen.....	19
Figure 7: Case 011-14/0052-17, DBA/2N ♀, histiocytic tumor: microscopic aspect in liver	20
Figure 8: Lineage derived tumor 0052-17: aspect of tumor lineage in the spleen.....	21
Figure 9: Macroscopic aspects of index case of tumor line JA-0013	22
Figure 10: Index case of JA-0013: high magnification view of the neoplastic tissue	23
Figure 11: Lineage case of JA-0013: 0026-17 high magnification view of the neoplastic tissue ...	24
Figure 12: Lineage case of JA-0013: 1562-16 high magnification view of the neoplastic tissue ...	25
Figure 13: Lineage case of JA-0013: 0027-17 medium magnification view of the neoplastic tissue	26

Figure 14:	Macroscopic aspect of JA-0018 (case 18-14).....	27
Figure 15:	Index neoplasm of sMDI JA-0018 (15-14) noted in the lungs of a ♀ CBA/J mouse.....	27
Figure 16:	Low, medium and high magnification of 0113-17 malignant lymphoma (ML) derived from index case 0018-14 tumor, subcutis, adipose and mammary.....	28
Figure 17:	Macroscopic aspect of JA-0034	29
Figure 18:	Low and high magnification of the malignant lymphoma (ML) index 0034-14	30
Figure 19:	Medium magnification of the daughter malignant lymphoma case 1426-17	30
Figure 20:	Spontaneous neoplasm study (study #10445): normal skin tissue with a mammary teat, female mouse 0021/14	31
Figure 21:	Early malignant lymphoma localization in a lymph node – Index 0021-14.....	32
Figure 22:	Spontaneous neoplasms (study #10445): malignant lymphoma, female SCID <i>bg/bg</i> mouse 1571/16	33
Figure 23:	Macroscopic aspects of the index tumor 009-14 (index case for lineage JA-0009).....	35
Figure 24:	Medium high magnification of the tumor index case 009-14, with glandular and anaplastic/ spindle shaped differentiation.....	36
Figure 25:	High magnification of the tumor index case 009-14, with clear evidence of epidermoid differentiation, suggesting an epidermoid carcinoma	37
Figure 26:	A moderate high magnification view of 009-14 showing spindle shaped cell differentiation	38
Figure 27:	Low magnification view of the index neoplasia 009-14	39
Figure 28:	Low magnification aspect of the transmitted tumor 1286/16 from index case 09-14.	40
Figure 29:	High magnification aspect of the transmitted tumor 1286/16.....	41
Figure 30 :	Gross aspects of the index neoplasm 0017-14.....	42
Figure 31:	Image ID: 780_#10445_tu01_0017-14_0017-14_HE_10x_1-AdK--mixed tumor-index-case, HE stain, original magnification: 100x.....	43
Figure 32:	Image ID: 780_#10445_tu_0017-14_1234-16_HE_20x_2-AdK-wKeratinization-mixed tumor-complex-myoepith-epith2ImesenchT-wC, HE stain, original magnification: 200x	44
Figure 33:	Image ID: 780_#10445_tu01_0096-17_0017-14_HE_20x_2-AdK--mixed tumor- trab-K, HE stain, original magnification: 200x.	45
Figure 34:	Low (left) and mid (right) magnification views of the index tumor from the kidney....	47
Figure 35:	High magnification view of the index renal tumor.....	47
Figure 36:	Index tumor of the subcutaneous tumor: microscopic morphological aspects	48
Figure 37:	Lineage tumor aspect in subcutaneous tissue: example of 0005-17	49
Figure 38:	Case 0005-17: High magnification reveals the tubulopapillary structure with necrotic cells in lumens and supportive stroma.....	50
Figure 39:	Lineage tumor aspect in kidney: example of 0001-17	51
Figure 40:	Lineage tumor aspect in subcutaneous tissue: example of 1620-16	52
Figure 41:	Spontaneous neoplasms (study #10445): papillary cystic adenocarcinoma, female mouse 0547/17, hematoxylin and eosin stain, subcutis.....	53

Figure 42:	Spontaneous neoplasms (study #10445): papillary cystic adenocarcinoma, female mouse 0544/17, skin	54
Figure 43:	Spontaneous neoplasms (study #10445): papillary adenocarcinoma, lung, male mouse 0032/14	56
Figure 44:	Spontaneous neoplasms (study #10445): adenocarcinoma, solid, clear cells, subcutis, male mouse 0055/17	57
Figure 45:	Low magnification of tumor aspect overview and high view detail (thumbnails)	58

JA-0011 sMDI: Histiocytic Sarcoma (HS) / Histiocyte-associated Lymphoma (HAL)

Index tumor **JA-0011** (Fig. 2) was classified as a histiocytic sarcoma (HS) or histiocyte-associated lymphoma (HAL), as localized in several tissues (liver, gut, kidney, spleen – see [Figure 1](#) to [Figure 5](#)), with both histiocytic and lymphocytic components. Re-transplanted subcutaneous tumors, **0339-17**, **4007-16**, or **0057-17** also invaded spleens e.g. **1298-16** ([Figure 6](#)) and/or livers e.g. **0052-17** ([Figure 7](#)) of recipient mice, with either lymphoblastic (e.g. **1298-16**) or histiocytic predominant differentiation. These features are topographical and histological characteristics of these hemolymphopoietic neoplasms.

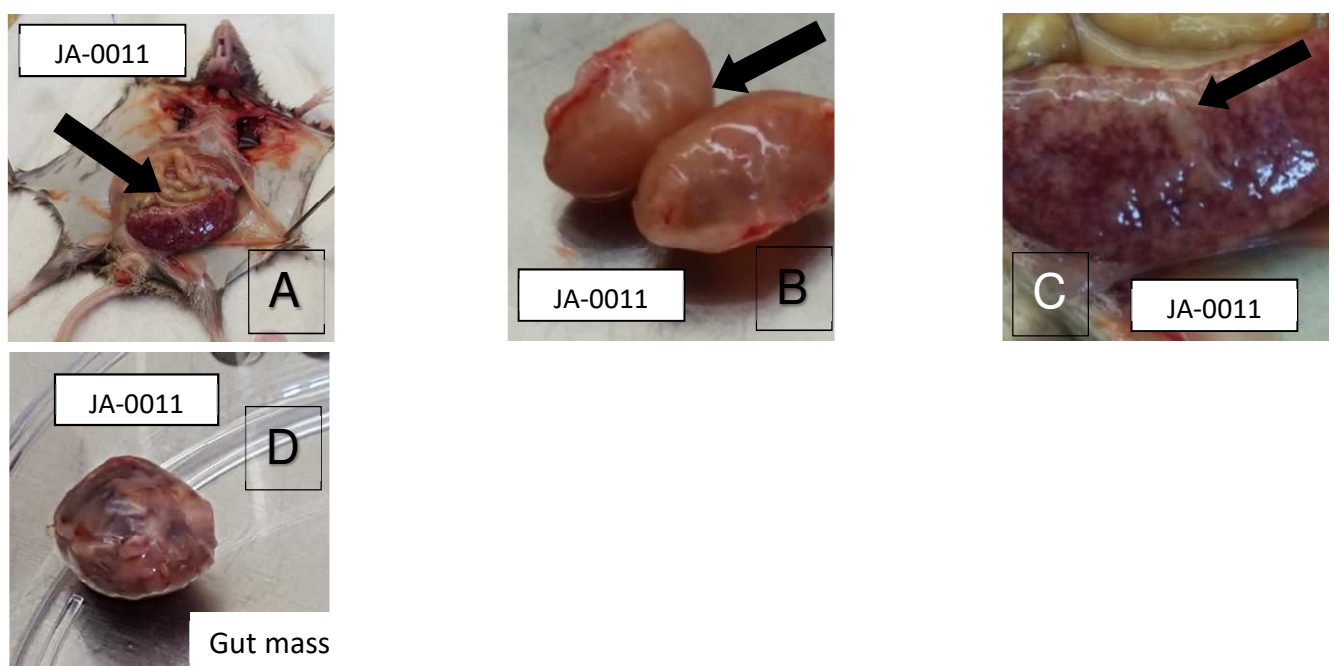


Figure 1: Macroscopic aspects of the **JA-0011** neoplasm index case

A: the spleen is markedly enlarged (**arrow**) and the liver pale yellow and enlarged. **B:** Kidneys are also paler than normal and enlarged; one kidney has segmental more important pale discoloration (**arrow**) **C:** Close up view of the spleen (see A), showing the white mottling (**arrow**) discoloration. **D:** mass noted in the abdominal cavity, of obvious tumoural origin, but without identifiable tissue of origin.

Diagnosis: Neoplasm of Hemolymphopoietic origin: most compatible with: histiocytic sarcoma (HS) or histiocyte-associated lymphoma (HAL)

Main features: multicentric tumor composed of sheets and bundles of histiocytic cells in various tissues, including, but not limited to spleen, liver, kidney, oviducts, with:

- presence of syncytial multinucleate cells (Hallmark of the neoplasm)
- significant infiltration of neoplastic cells by polymorphonuclear leukocytes (neutrophils, eosinophils), often immature (band granulocytes) erythropoietic cells and lymphoid cells
- presence of inflammation

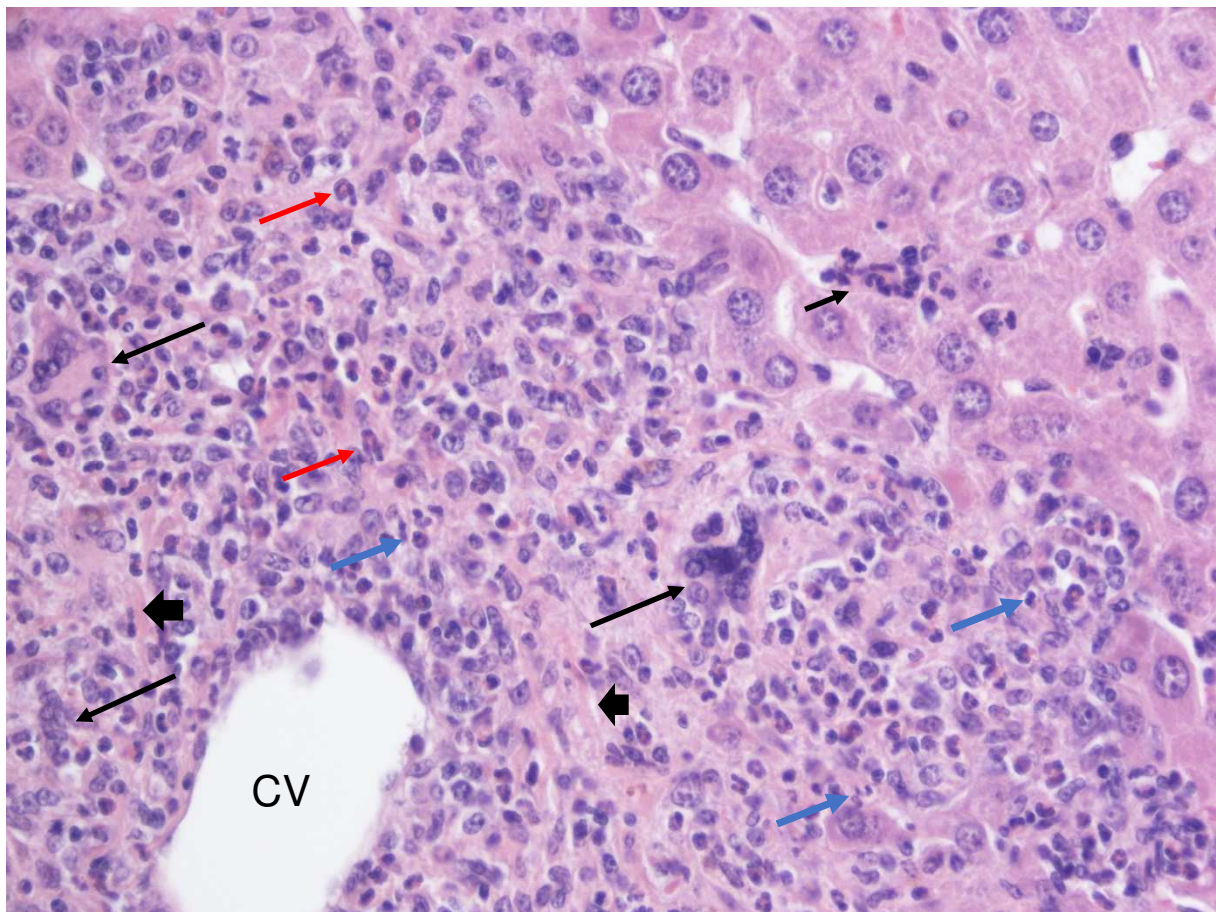


Figure 2: Index case 011-14, DBA/2N ♀, histiocytic tumor microscopic aspect in liver I

The malignant proliferation is characterized by sheets and bundles of pale macrophage-like histiocytic cells, which progressively compress, invade and replace the hepatic parenchyma and by the presence of many multinucleate giant cells (**long black arrows**). There is also relatively significant associated inflammation and/or recruited mixed leukocytes, a majority of which is characterized by histiocytes/macrophages infiltrates cytologically within normal limits, a few of which in a necrotic/degenerated form (small black arrow in the upper left quadrant area). Accompanying this histiocytic and macrophagic proliferation, are significant infiltrates of polymorphonuclear (PMN) leukocytes, associating both neutrophils (**blue arrows**) and some eosinophils (**red arrows**). On this particular high magnification view centered on a central vein (**CV**), the neoplastic proliferation (cell type) is not particularly obvious. The neoplastic process is chronic (probably relatively indolent/slow growing neoplasm), as judged by the associated florid fibrosis accompanying the predominantly granulomatous-like inflammation (see arrowhead **◄**).

Index case: mouse ID number 011-14, strain DBA/2N ♀, HE stain, original magnification: 400x.

Morphological diagnosis: Histiocytic Sarcoma/ Histiocyte-associated lymphoma.

Abbreviation: HS/HAL

Image ID: 780_#10445_liver_0011-14_HE_40x_1_syncytial-giant-cell_inflammation

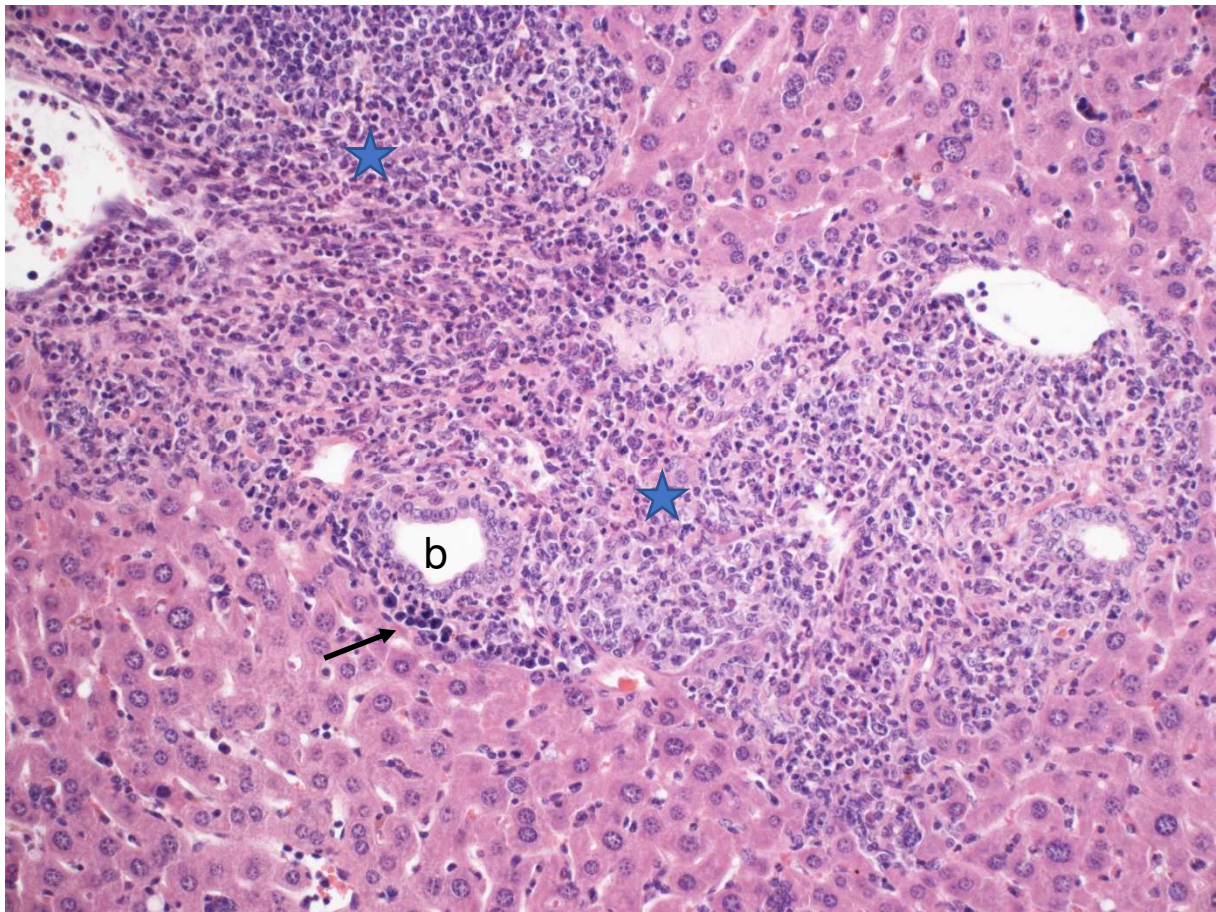


Figure 3: Index case 011-14, DBA/2N ♀, histiocytic tumor microscopic aspect in liver II

Index case: mouse ID number 011-14, strain DBA/2N ♀ same case as in [Figure 2](#); HE stain, original magnification 200x.

The portal areas of the liver have diffuse marked mononuclear and histiocytic diffuse infiltration of the connective tissue ([blue stars](#)), with a significant population of large blastic cells and cells most compatible morphologically with small lymphocytes. The mixed inflammatory cell infiltration is similar in intensity and type to [Figure 2](#). There is also associated erythropoiesis (extramedullary hematopoiesis – **black arrow**). b = small bile duct.

Morphological diagnosis: Histiocytic Sarcoma/ Histiocyte-associated lymphoma.

Abbreviation: HS/HAL

Image ID: 780_#10445_liver_0011-14_Liver_HE_20x_1_HS_pport-area.

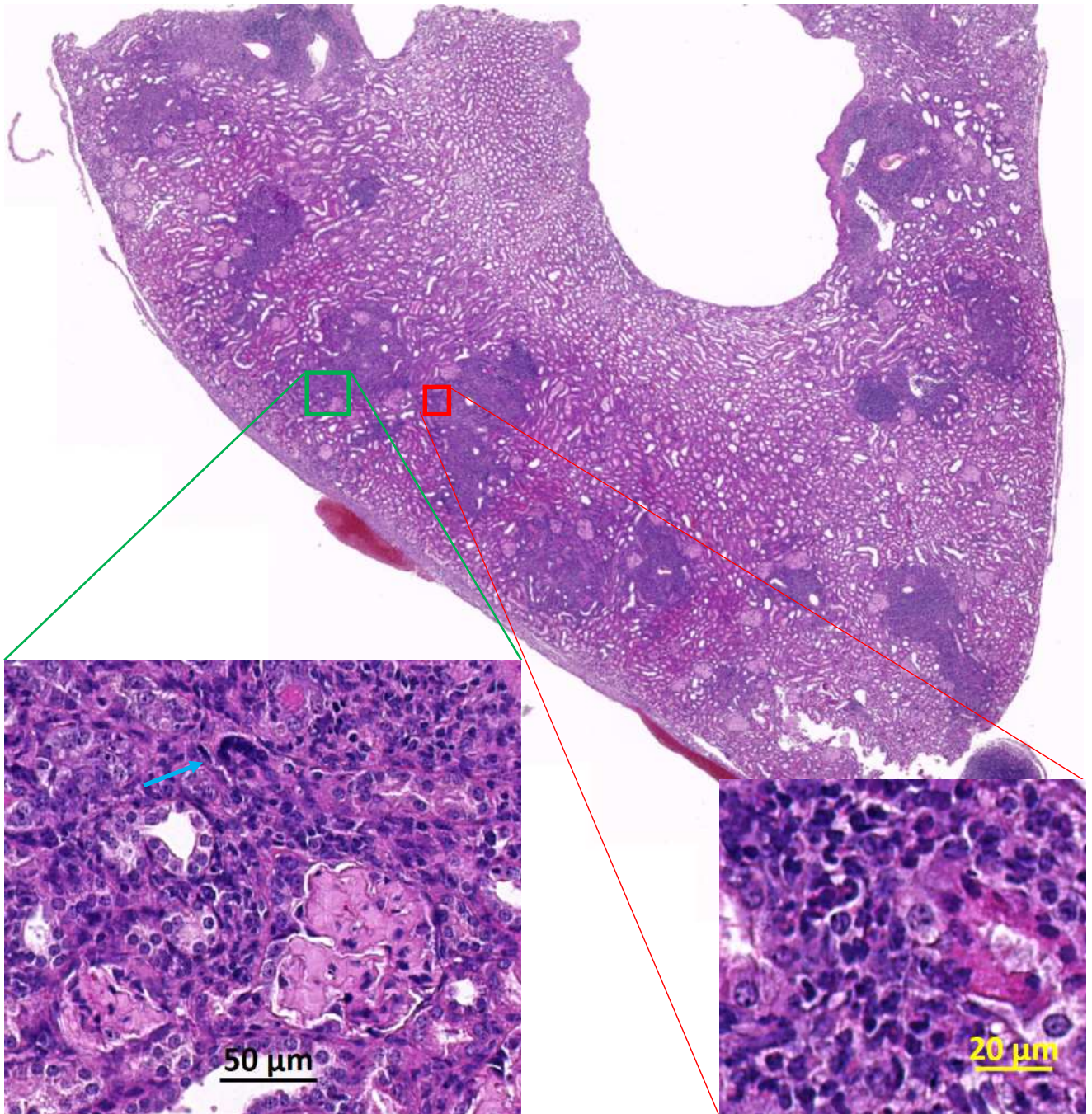


Figure 4: Index case 0011-14; aspects the histiocytic sarcoma in the kidney

Similar foci as in the liver (indicating secondary localizations) are scattered in the cortex of the kidney cortex, with glomerular hyalinosis (left green inset) and features of infiltrating cells similar to the liver: presence of multi-nucleate giant cells (blue arrow), and various proportions of histiocytes, granulocytes and small lymphocytes (right small red inset) with evidence of associated tubular degeneration and regeneration.

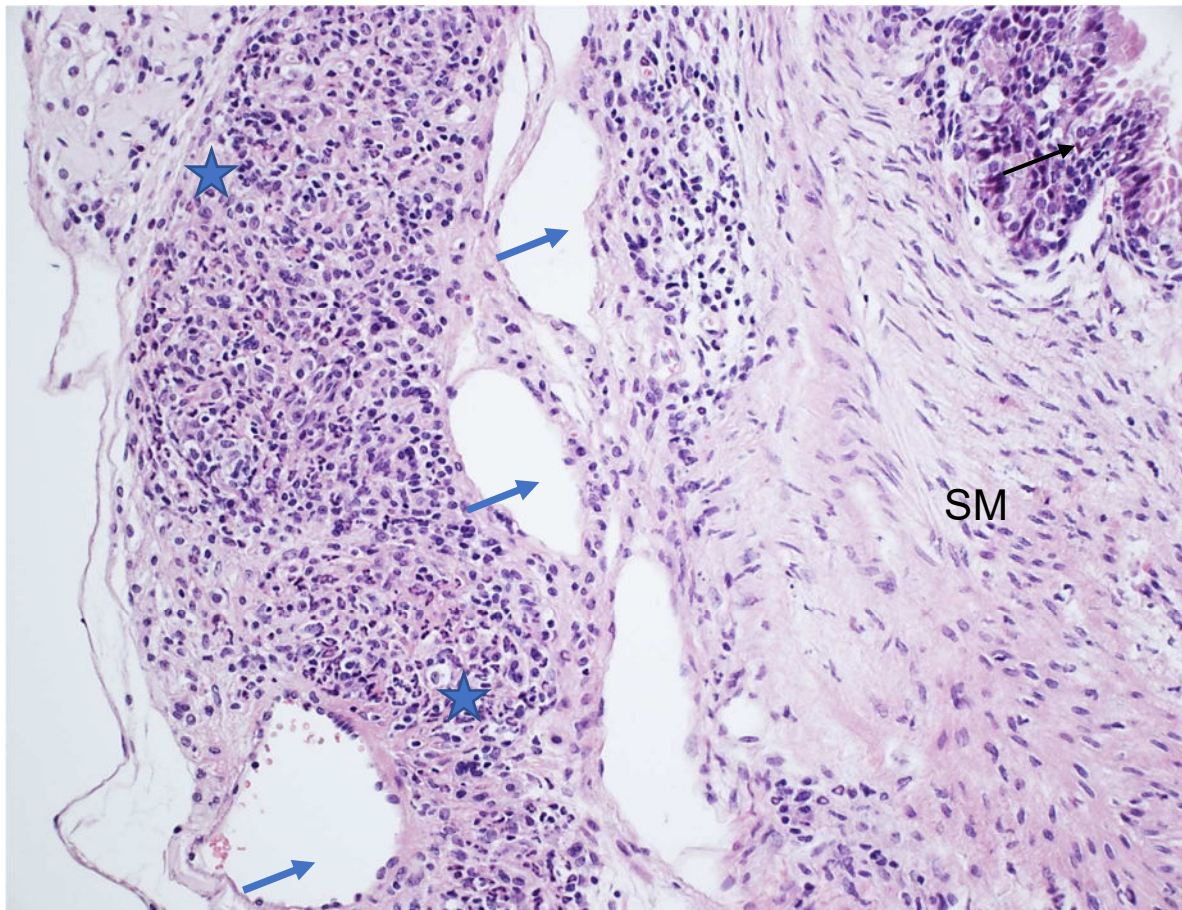


Figure 5: Index case 011-14, DBA/2N ♀, histiocytic tumor aspect in oviduct.

Index case: mouse ID number 011-14, strain DBA/2N ♀, HE stain, original magnification: 400x

Cavitory organ composed of a smooth muscle wall and ciliated pseudostratified epithelium (**black arrow**): Female reproductive tract, most compatible with oviduct.

A proliferative infiltrate similar to liver (see [Figure 2](#) and [Figure 3](#)) and kidney is noted (**blue stars**), markedly thickening the serosal surface of a cavitory organ most compatible with oviduct adjacent to ovary. This proliferative tissue induces marked dilatation of blood and lymph vessels (**blue arrows**). SM = smooth muscle layer of the oviduct.

Consequently, it may be surmised that the intestinal mass was most probably a heavily invaded ovary (see [Figure 1](#) panel D). Ovary is a frequent primary or secondary localization of histiocytic sarcoma (see [Reference 1](#))

Morphological diagnosis: Histiocytic Sarcoma/ Histiocyte-associated lymphoma.

Abbreviation: HS/HAL

Image ID: 780_#10445_ORG_0011-14_Darm_HE_40x_1_HS

Isografts – example 1: 1298-16

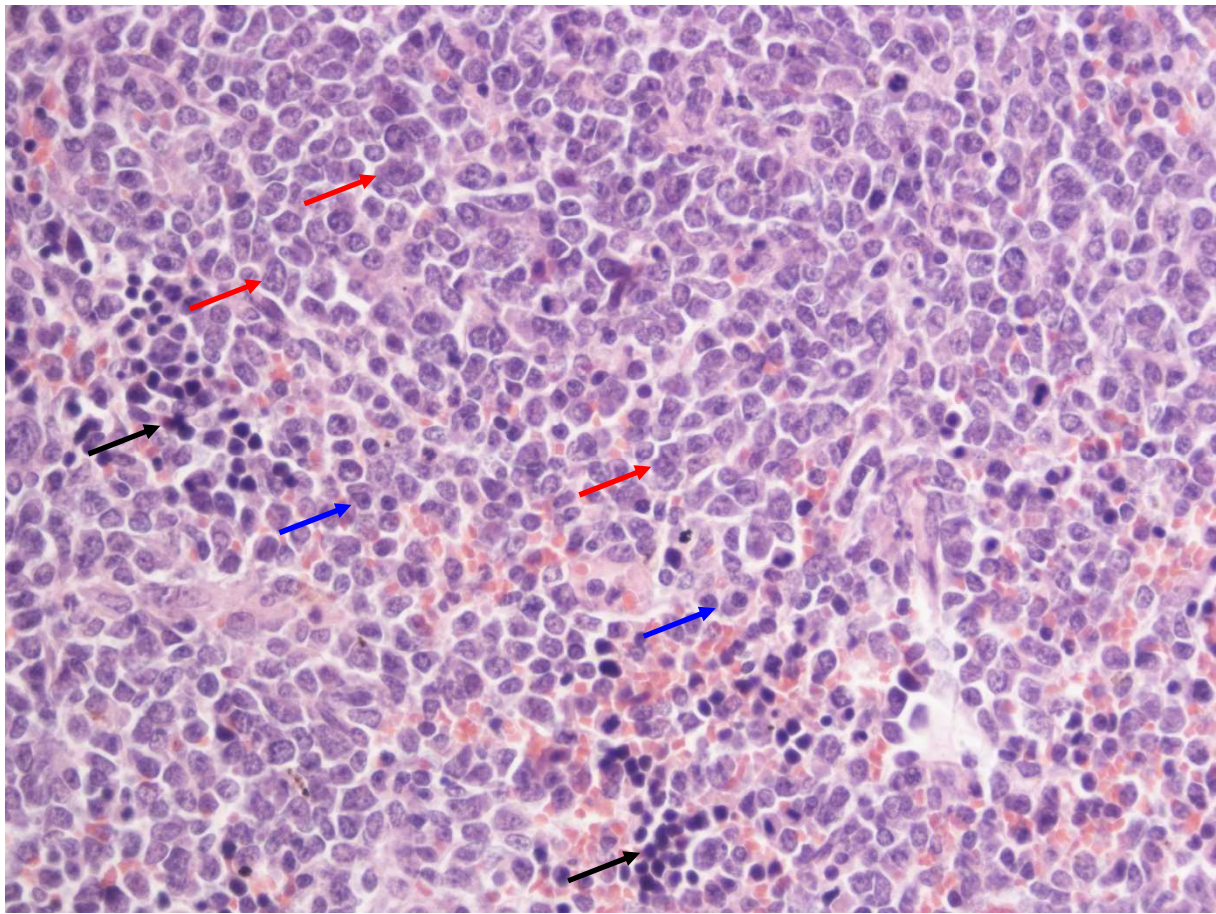


Figure 6: Case 011-14/1298-16, DBA/2N ♀, tumor microscopic aspect in spleen

Mouse ID #1298-16 **spleen tissue**; from index case: mouse ID number 011-14, strain DBA/2N ♀. HE stain, original magnification: 400x.

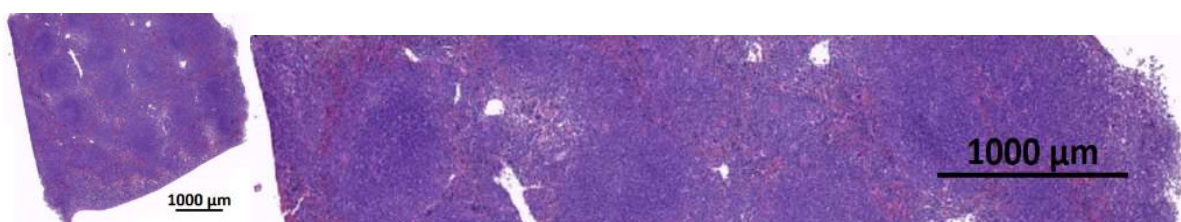
Diffusely (almost entirely) erasing the structure of the white and red pulp of the spleen are diffuse relatively homogenous sheets (see **thumbnails** below) of immature large “blastic” mononuclear cells most compatible morphologically with immature lymphoblasts (**red arrows**). Some of the differentiated cells have morphology suggesting plasma cells (**blue arrows**). There is also extramedullary erythropoiesis (**black arrows**). In this case, early infiltration in the liver features similar cells as in the spleen, with few inflammatory cells (data not shown).

This demonstrate the lymphoma potential of this particular cell lineage.

This phenotypic variability would warrant further molecular pathology characterization by immunohistochemistry and in situ hybridization when re-used in future studies

Morphological diagnosis: Malignant lymphoma.

Image ID: 780_#10445_mz_0011-14_1298-16_HE_40x_1_lymphoma



Isografts – example 2: 0052-17

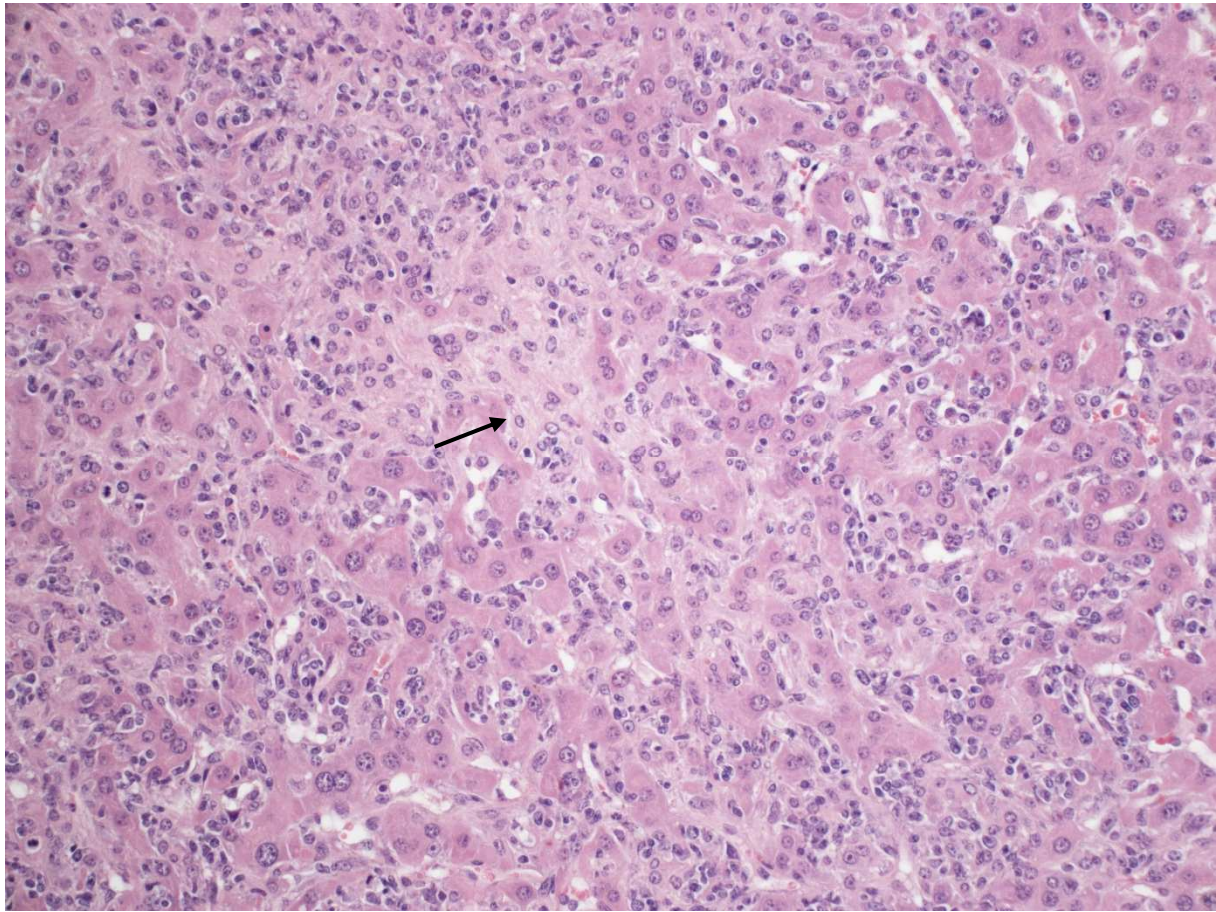


Figure 7: Case 011-14/0052-17, DBA/2N ♀, histiocytic tumor: microscopic aspect in liver

Mouse ID #0052-17; from index case: mouse ID number 011-14, strain DBA/2N ♀. HE stain, original magnification: 200x.

Notice the almost pure central proliferation of histiocytic cells widely thickening the sinusoids (**black arrow**). Histiocytes have homogenous pale nuclei and amorphous pale pink abundant cytoplasm with indistinct boundaries and low/absent anaplastic or pleomorphic features, making them as typical histiocytes/macrophages. Furthermore, these cells closely resemble typical hypertrophic Kupffer cells, replacing the normal looking fenestrated endothelial covering of sinusoids. Other cells at the vicinity are of various types, including small, mainly medium-sized and few large lymphocytes.

This phenotypic variability of this lineage JA-0011 would warrant further molecular pathology characterization by immunohistochemistry and in situ hybridization when re-used in future studies

Morphological diagnosis: Histiocytic Sarcoma/ Histiocyte-associated lymphoma.

Abbreviation: HS/HAL

Source file: Image ID: 780_#10445_leb_0011-14_0052-17_HE_20x_1_HS

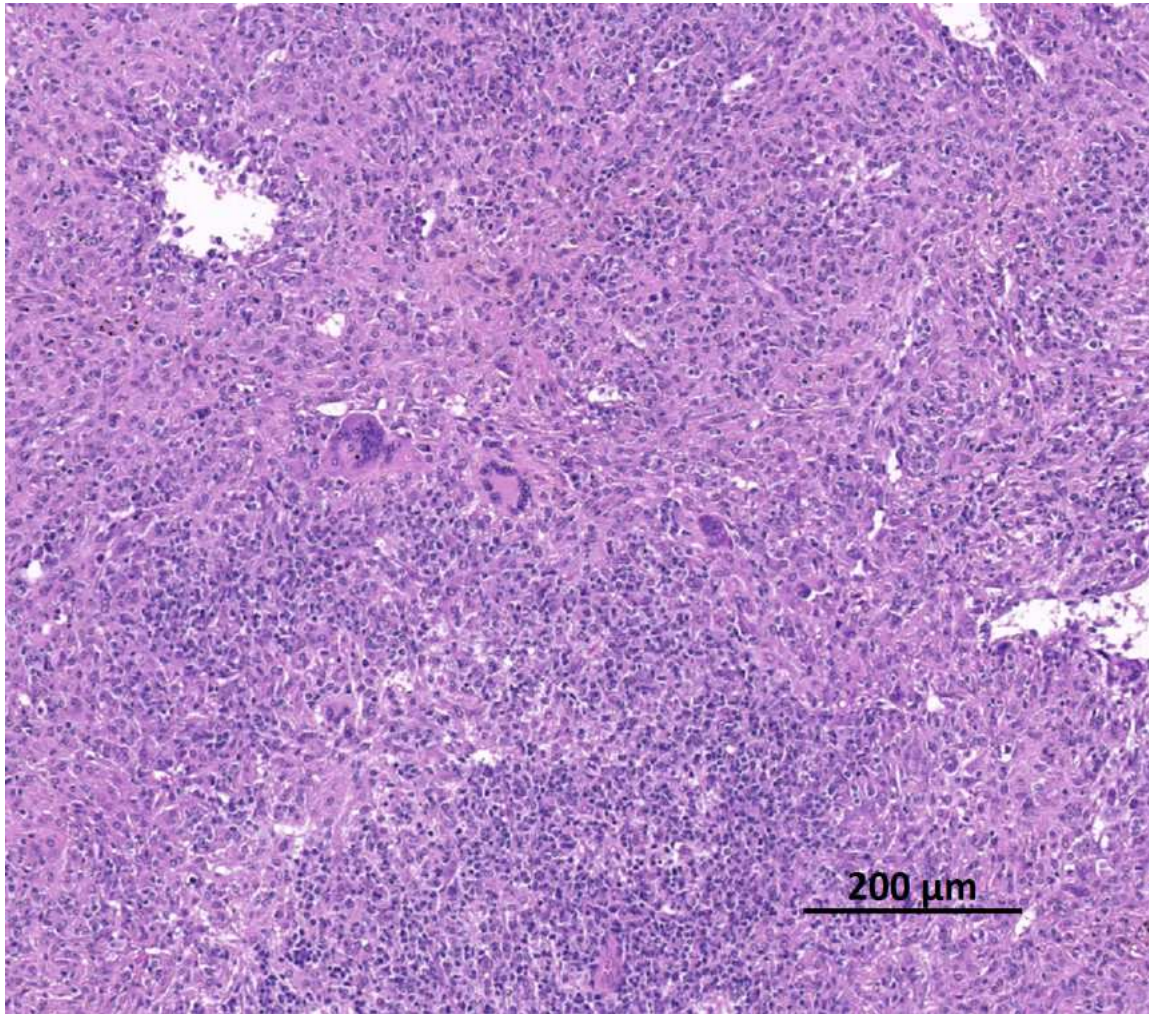
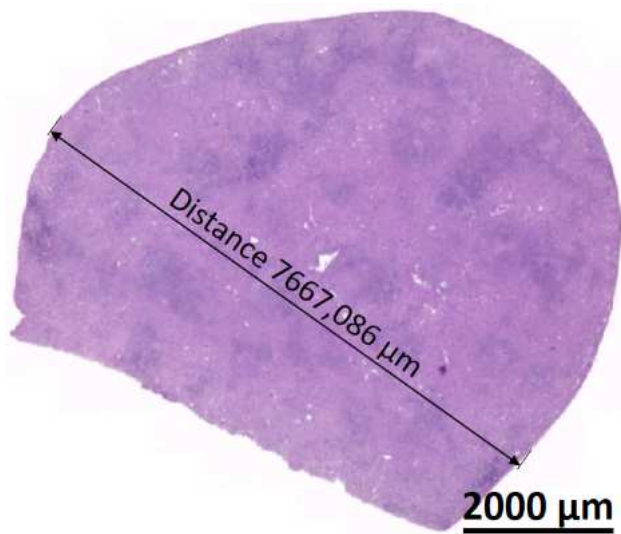


Figure 8: Lineage derived tumor 0052-17: aspect of tumor lineage in the spleen

The spleen is grossly enlarged (**see thumbnail below**) and the red pulp is diffusely invaded with sheets of histiocytic and cells with occasional to numerous giant multinucleate cells. The white pulp is also invaded and partially erased by the neoplastic process. Contrast with case in [Figure 6](#), where a malignant lymphoma is present in the spleen of case 1298-16.



JA-0013 sMDI: Malignant Lymphoma (ML)

The phenotype of tumor **JA-0013**/ as exemplified by specimens **0013-14** (index case) and mice **1562-16**, **0026-17**, **0027-17** and **0028-17** (Fig. 2) was most consistent with malignant lymphoma, which was probably of B-cell lineage, as judged by the presence of infiltration of blastic cells with immunoblastic or plasmacytic differentiation ([Figure 10](#)) plasma and Mott cells (plasma cells containing Russell bodies) and the presence of large histiocytoid cells (see [Figure 10](#)). It had a remarkable phenotypic stability (see [Figure 11](#) and [Figure 12](#)). One daughter re-transplanted tumor studied microscopically, **0027-17**, had an intriguing finding, non-neoplastic giant multinucleate giant cells, leading to suspect a possible complication with an opportunistic organism (see [Figure 13](#)).

Gross aspects were also typical of malignant lymphoma (see [Figure 9](#))

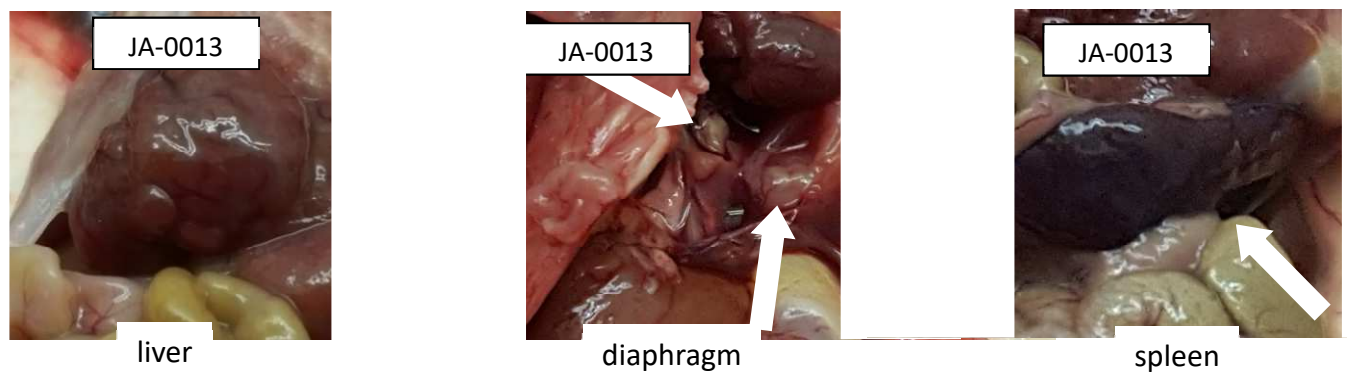


Figure 9: Macroscopic aspects of index case of tumor line **JA-0013**

There is markedly enlarged liver, 2 masses in pulmonary hilus in the thorax (behind the diaphragm) and a markedly enlarged spleen

Primary differential diagnosis: Lymphoma, lymphoblastic (with histiocytoid large cells) - most likely lineage origin: B cells

Immunohistochemistry would be useful for precise lineage definition.

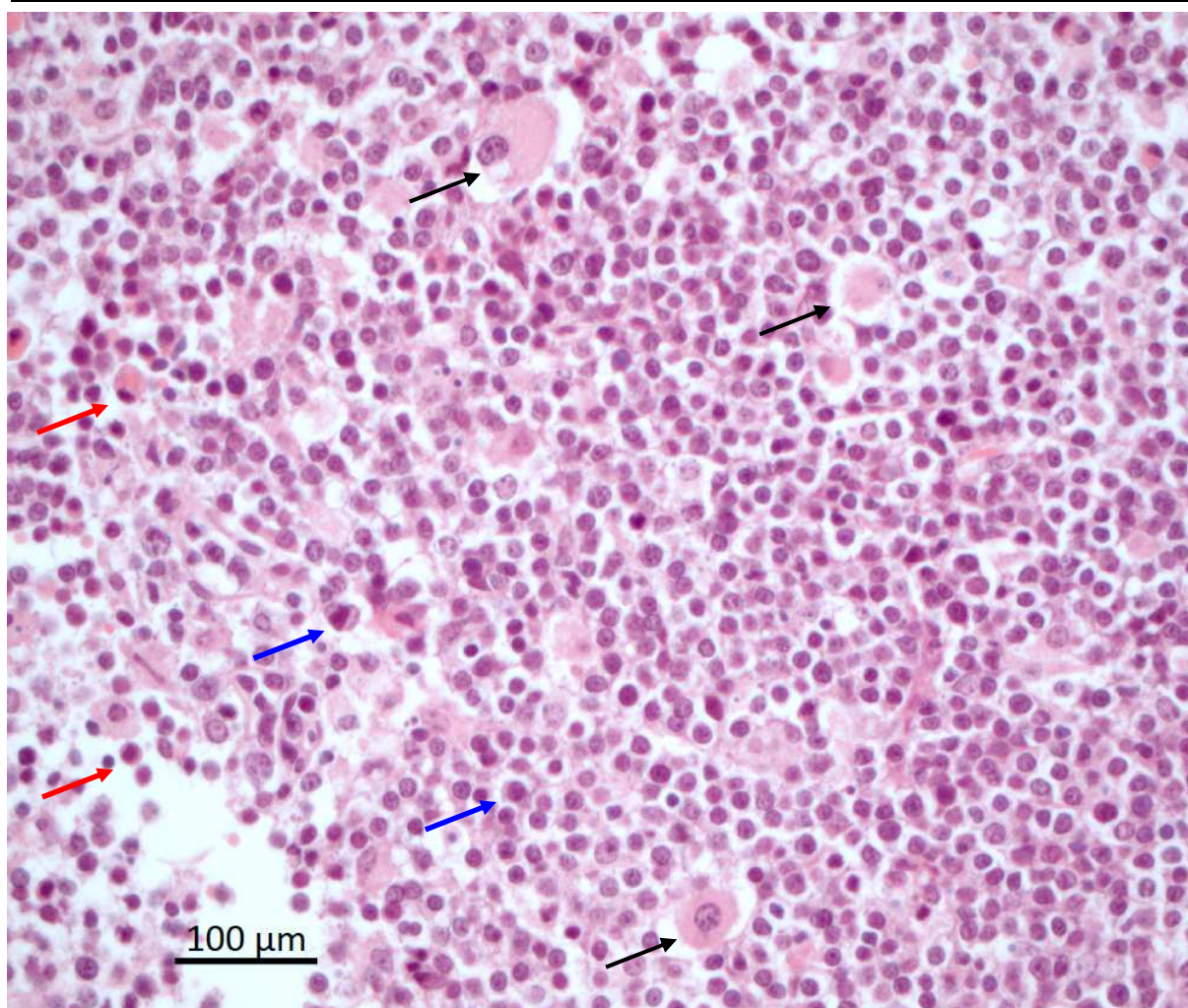


Figure 10: Index case of JA-0013: high magnification view of the neoplastic tissue

This specimen from pulmonary hilus/diaphragmatic masses exhibits sheets of malignant mid-sized blastic lymphocytes with presence of large, 50-70 μm diameter atypical cells with a pale glassy eosinophilic cytoplasm (**black arrows**). The sheets are irregularly infiltrated with smaller cells with a stem cell morphology, which could be of neoplastic origin or myeloid in origin (related to a response to anemia) and with plasmacytic cells, either neoplastic like (**blue arrows**) suggesting plasmacytic differentiation, or typical plasma cells with Russell bodies (Mott cells – see **red arrows**). Tumor infiltrating lymphocytes and other normal host inflammatory cells cannot be appraised without special molecular pathology techniques based on HE-stained sections and morphology alone.

Hematoxylin eosin stain, 400 x original magnification.

Morphological diagnosis: Malignant lymphoma.

Abbreviation: ML

Source file: 2019-01-24 19_40_09-TPL780-#10445-dia-0013-14_0013-14_1_400x_2-index-lymphoma.czi - ZEN 2.3 lite

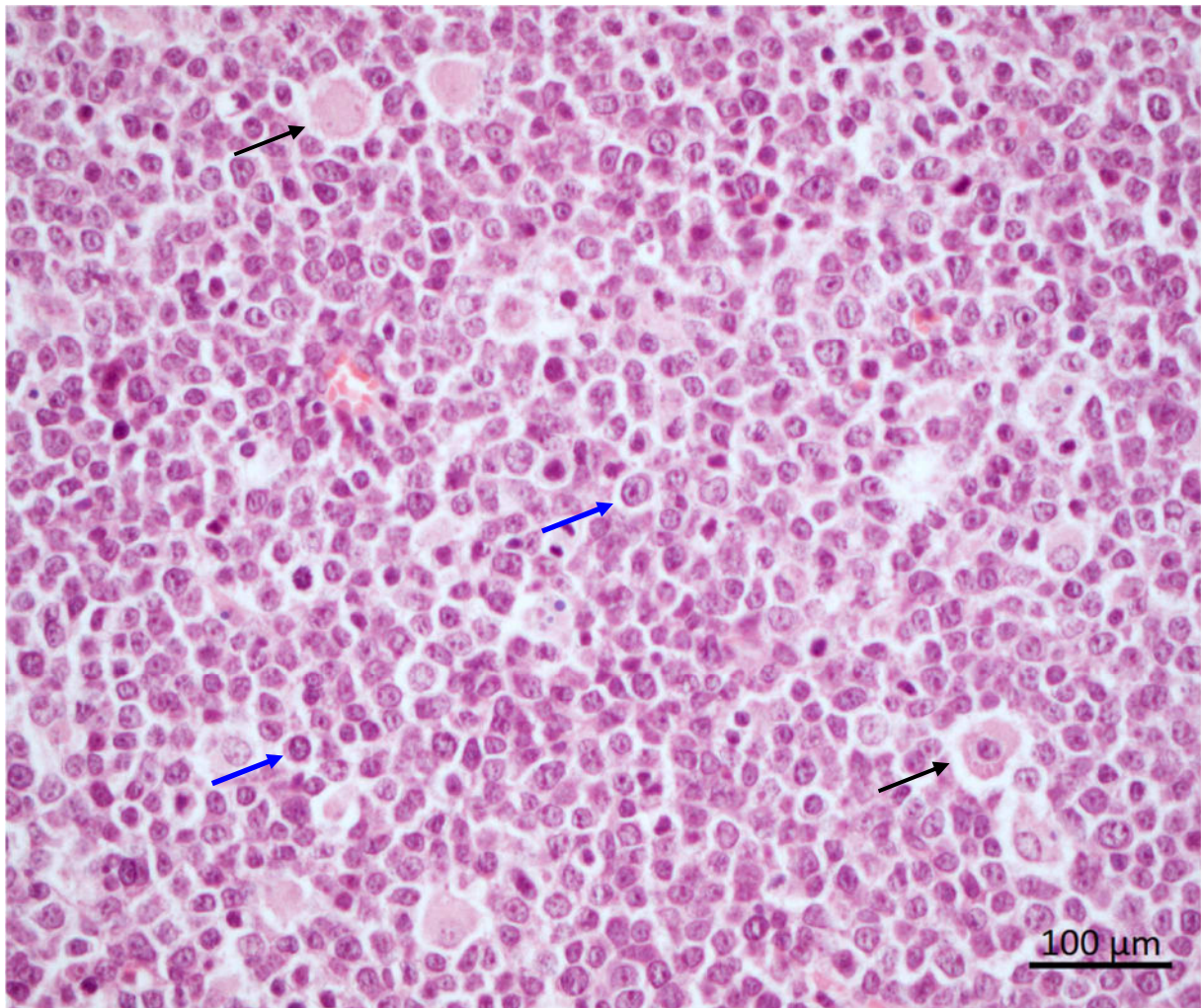


Figure 11: Lineage case of JA-0013: 0026-17 high magnification view of the neoplastic tissue

This tumor is derived from index case: 0013-14

When comparing to the index case, there is remarkable phenotypic stability in the tissue of this particular mouse, with the conservation of the large histiocytoid cells (**black arrows**) and the plasmacytic differentiation, with scant eccentric cytoplasm (**blue arrows**). All these simple morphologic features are most typical of B-cell differentiation and are indicating phenotypic stability, at least morphologically. B cell or T cell may be verified by immunohistochemistry.

Morphological diagnosis: Malignant lymphoma.

Abbreviation: ML

Cancer lineage: lymphocytes

Source file: 019-01-24 19_40_09-TPL780-#10445-dia-0013-14_0013-14_1_400x_2-index-lymphoma.czi - ZEN 2.3 lite.png

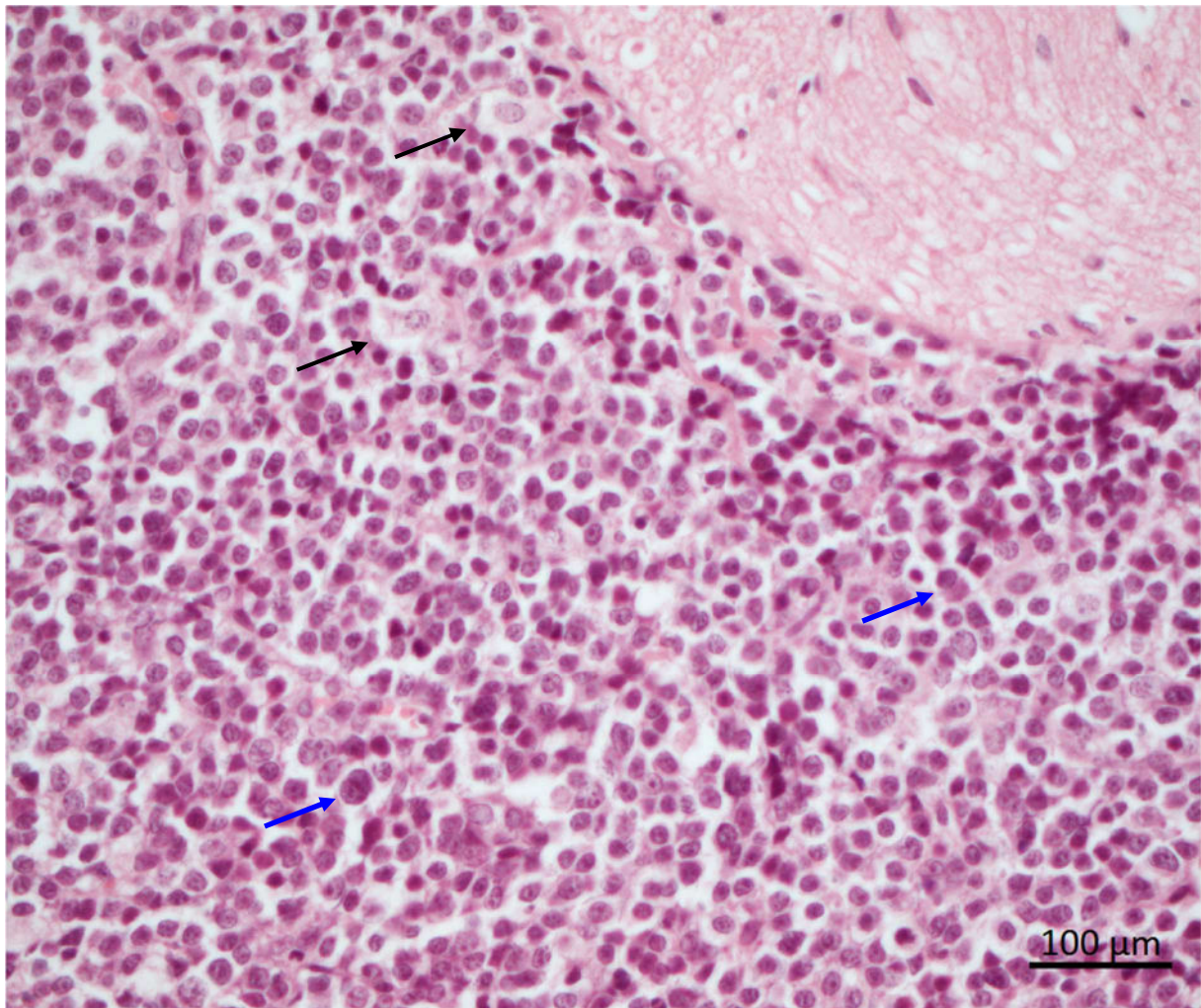


Figure 12: Lineage case of JA-0013: 1562-16 high magnification view of the neoplastic tissue

This tumor is derived from index case: 0013-14

When comparing to the index case, there is remarkable phenotypic stability in the tissue of this particular mouse, with the conservation of the large histiocytoid cells (**black arrows**) and the plasmacytic differentiation, with scant eccentric cytoplasm (**blue arrows**). All these simple morphologic features are most typical of B-cell differentiation and are indicating phenotypic stability, at least morphologically.

Morphological diagnosis: Malignant lymphoma.

Abbreviation: ML

Cancer lineage: lymphocytes

Source file: 019-01-24 20_31_32-TPL780-#10445-dia-0013-14_1562-16_1_400x_2-lymphoma-with large-histiocytic-like-.png

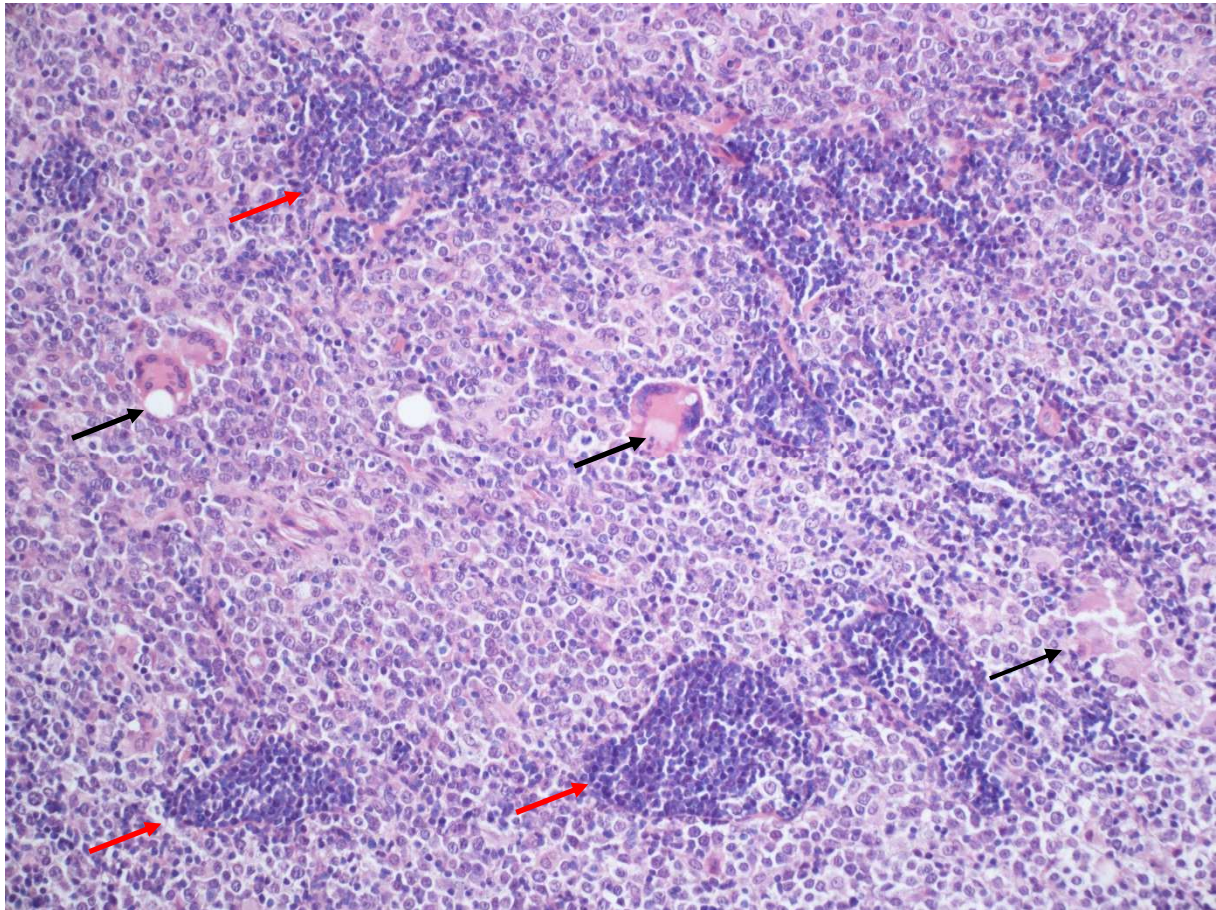


Figure 13: Lineage case of JA-0013: 0027-17 medium magnification view of the neoplastic tissue

Mouse ID #0027-17; from index case: mouse ID number 013-14, ♀ strain C57BL/6 albino.

HE stain, original magnification: 200x.

Tissue of origin: very likely lymph node (presence of lymphatic vessels – not present in the field above) and lymphatic sinuses filled with small lymphocytes (see **red arrows** – architecture partially preserved)

There is partial erasing of lymphoid architecture by homogenous sheets of round cells most compatible with proliferating (blastic) lymphocytes and scattered rare multinucleate giant cells (MGCs) that have large empty vacuoles or vacuoles containing pale amorphous pale gray material (**arrows**) and are not considered to be neoplastic.

This finding of non-neoplastic giant multinucleate giant cells is intriguing, and leads to suspect a possible complication with an opportunistic organism.

B cell markers would be useful to characterize the proliferation.

Morphological diagnosis: Malignant lymphoma.

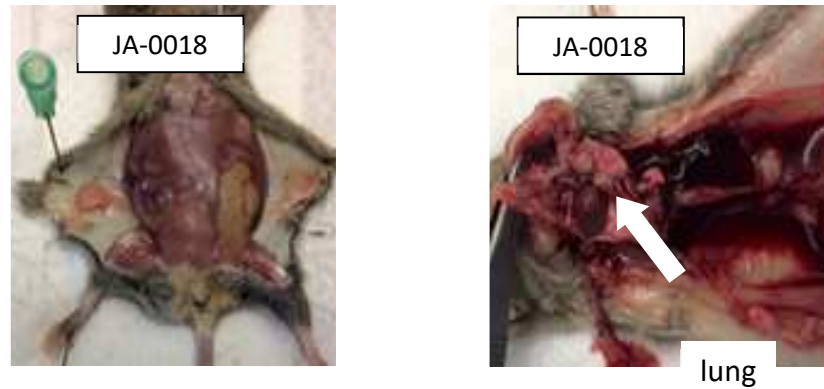
Abbreviation: ML

Image ID: 780_#10445_tu_0013-14_0027-17_1_HE_20x_1-Lymphoma-with-non-neoMGCs

JA-0018 sMDI: Malignant Lymphoma (ML)

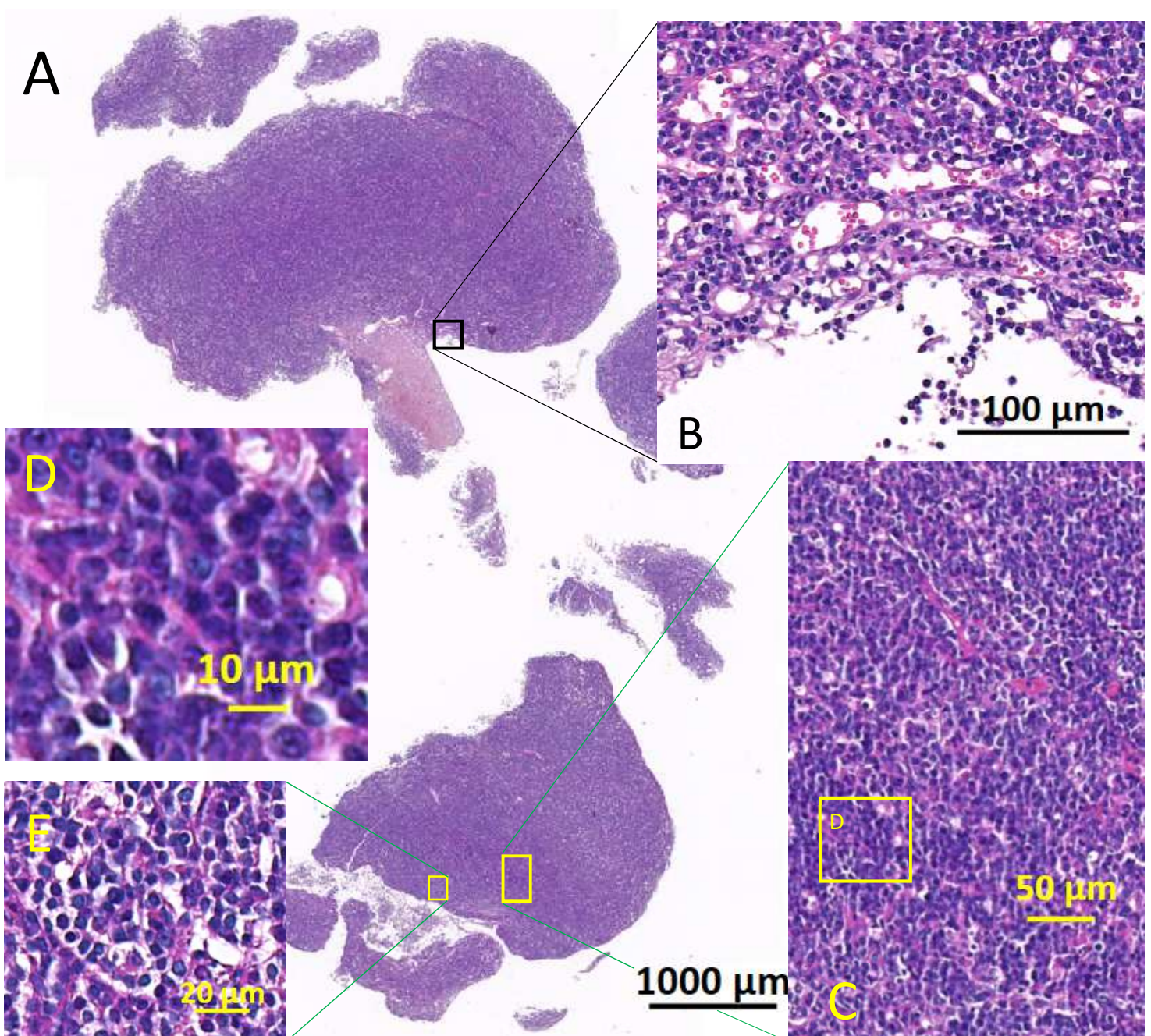
CBA/J ♀ derived tumor **JA-0018/ 0113-17**

Figure 14: Macroscopic aspect of **JA-0018** (case 18-14)



Malignant lymphoma with small lymphocytes – original localization studied: lung

Figure 15: Index neoplasm of sMDI JA-0018 (15-14) noted in the lungs of a ♀ CBA/J mouse



Legend of Figure 15 in previous page:

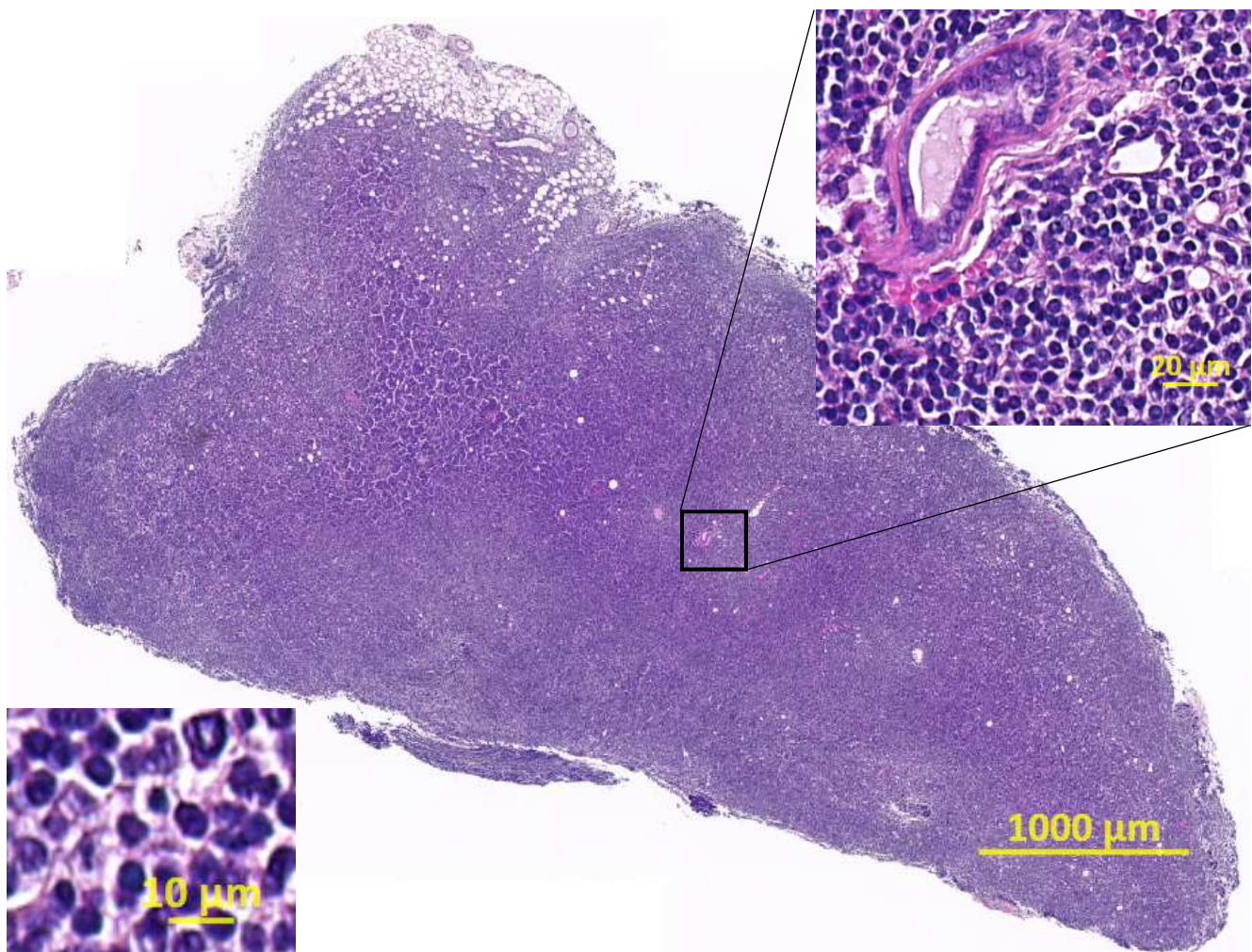
A: Low magnification fragments of the pulmonary neoplasm, exhibiting homogenous deeply basophilic sheets of neoplastic tissue that almost completely the pre-existing morphology of the lung and pleura.

B: This view adjacent to the pleura and mesothelial lining (**black arrow**) shows non-coalescing infiltration with small lymphocytes, with partial preservation of architecture.

C, D, E: medium (C) and high (D, E) magnifications of the neoplasm with small to medium-sized 5-8 μm lymphocytes with pseudo cord (packet) formation (white arrows) in preexisting pulmonary structures, notably pre-existing alveoli (E), mimicking a neuro-endocrine tumor.

Source file: TPL811_17_HE_11975_18_14_10_4_17_Lu

Figure 16: Low, medium and high magnification of 0113-17 malignant lymphoma (ML) derived from index case 0018-14 tumor, subcutis, adipose and mammary



CBA/J ♀: The proliferation is composed of homogenous sheets of small ($\sim 5 \mu\text{m}$ in diameter) to mid-sized ($\sim 5-8 \mu\text{m}$) well differentiated lymphocytes, which are diffusely invading into the subcutis, isolating small ducts and ductules of the mammary gland (see exocrine gland profile of upper right inset). Immunophenotyping would be desirable if this sMDI would be further used as a tumor model.

Source file: TPL811_17_HE_10445_Tu_0113_17.czi

JA-0034 sMDI: Malignant Lymphoma (ML)

In index case **JA-0034/0034-14 index case** with **1426-17 0036-17** and **0042-17** as examples of subsequent tumors are all phenotypically stable lymphoma. These lymphoma cells also are characterized by small cell morphology

no *in situ* Foto

Figure 17: Macroscopic aspect of **JA-0034**

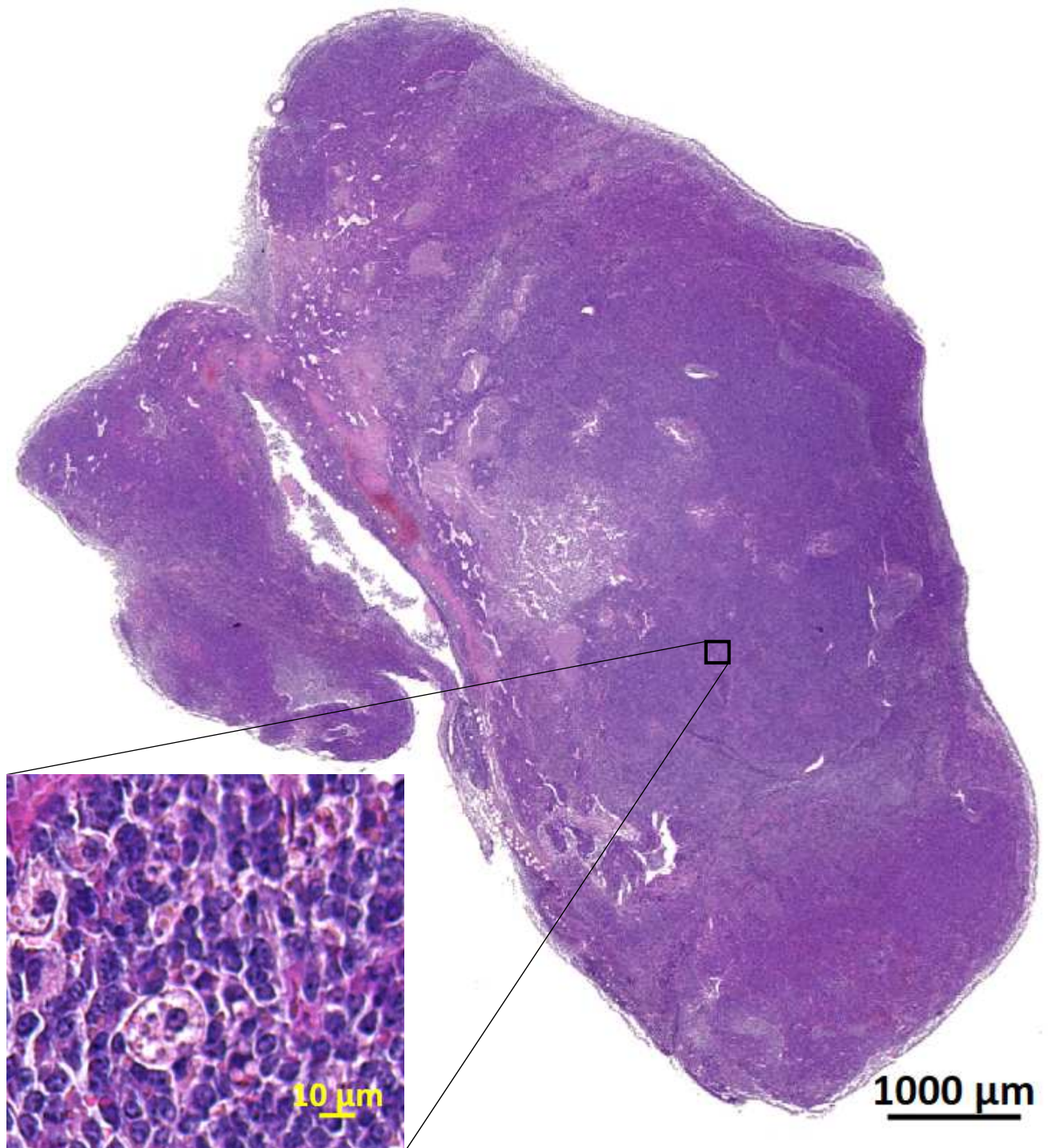
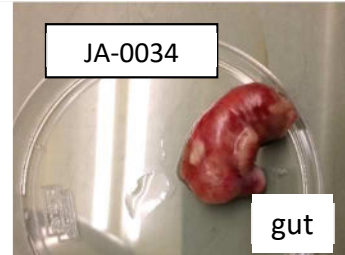


Figure 18: Low and high magnification of the malignant lymphoma (ML) index 0034-14

In previous page: The proliferation is composed of homogenous sheets of small ($\sim 5 \mu\text{m}$ in diameter) to mid-sized ($\sim 7 \mu\text{m}$) well differentiated lymphocytes, which are diffusely invading into the subcutis or a pre-existing lymph node. **Inset:** cells are $7-8 \mu\text{m}$ and there are also evidence of macrophages with phagocytized apoptotic debris (“starry sky” aspect)..

Morphological diagnosis: Malignant lymphoma, small cells, intestine

Source files:

2019-01-24 12_09_36-#10445darm_34-14_34-14.czi - ZEN 2.3 lite.png

2019-01-24 12_12_07-#10445darm_34-14_34-14.czi - ZEN 2.3 lite.png

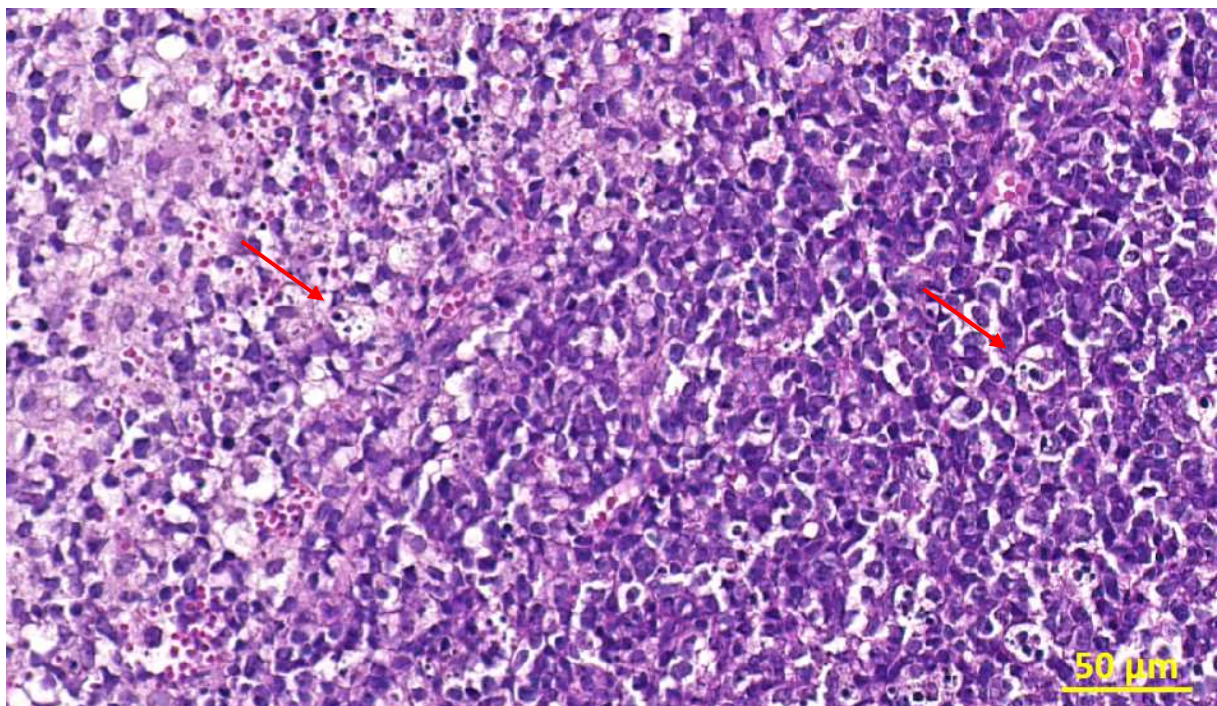


Figure 19: Medium magnification of the daughter malignant lymphoma case 1426-17

This specimen is in the subcutis adipose tissue, with diffuse invasion. The lymphoma cells are small/medium sized, measuring $7-8 \mu\text{m}$ and there is also as in index case macrophages with phagocytized apoptotic debris (“starry sky” aspect) – see **red arrows**.

The morphological similarity with the index case (see [Figure 18](#)) is striking.

Morphological diagnosis: Malignant lymphoma, small cells, intestine

Source file:

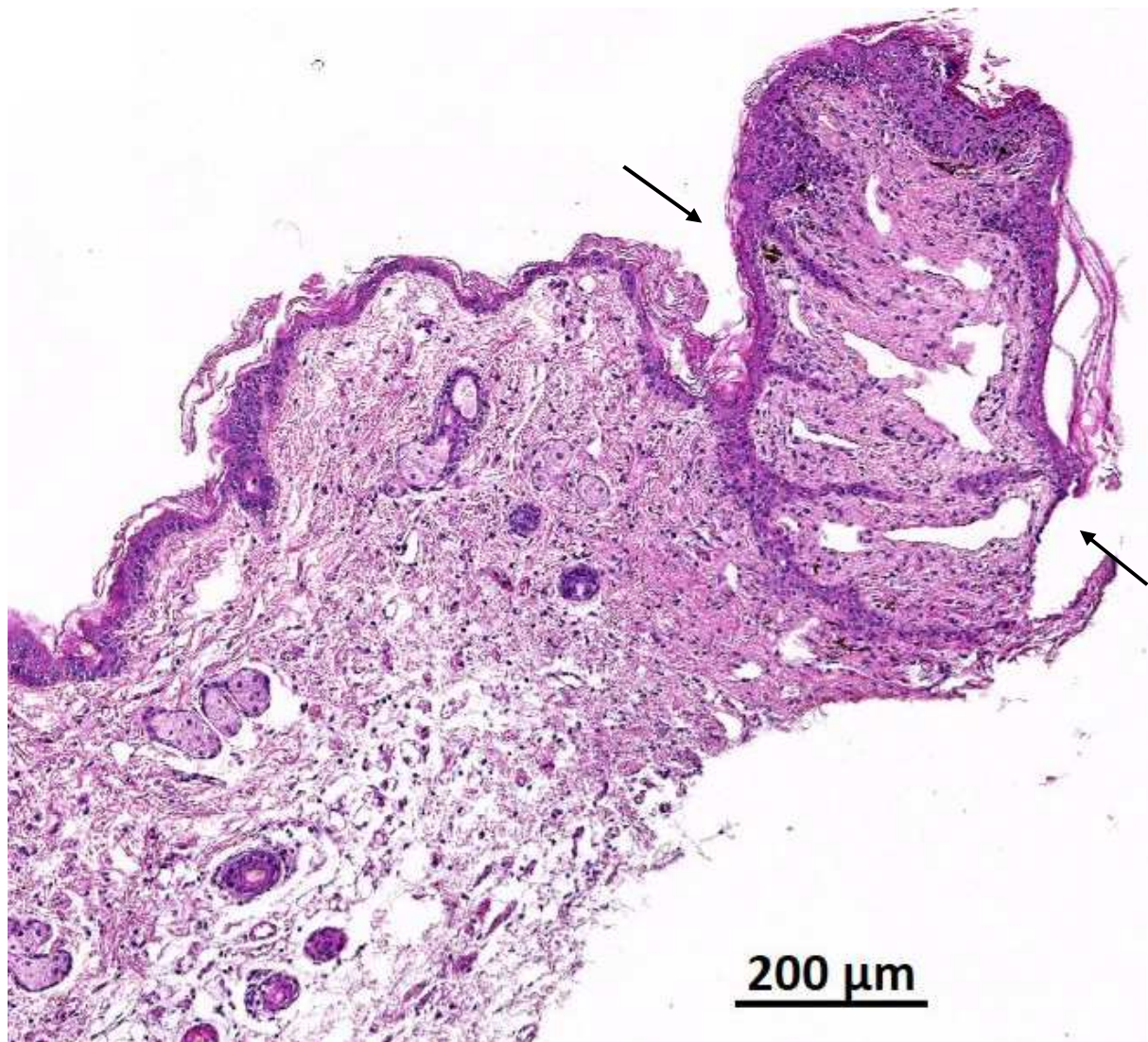
TPL Study Phase Number 780/17: 2019-01-25 12_33_53-#10445tu(da)_34-14_1426-17.czi - ZEN 2.3 lite.png

JA-0021 sMDI: Malignant Lymphoma (ML)

In the case of tumor **JA-0021** (Fig. 2), starting from various suspicious tissues, an enlarged lymph node from female C3H/HeJ mouse was re-transplanted. Although weakly growing in primary recipient SCID/bg mouse **1205-16**.

no *in situ* Foto

Figure 20: Spontaneous neoplasm study (study #10445): normal skin tissue with a mammary teat, female mouse 0021/14



Source: 2017-10-25 15_11_37-TPL811_17_HE_10445_1_mamma_021_14_recut-Rotate-03
- ZEN 2.3 lite

Index case: mouse ID number 0021-14, strain C3H/HeJ, sex: ♀.

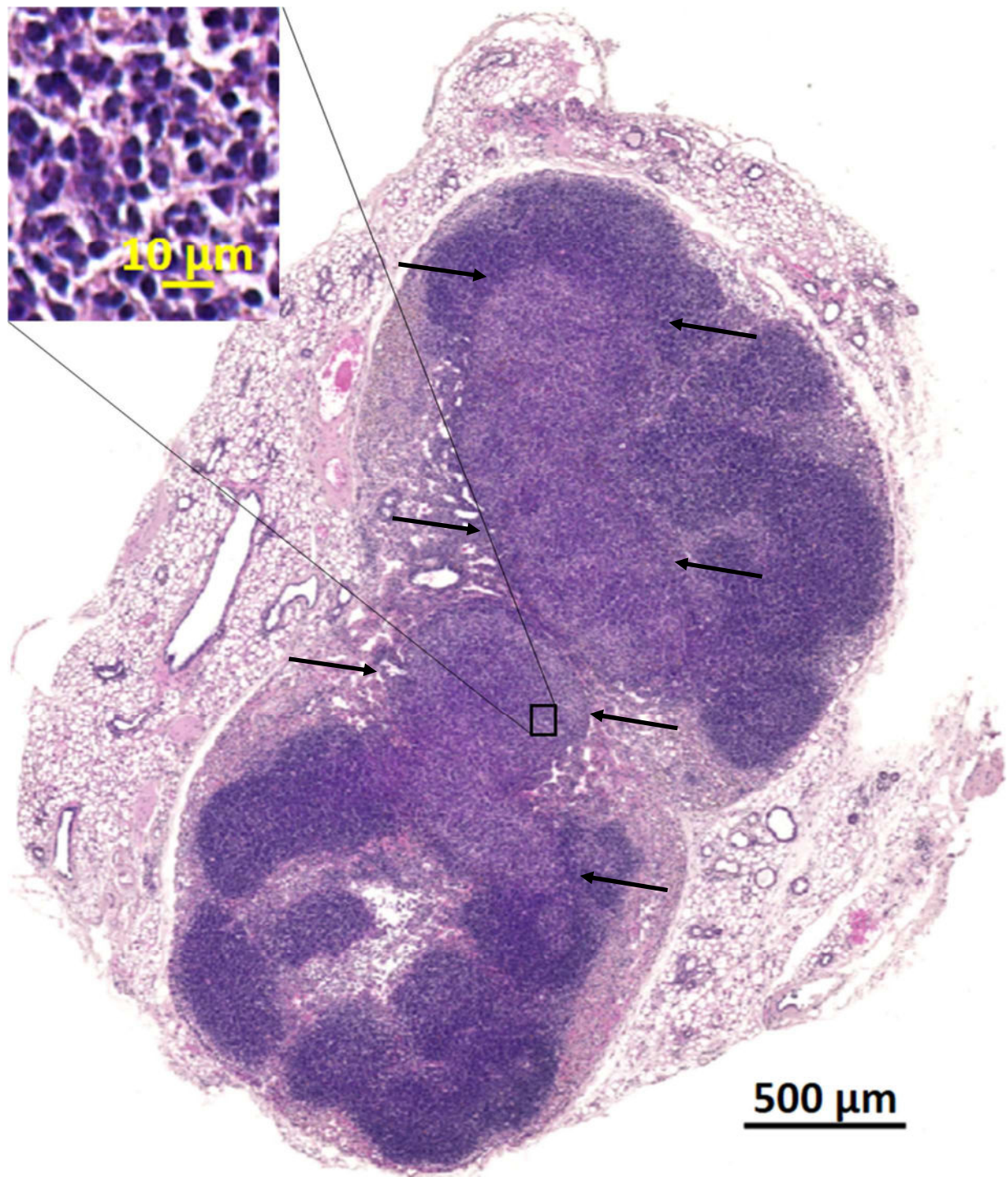
These are all normal tissues: there is no evidence of tumors, even after several recuts.

The source neoplasm was not located in this sample.

Morphological diagnosis: Within normal limits (normal skin and teat – see **black arrows**).

Abbreviation: NA (not applicable); ID = identification

Figure 21: Early malignant lymphoma localization in a lymph node – Index 0021-14

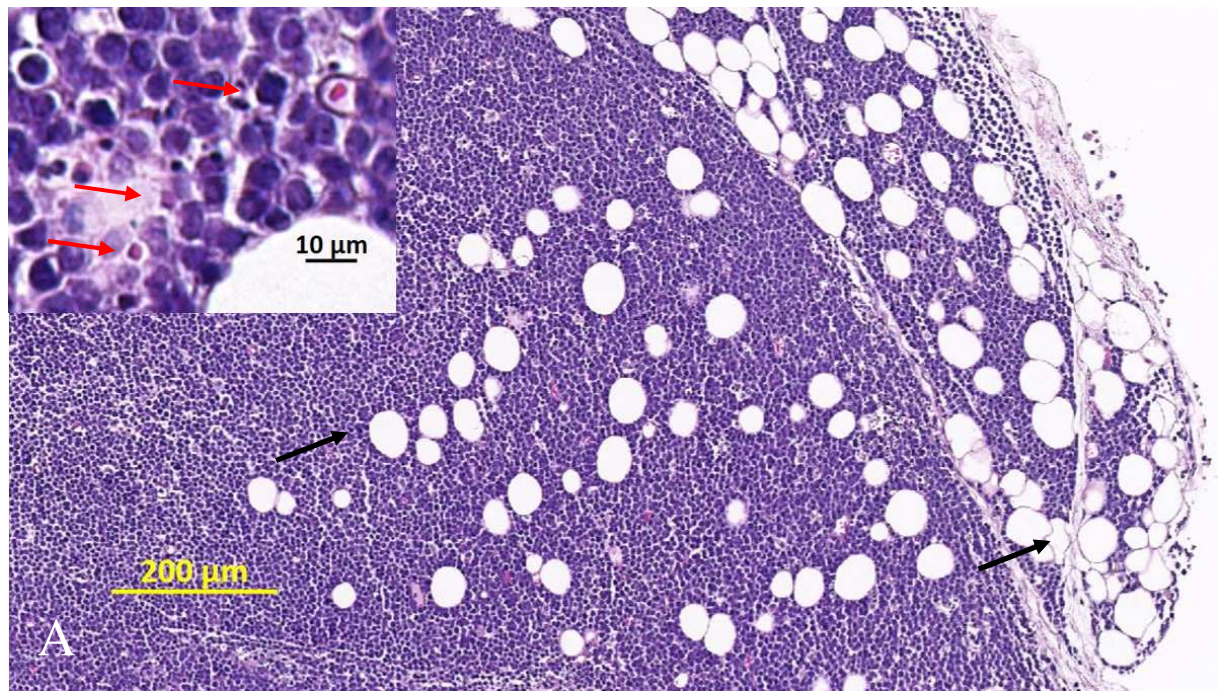


The para-cortical region of this sub-cutaneous lymph node has an early invasion with homogenous sheets of small lymphocytes (see **black arrows** to bracket the foci). Although an atypical lymphocytic immune response cannot be strictly rule out on an isolated case, the context suggests these early sheets of cells to represent malignant lymphoma. The surrounding tissue is mammary gland tissue in adipose tissue of subcutis (panniculus). **Inset:** The lymphocytes are small and homogenous in morphology, measuring 5-7 μm in diameter.

Source file: C:\Users\TLEMARCHAND\Documents\ProQinase-Paper-Project\neue-bilds\2019-01-25 11_09_23-TPL811_HE_10445-1_21-14.czi - ZEN 2.3 lite.png

Morphological diagnosis: Malignant lymphoma, panniculus/sub-cutis, early invasion

Figure 22: Spontaneous neoplasms (study #10445): malignant lymphoma, female SCID *bg/bg* mouse 1571/16



Source: 2017-10-25 14_51_40-TPL811_17_HE_10445_Tu_1571_16.czi - ZEN 2.3 lite

2018-01-22 18_25_10-TPL811_17_HE_10445_Tu_1571_16.czi - ZEN 2.3 lite

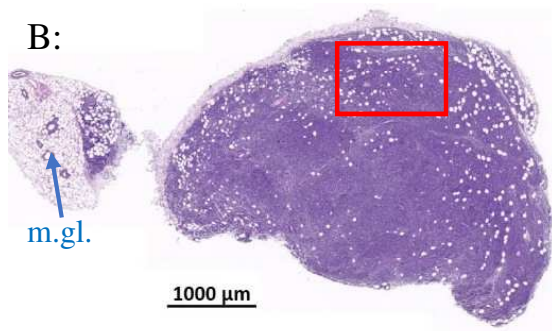
Index case: mouse ID number 0021-14, strain C3H/HeJ, sex: ♀.

Figure 22 A legend:

There is partial to complete erasing of the normal lymphoid architecture of a lymphoid organ by homogenous sheets of small (5 to 7 μm) round cells (see inset for details), most compatible with blastic lymphocytes, which invade the adjacent tissues, here most probably the adipose tissue of the subcutis and/or the skin (**black arrows** and **blue arrow** below in **B** showing mammary gland tissue). There is evidence of mitoses and apoptosis (inset of **A**: **red arrows**). Further characterization of the lymphoma would be an advantage.

Morphological diagnosis: Malignant lymphoma, panniculus/sub-cutis, ♀ SCID *bg/bg*.

Figure 22 B: Low magnification of tumor aspect overview (thumbnail):



Source photo file (B): 2018-01-22 18_20_25-TPL811_17_HE_10445_Tu_1571_16.czi - ZEN 2.3 lite

The **red rectangle** indicates the part of the neoplasm, which is depicted above

Blue arrow, m.gl. = mammary gland

Comments on Tumor lineage JA-0011 sMDI:

This case is a borderline one because 2 situations might have arisen:

1. The tumor lineage might have had indeed originated from cells present in this early invasion by small lymphocyte neoplastic cells noted in [Figure 21](#) above
2. this tumor might have spontaneously arisen from the immuno-suppressed beige mouse 1571/16 ([Figure 22](#)), and might not be derived from the index case 021-14.

IHC could be useful to further characterize the tumors and confirm lineage.

JA-0009 sMDI: Adenocarcinoma, anaplastic, invasive

Tissue of origin of tumor **JA-0009/ 1286-16**

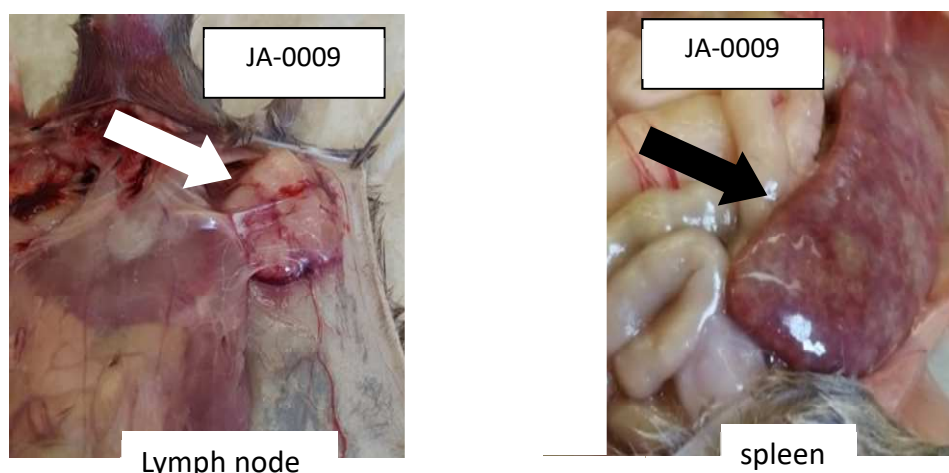


Figure 23: Macroscopic aspects of the index tumor **009-14** (index case for lineage JA-009)

The index animal had a subcutaneous mass in the lymph node region and a markedly enlarged spleen, suggesting a malignant lymphoma (see [Figure 23](#)). Histology showed the “lymph node” tumor to be a transmissible neoplasia of epithelial glandular origin ([Figure 27](#) and [Figure 24](#)) located in the skin/subcutis with possible anatomical localization in/adjacent to a lymph node or other organ (origin could be apocrine sweat gland, mammary gland etc.). It was an aggressive neoplasm with abundant epidermoid ([Figure 25](#) – actually predominant feature of the daughter transmitted neoplasm 1286/16 see [Figure 28](#) and [Figure 29](#)) and spindle cell differentiation ([Figure 26](#)). As the spleen was not sampled for microscopic evaluation, the presence of metastases of the epithelial neoplasm (carcinoma) could not be verified, and therefore a concomitant neoplasm of the hemolymphopoietic lineage (leukemia or lymphoma) cannot be strictly ruled out in this particular case.

Histological classification: Skin, subcutis, epithelial neoplasia, glandular (tubular), epidermoid and spindle shape cell differentiation

Diagnosis: Adenocarcinoma, solid, invasive, NOS

Main features: Solid (trabecular), invasive, anaplastic

Mitotic index: 3,25 mitoses per high power fields (phpf) for index case 009-14 and 3.125 mitoses phpf for the derived tumor 1286/16.

Necrosis: Yes (coagulative, disintegrative, with neutrophils), SCN (pyknosis, karyorrhexis), compatible with presence of apoptosis - Overall necrosis grade : minimal

Main differential diagnosis: epidermoid carcinoma, carcinosarcoma (malignant glandular mixed cell tumour), anaplastic carcinoma

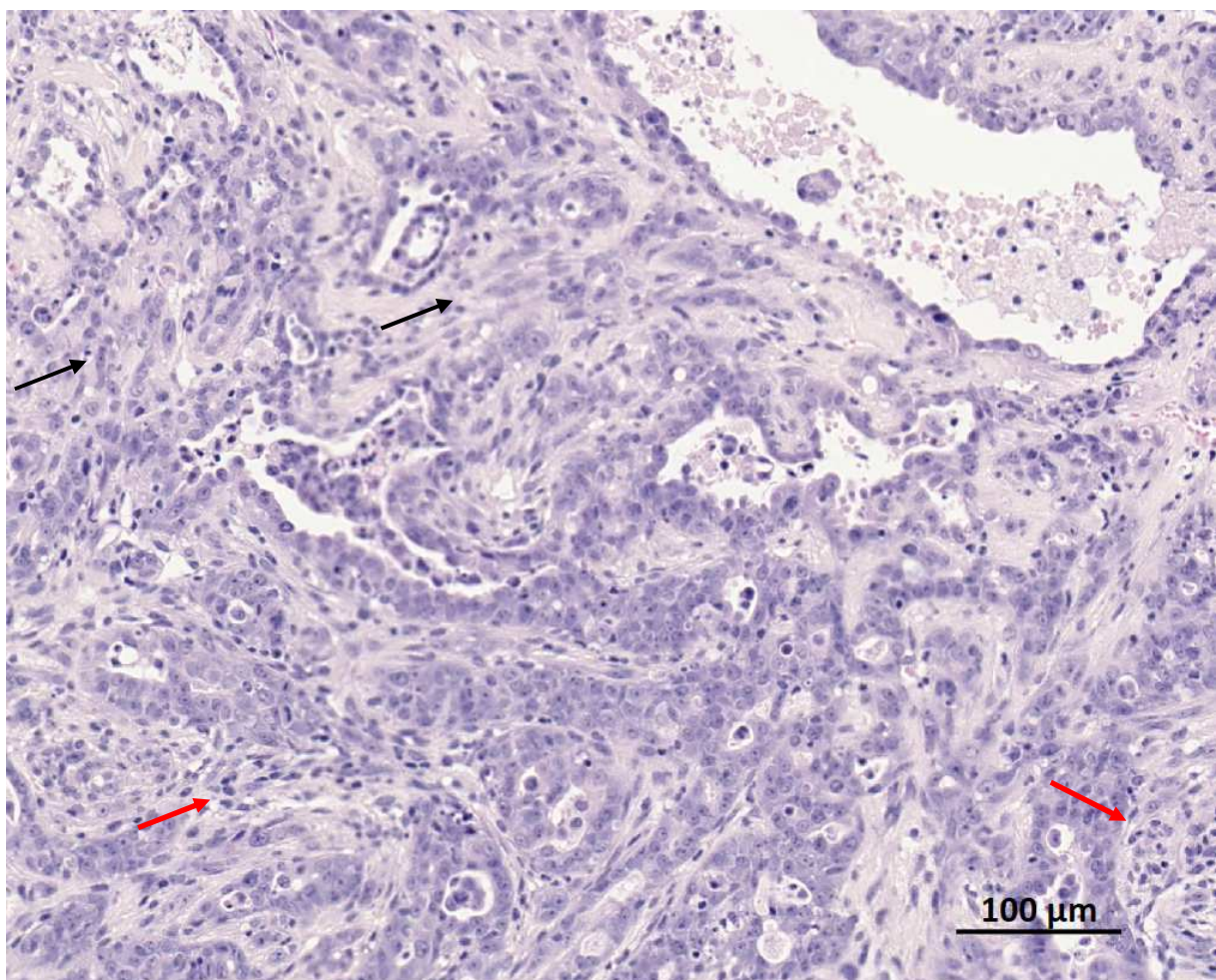


Figure 24: Medium high magnification of the tumor index case 009-14, with glandular and anaplastic/ spindle shaped differentiation

Medium high magnification of the tumor index 009-14, showing evidence of glandular differentiation, with areas of anaplastic/spindle shaped differentiation (**black arrows**). Host inflammatory cells are moderately numerous (**red arrows**).

Source file: 2019-01-23 16_25_06-TPL_601_16_009_14_Tu.czi - ZEN 2.3 lite.png

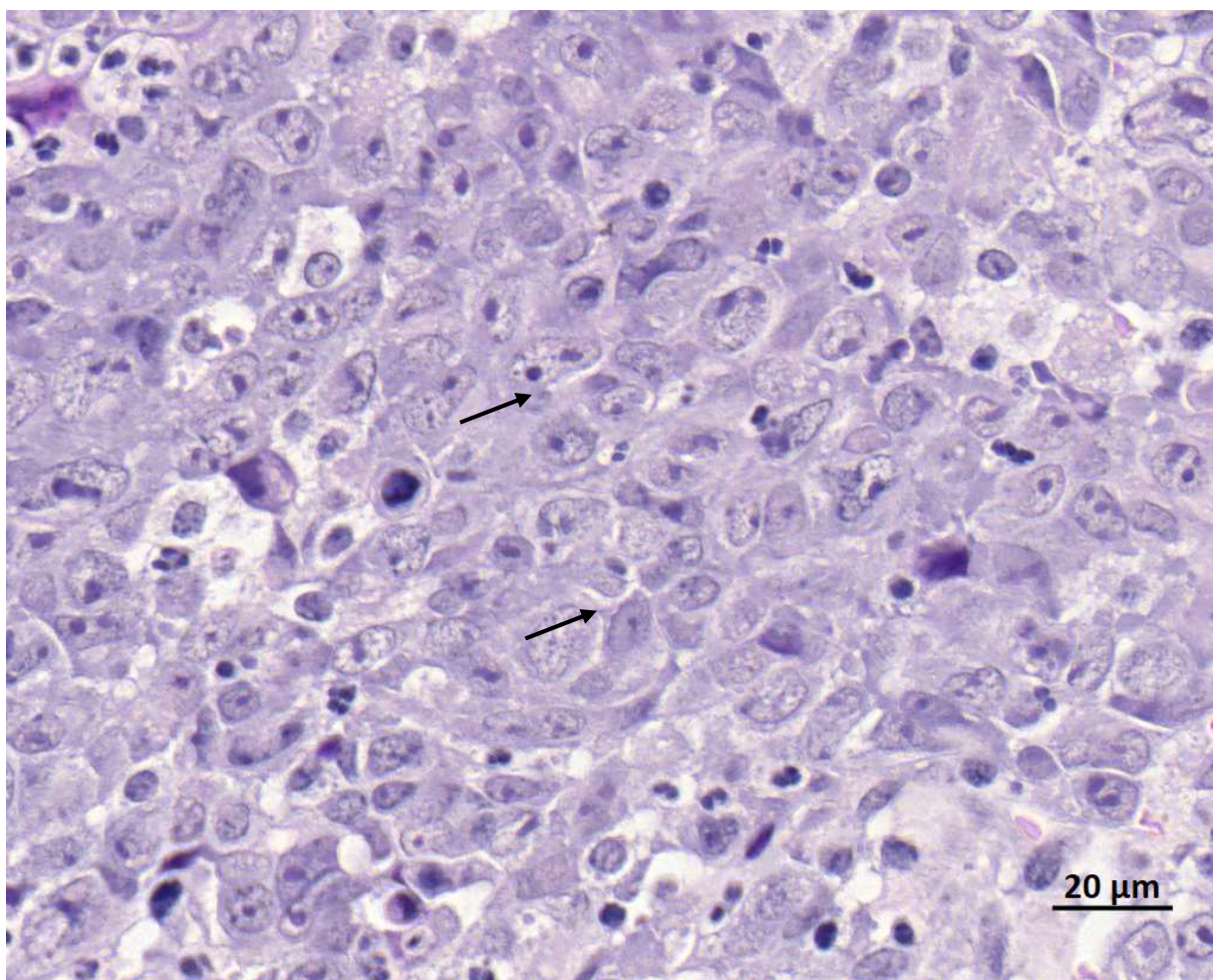


Figure 25: High magnification of the tumor index case 009-14, with clear evidence of epidermoid differentiation, suggesting an epidermoid carcinoma

The intercellular bridges are diffusely very distinct in this thin section of the tumor (**black arrows**).

Source file: 2019-01-24 21_34_29-TPL_601_16_009_14_Tu.czi - ZEN 2.3 lite.png

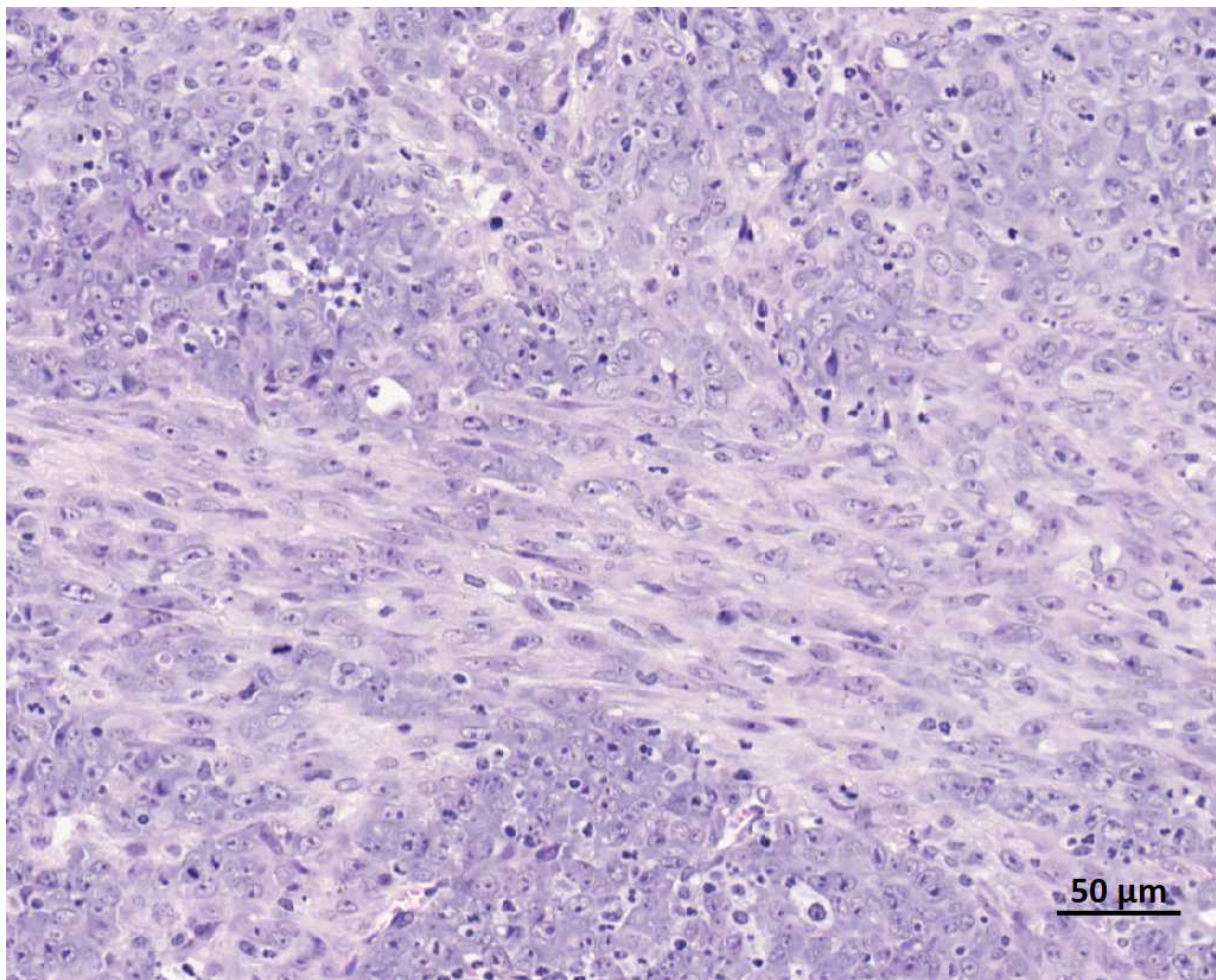


Figure 26: A moderate high magnification view of 009-14 showing spindle shaped cell differentiation

The epithelial to mesenchymal transition and the epidermoid differentiation, with a clear anaplastic (isolated neoplastic cells) and spindle-shaped neoplastic cells (suggesting a malignant mixed cell tumor of glandular origin or carcinosarcoma) suggest the neoplasm to be of salivary or apocrine sweat gland or also possibly of mammary gland origin.

Source file: 2019-01-24 22_11_08-TPL_601_16_009_14_Tu.czi - ZEN 2.3 lite.png

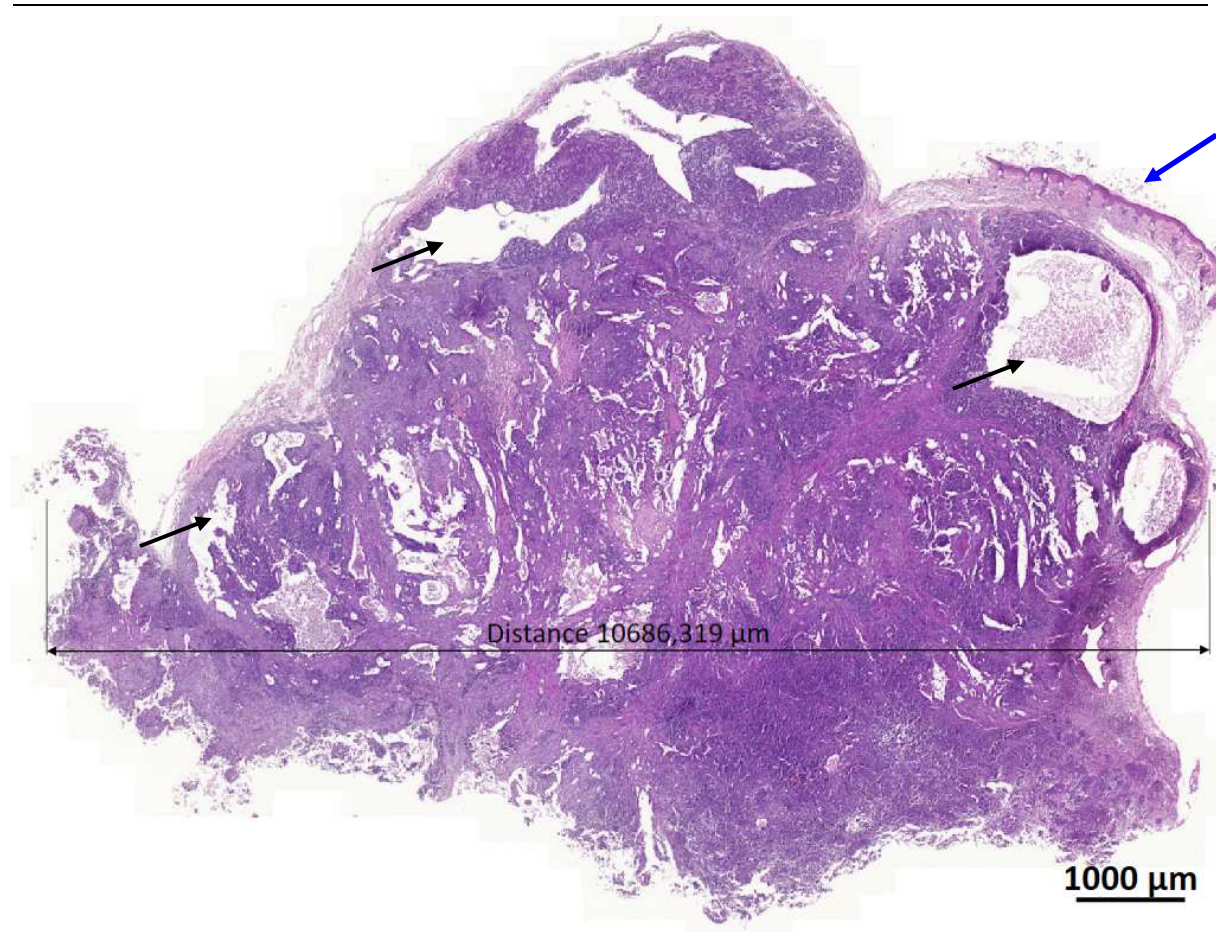


Figure 27: Low magnification view of the index neoplasia 009-14

There is presence of cysts with papillary proliferations and many tubular profiles, with abundant evidence of secretion materials and necrotic debris, demonstrating the glandular origin of this aggressive neoplasm (**black arrows**). The tumor is clearly cutaneous/sub-cutaneous (**blue arrow**).

Source file: 2019-01-24 22_20_14-009_14.czi - ZEN 2.3 lite.png

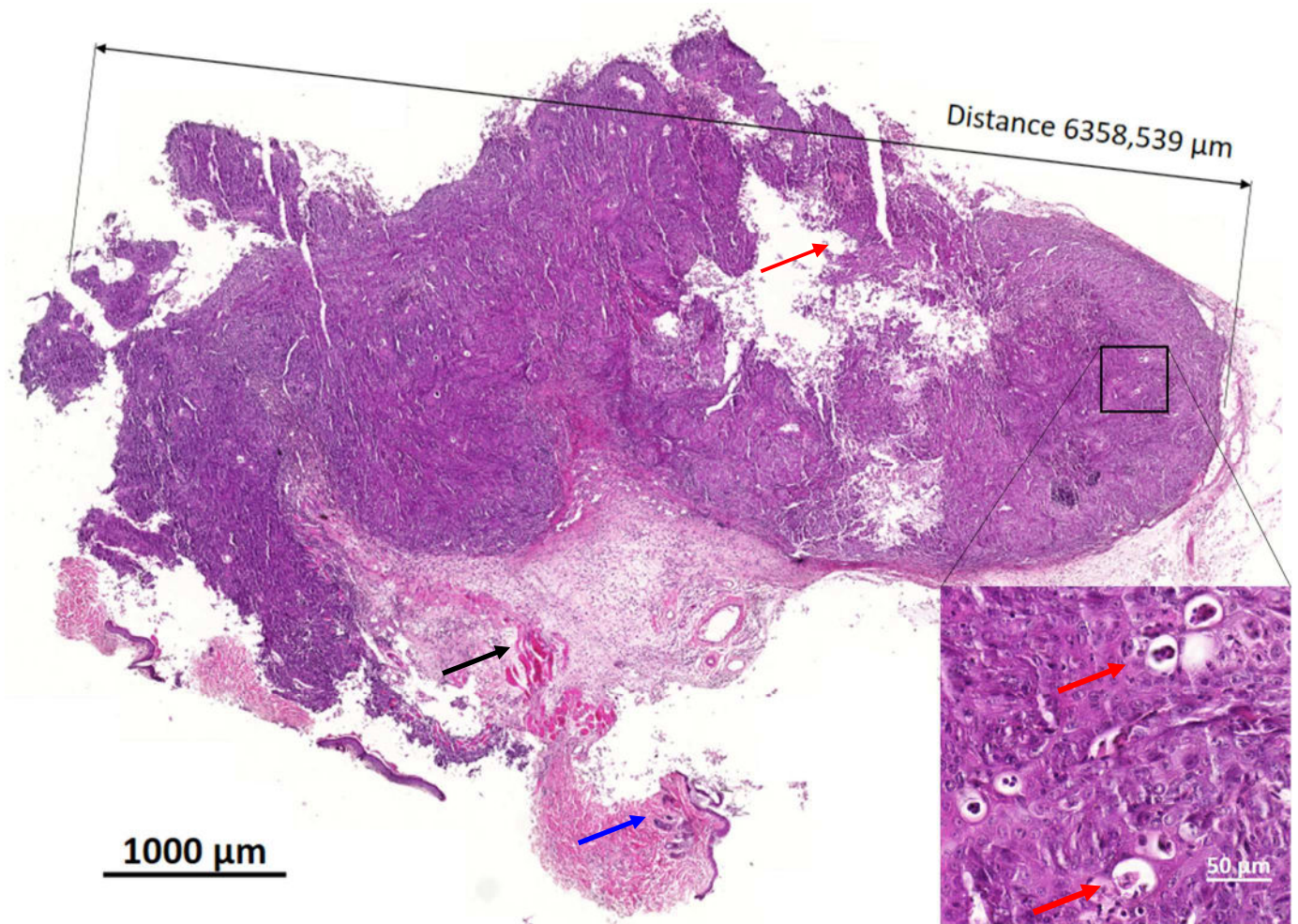


Figure 28: Low magnification aspect of the transmitted tumor 1286/16 from index case 09-14

Low magnification aspect of the transmitted tumor 1286/16: essentially solid aspect with still limited evidence of mucinous and/or glandular differentiation (inset: **red arrows**). The solid epidermoid carcinoma component is now predominant, almost exclusive, with more eosinophilia associated with keratinization. The tumor is also developed in the subcutis adjacent to cutaneous muscle (**black arrow**) and right under the skin (**blue arrow**).

Source files:

2019-01-24 23_10_30-1286_16.czi - ZEN 2.3 lite.png

2019-01-24 22_57_44-1286_16.czi - ZEN 2.3 lite.png

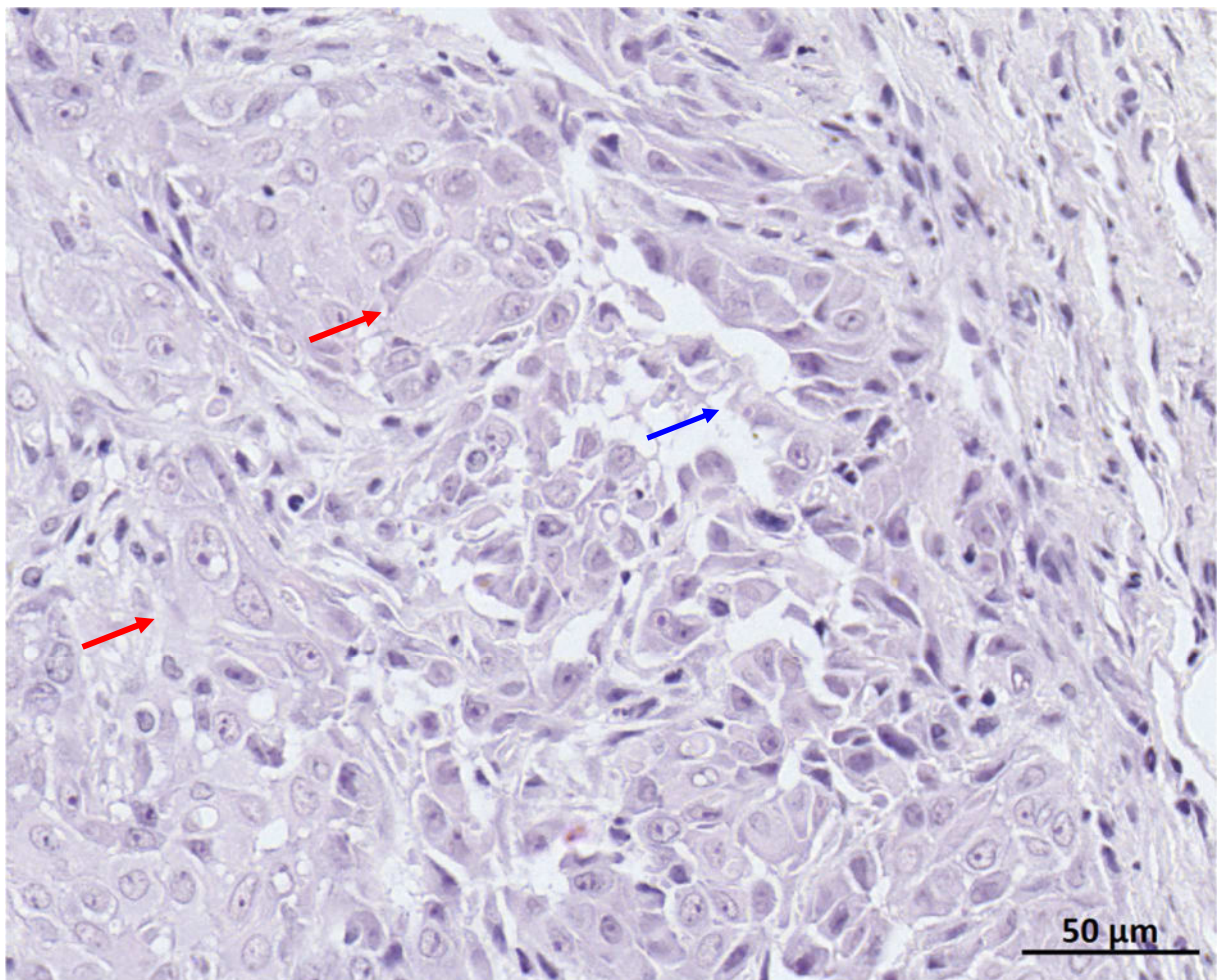


Figure 29: High magnification aspect of the transmitted tumor 1286/16

High magnification aspect of the 1286/16 with epidermoid differentiation and abundant pale eosinophilic cytoplasm (**red arrows**) and acantholysis with pseudo-glandular formation (**blue arrow**). The epidermoid differentiation is in this case the main component and therefore a differential diagnosis is **epidermoid carcinoma**

Source file: 2019-01-24 22_08_31-TPL_601_16_009_14_Tu_1286.czi - ZEN 2.3 lite.png

JA-0017 sMDI: Adenocarcinoma, complex type

Index case **JA-0017/ 0096-17** seemed at first analysis to exhibit some significant degree of phenotypic drifting. Tumors from the two daughter mice (1234-16 and 0096-17)

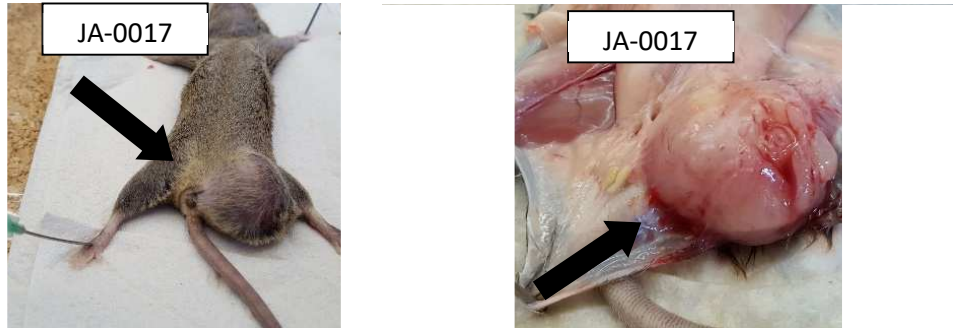


Figure 30 : Gross aspects of the index neoplasm 0017-14

Adenocarcinoma, complex type, or "mixed cell tumor",

The proliferation is composed of both myoepithelial and glandular elements with preserved ductular elements. These elements are well differentiated and benign looking.

This is an epithelial proliferation from an exocrine gland, of undetermined origin. The complex nature (see below) suggests it to be most likely of apocrine sweat gland or mammary gland origin.

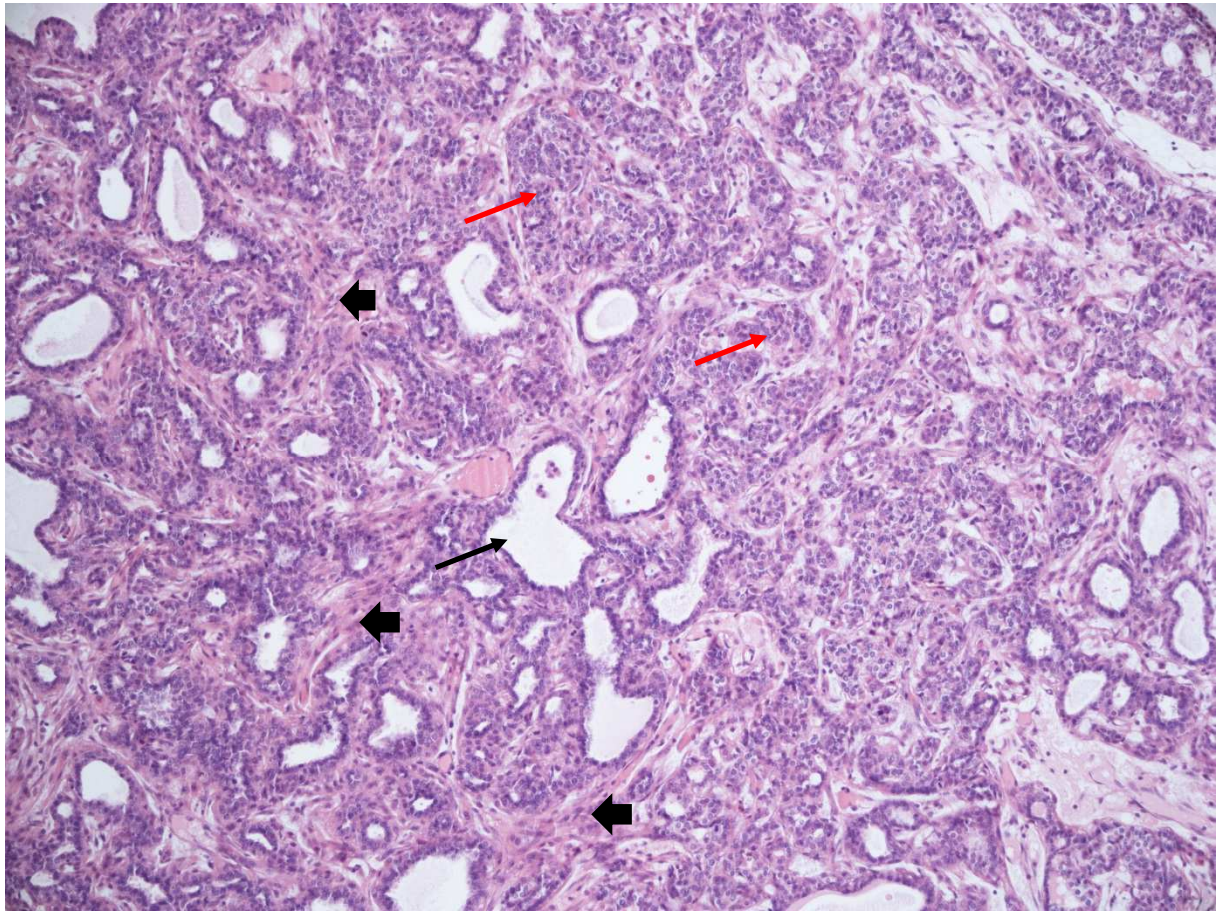



Figure 31: Complex adenocarcinoma (mixed tumor) -index-case, HE stain, original magnification: 100x

Index case: mouse ID number 017-14. Strain CBA/J ♀

This is an epithelial proliferation from an exocrine gland, of undetermined origin. The complex nature (see below) suggests it to be most likely of apocrine sweat gland or mammary gland origin.

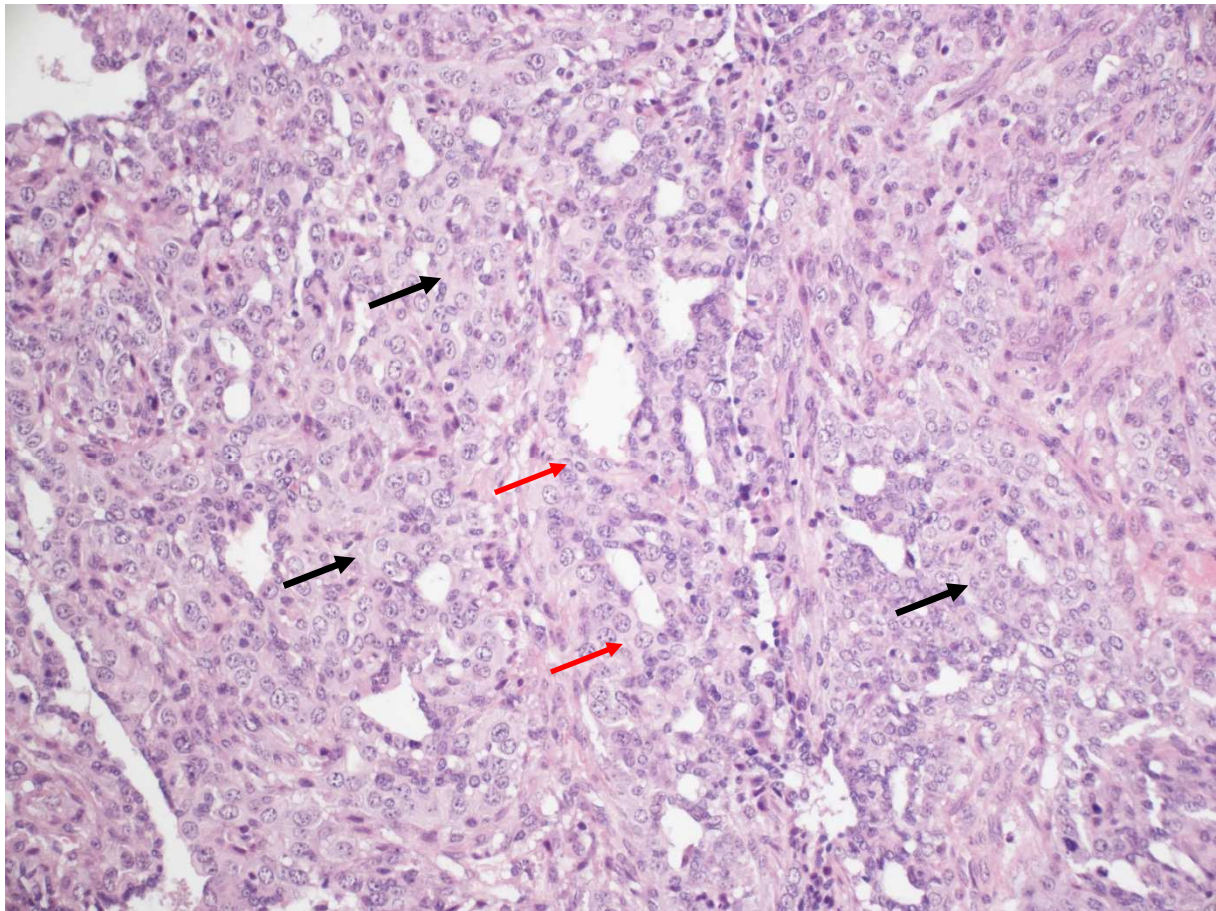
The proliferation is composed of both myoepithelial (**arrowheads** ) and glandular elements (**red arrows**) with preserved ductular elements (**black arrow**). These elements are well differentiated and benign looking. This neoplasm was however transmitted.

Morphological diagnosis: Complex adenocarcinoma/Mixed Tumor/Carcinosarcoma.

Abbreviation: c-ADK/MT/KS

Image ID: 780_#10445_tu01_0017-14_0017-14_HE_10x_1-AdK--mixed tumor-index-case, HE stain, original magnification: 100x

Figure 32: Complex adenocarcinoma (mixed tumor) – myoepithelial aspect, derived case mouse 1234-16, HE stain, original magnification: 200x



Mouse ID #1234-16; from index case: mouse ID number 017-14. Strain CBA/J ♀.

The proliferative component of this tumor is mostly myoepithelial (**black arrows**) with well differentiated glandular elements (**red arrows**).

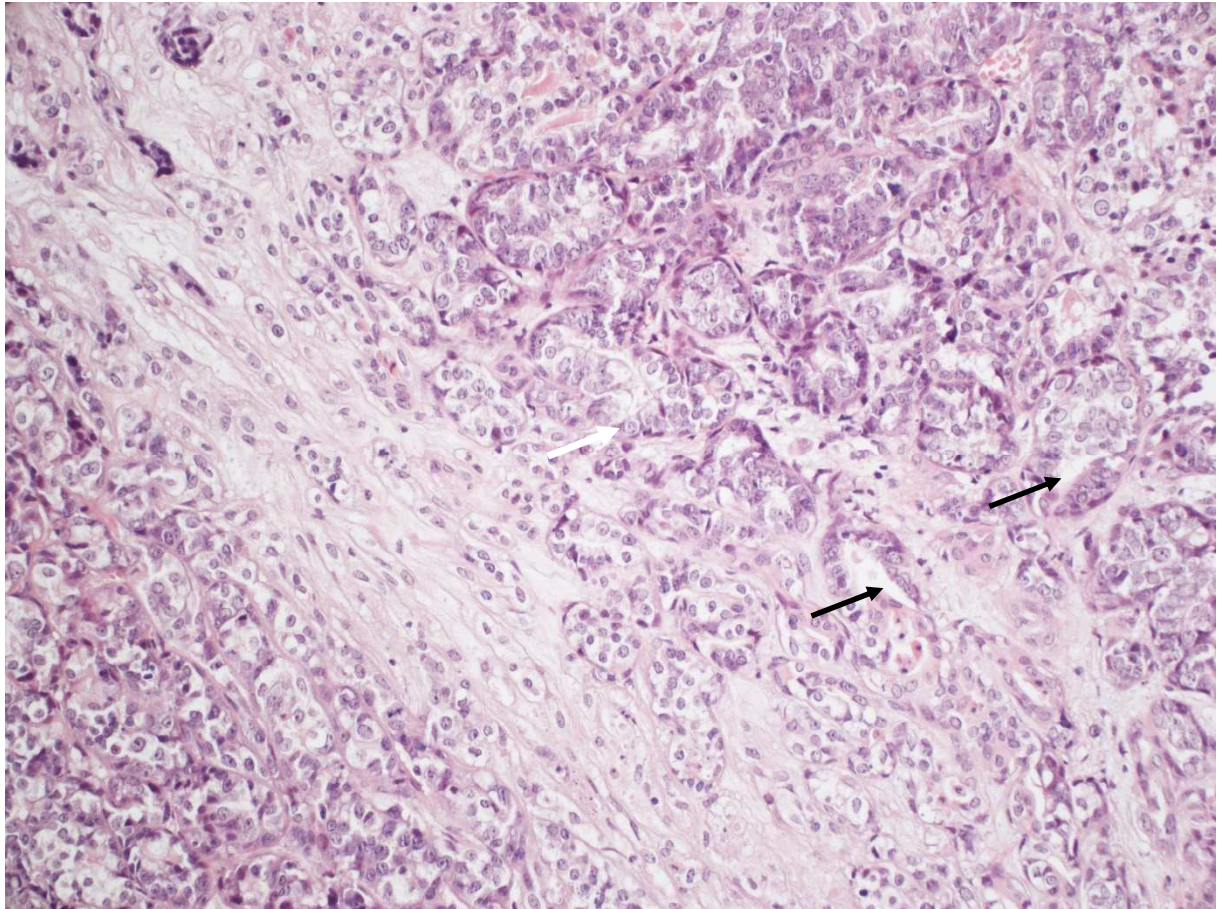
Morphological diagnosis: Complex adenocarcinoma/Mixed Tumor/Carcinosarcoma.

Abbreviation: c-ADK/MT/KS

Image ID: 780_#10445_tu_0017-14_1234-16_HE_20x_2-AdK-wKeratinization-mixed tumor-complex-myoepith-epith2mesenchT-wC,

HE stain, original magnification: 200x

Figure 33: Complex adenocarcinoma (mixed tumor) – trabecular clear cell aspect, derived case mouse 0096-17, HE stain, original magnification: 200x



Mouse ID #0096-17; from index case: mouse ID number 017-14. Strain CBA/J ♀.

Trabecular carcinoma composed of epithelial cells with clear cytoplasm, with occasional luminal differentiation (**black arrows**).

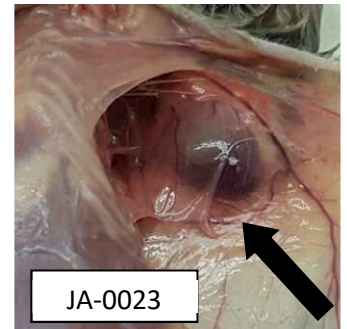
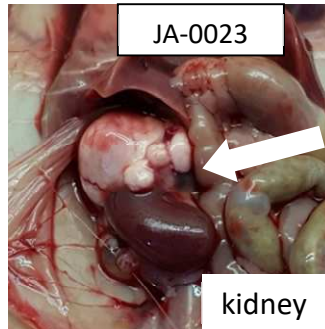
Morphological diagnosis: Trabecular carcinoma, possibly from the index complex adenocarcinoma/Mixed Tumor/Carcinosarcoma.

Abbreviation: c-ADK/MT/KS

Image ID: 780_#10445_tu01_0096-17_0017-14_HE_20x_2-AdK--mixed tumor- trab-K, HE stain, original magnification: 200x

JA-0023 sMDI: Adenocarcinoma, mammary gland

JA-0023 (Fig. 3) were obtained by growing spontaneous tumors either from a primary invasive ADK of mammary gland origin (back tumor – see [Figure 36](#)) or a clear cell carcinoma (CCC)-like tumors from the kidney of the single index mouse 0023-14 ([Figure 34](#) and [Figure 35](#)). Morphologically, all mouse derived (sMDI) tumors, including a derived (daughter) tumor noted in the kidney of another mouse, e.g. **0001-17** ([Figure 39](#)), had morphological features identical or the closest to the mammary index tumor of the back JA-0023 in 0023-14. These 2 index neoplasms and all daughter sMDI, e.g. **0001-17**, **0005-17**, **1620-16**, **0544-17** and **0547-17** (see below) are presented below.



Renal tumor: index case: Carcinoma/adenocarcinoma with clear cell differentiation /Clear Cell Renal Carcinoma – see [Figure 34](#) and [Figure 35](#).

Mammary gland: Invasive ductal cystic-papillary adenocarcinoma with desmoplasia and lymphatic emboli – see index [Figure 36](#) and lineate [Figure 37](#) to [Figure 42](#).

- peripheral perineoplastic lymphocytic infiltration, moderate
- hemorrhage and erythrophagocytosis by macrophages (not shown in photos below)

Given the aggressiveness of the primary tumor (i.e. neoplastic emboli) it is very likely the tumor origin of the tumor lineage s-MDI JA-.0023 is the mammary gland, and not the kidney.

The papillary cystic tumor of mammary gland origin has excellent phenotypic stability (see [Figure 37](#) to [Figure 42](#)).

Figure 34: Low (left) and mid (right) magnification views of the index tumor from the kidney

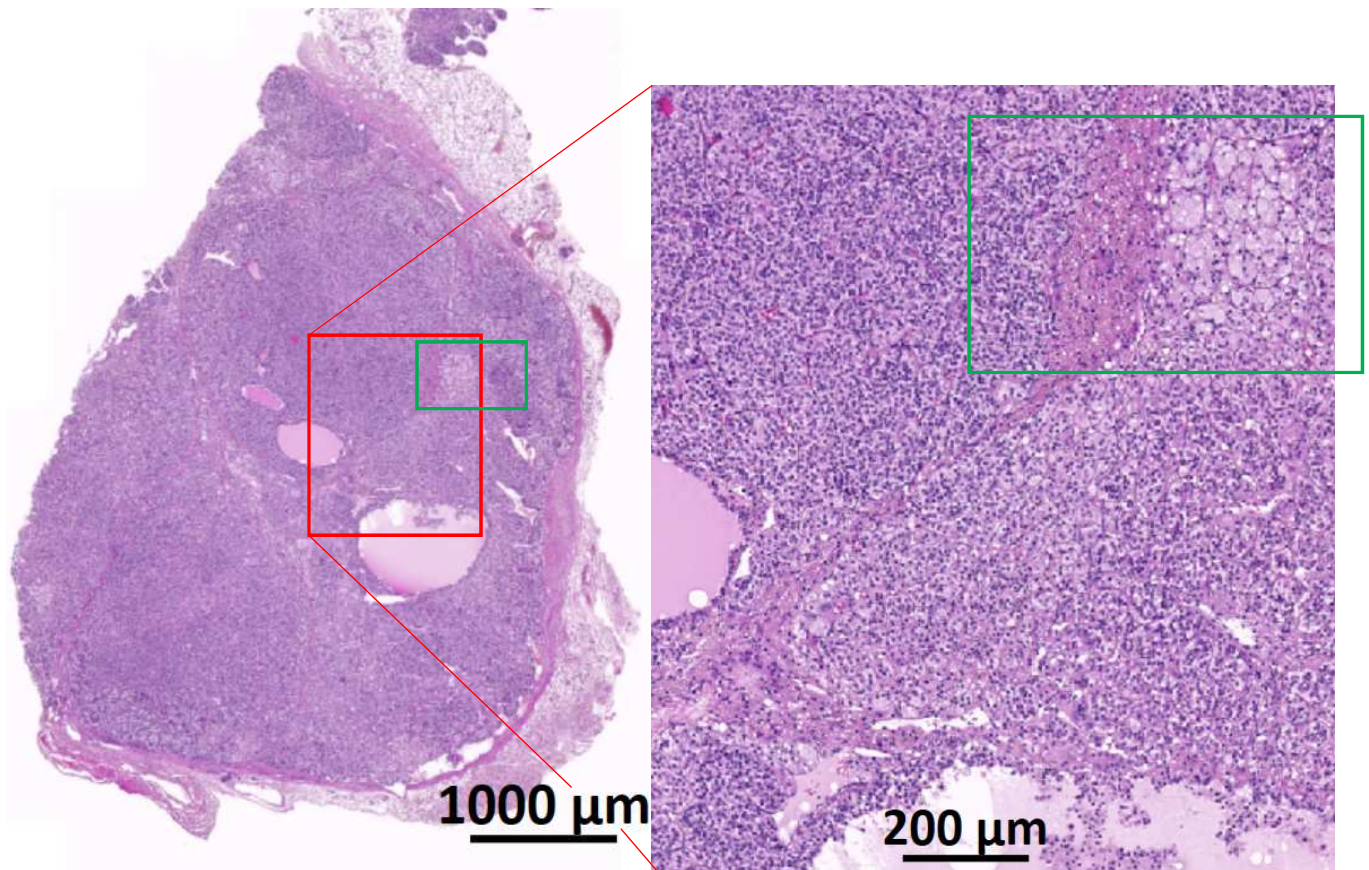
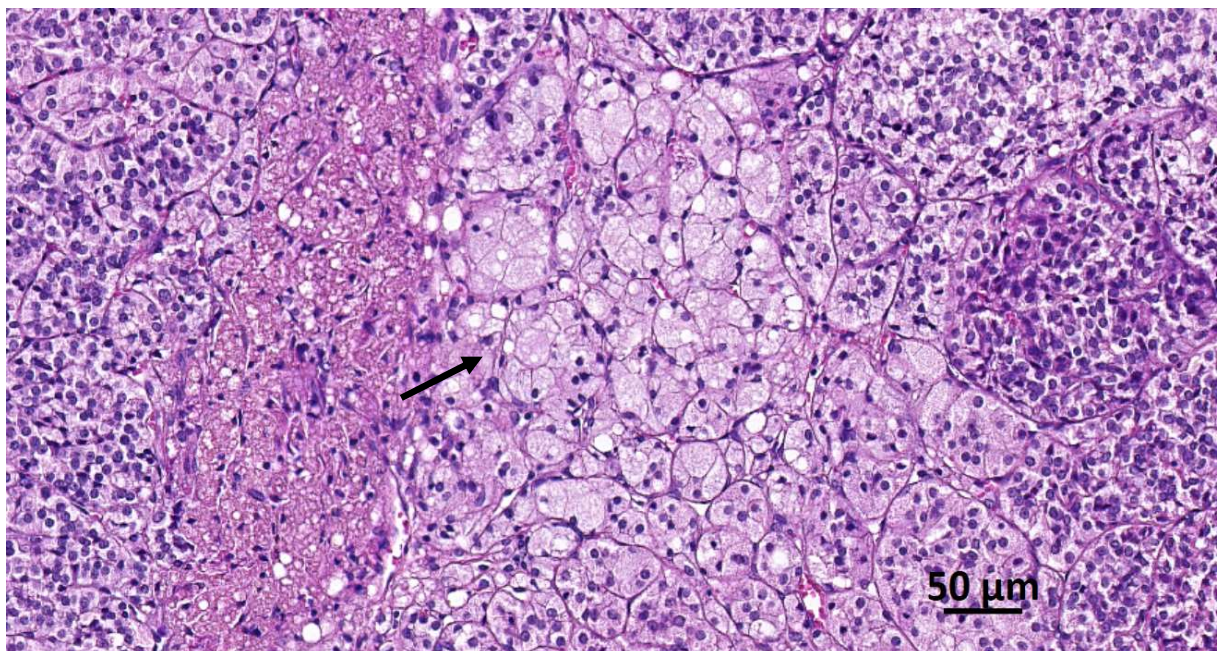
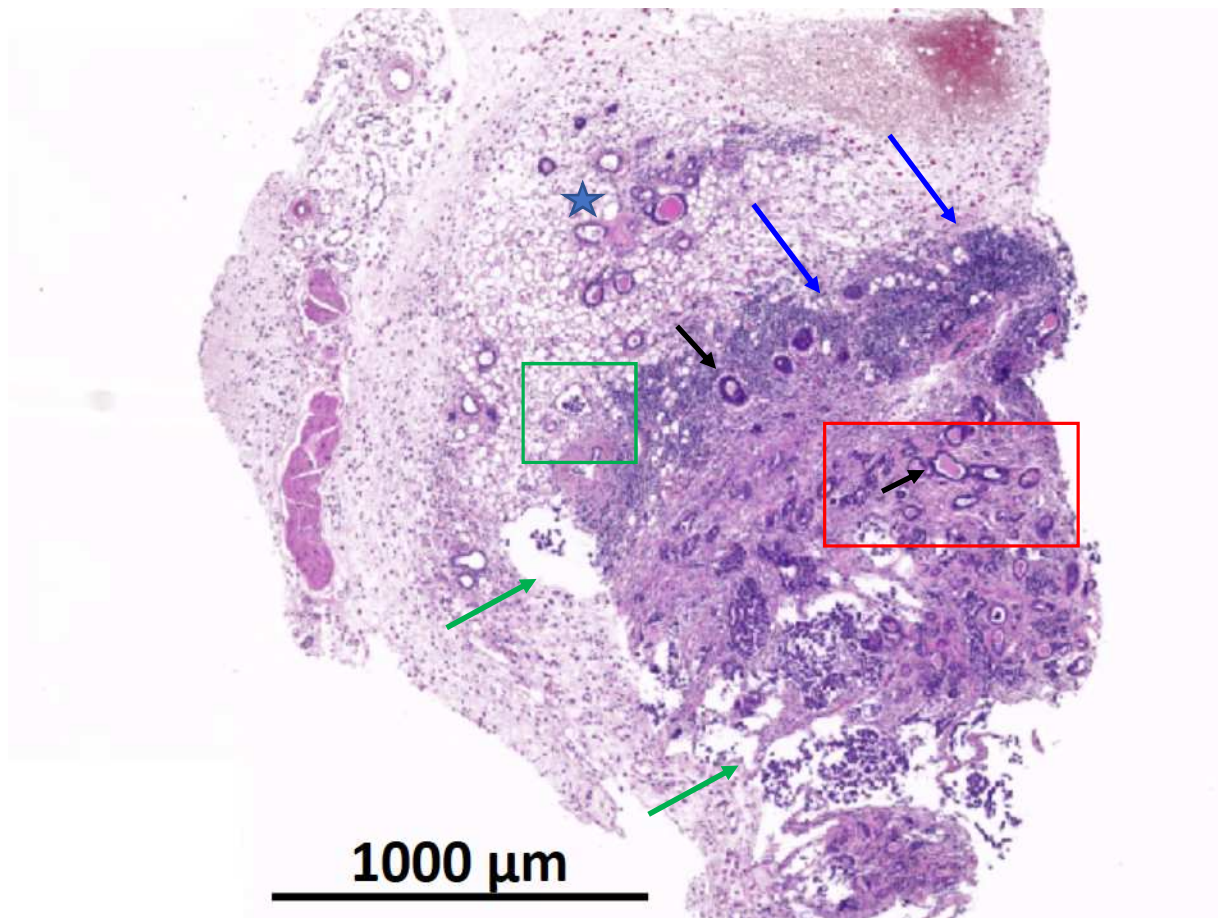


Figure 35: High magnification view of the index renal tumor

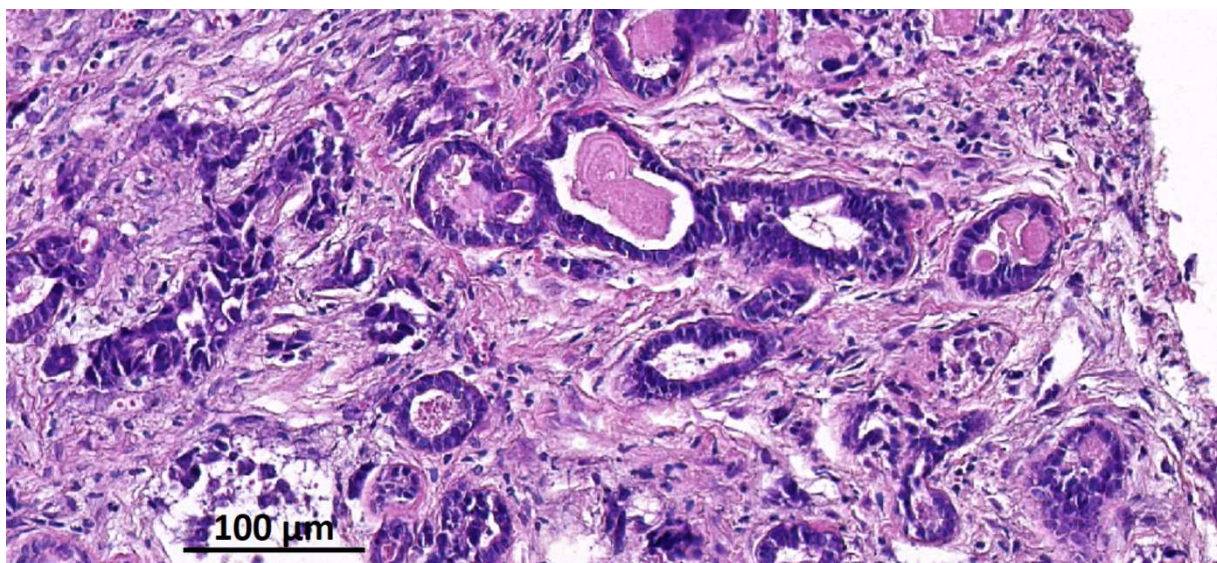


Green square inset: High magnification view of the clear cell differentiation in the index tumor (**black arrow**), which is focally reminiscent of a clear cell renal carcinoma, the most common renal neoplasm in humans. **Source file:** 2019-02-03 21_43_30-10445_tu_nie_0023-14_0023-14.czi - ZEN 2.3 lite.png

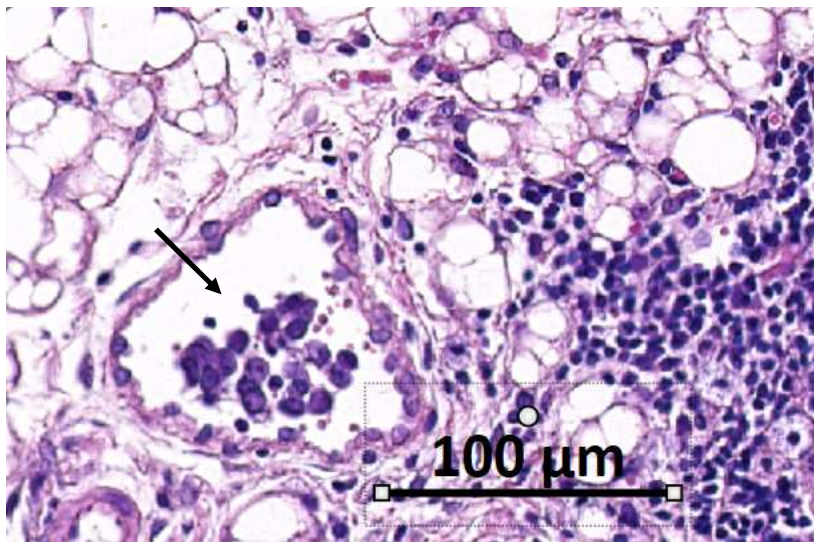
Figure 36: Index tumor of the subcutaneous tumor: microscopic morphological aspects



Low magnification aspect of the subcutaneous neoplasm: there is a mass developed from the mammary gland (★) and in the adipose tissue, of malignant glandular ductular profiles with varying glandular secretion (**black arrows**), invading into the adjacent subcutis and eliciting an abundant fibroplasia (desmoplastic change) and abundant lymphoid response (**blue arrow**) and dilated lymphatics and blood vessels (**green arrows** and **green square**).

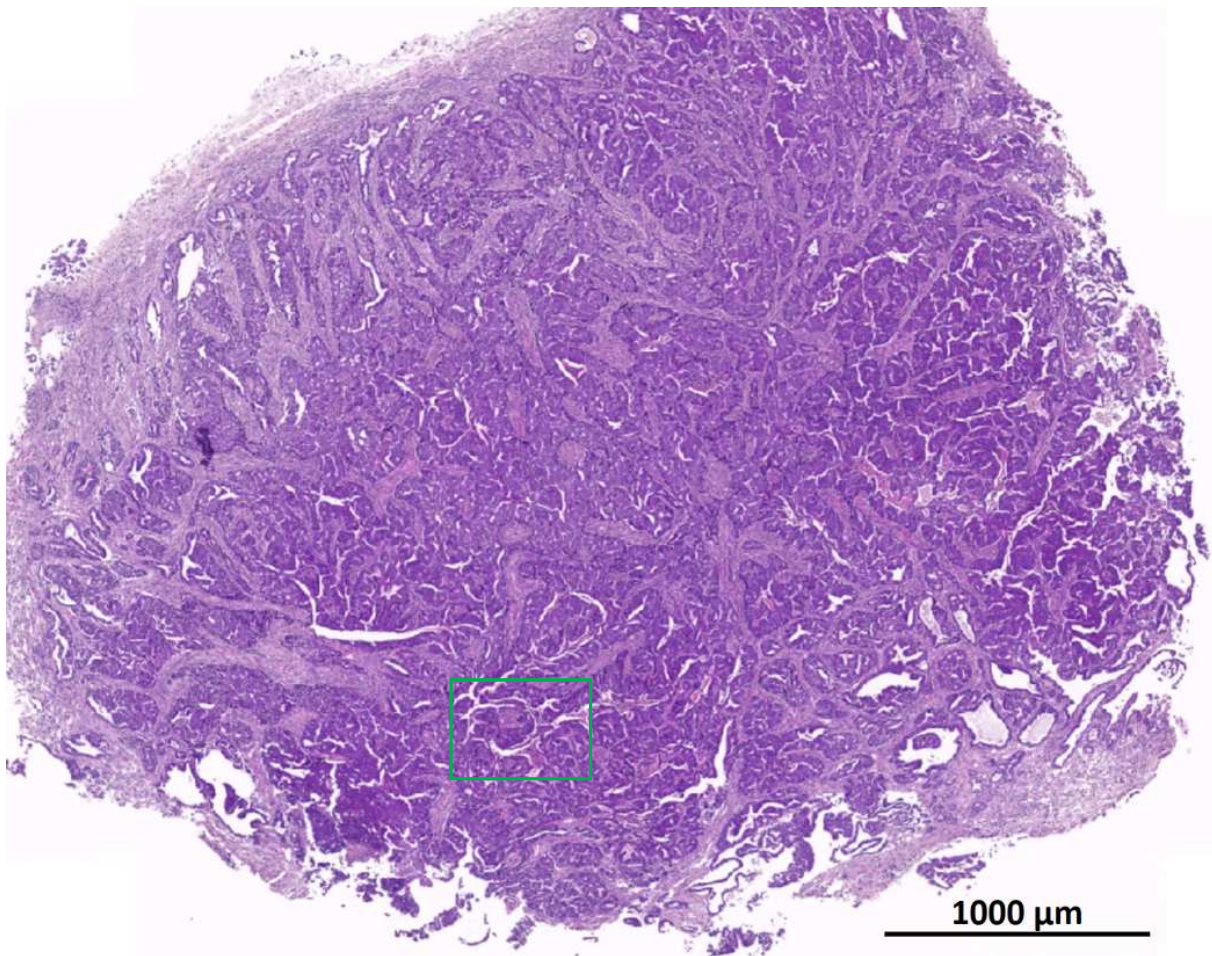


Red square: The tumor consists of ductular profiles developed in a dense fibroblastic tissue.



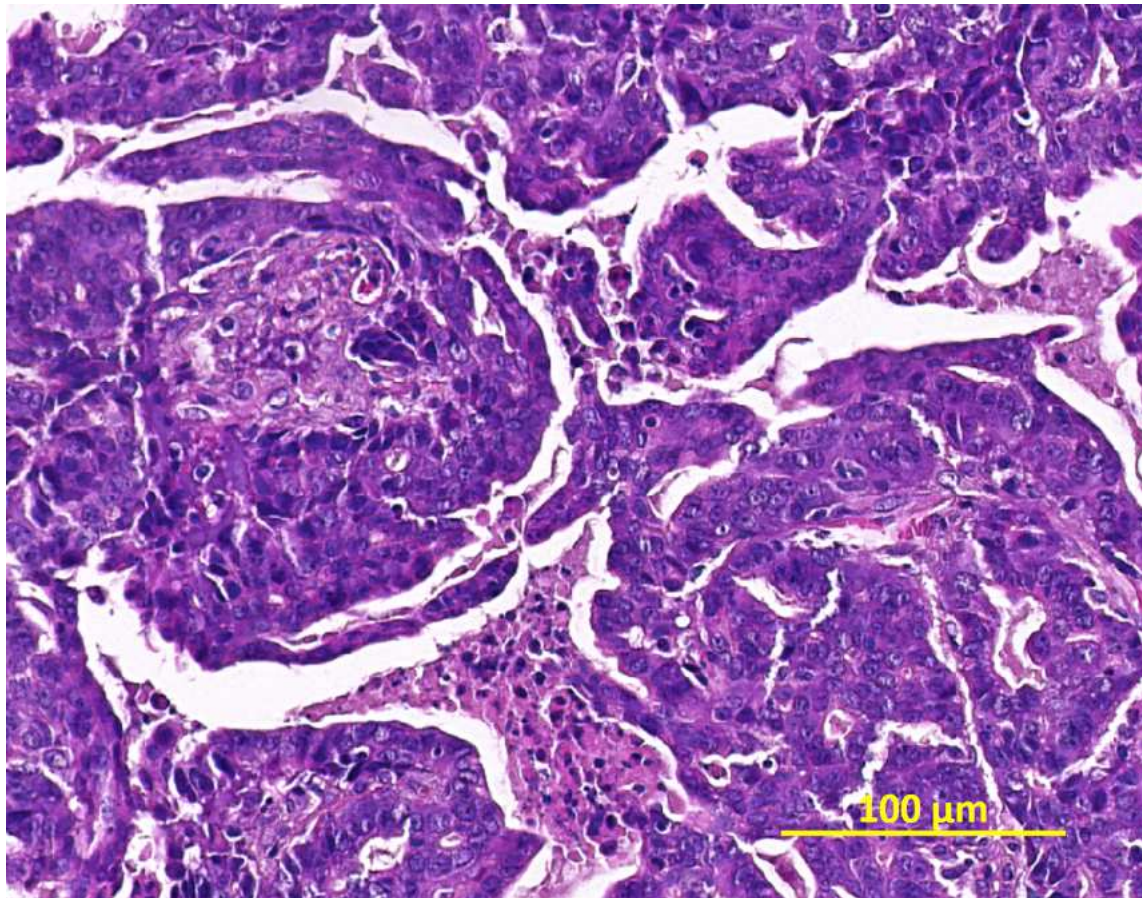
Green square: an example of individualized neoplastic cells in a vein (see **black arrow**) with a few red blood cells. On the right of the photo there is numerous small mononuclear cells, most compatible with small lymphocytes.

Figure 37: Lineage tumor aspect in subcutaneous tissue: example of **0005-17**



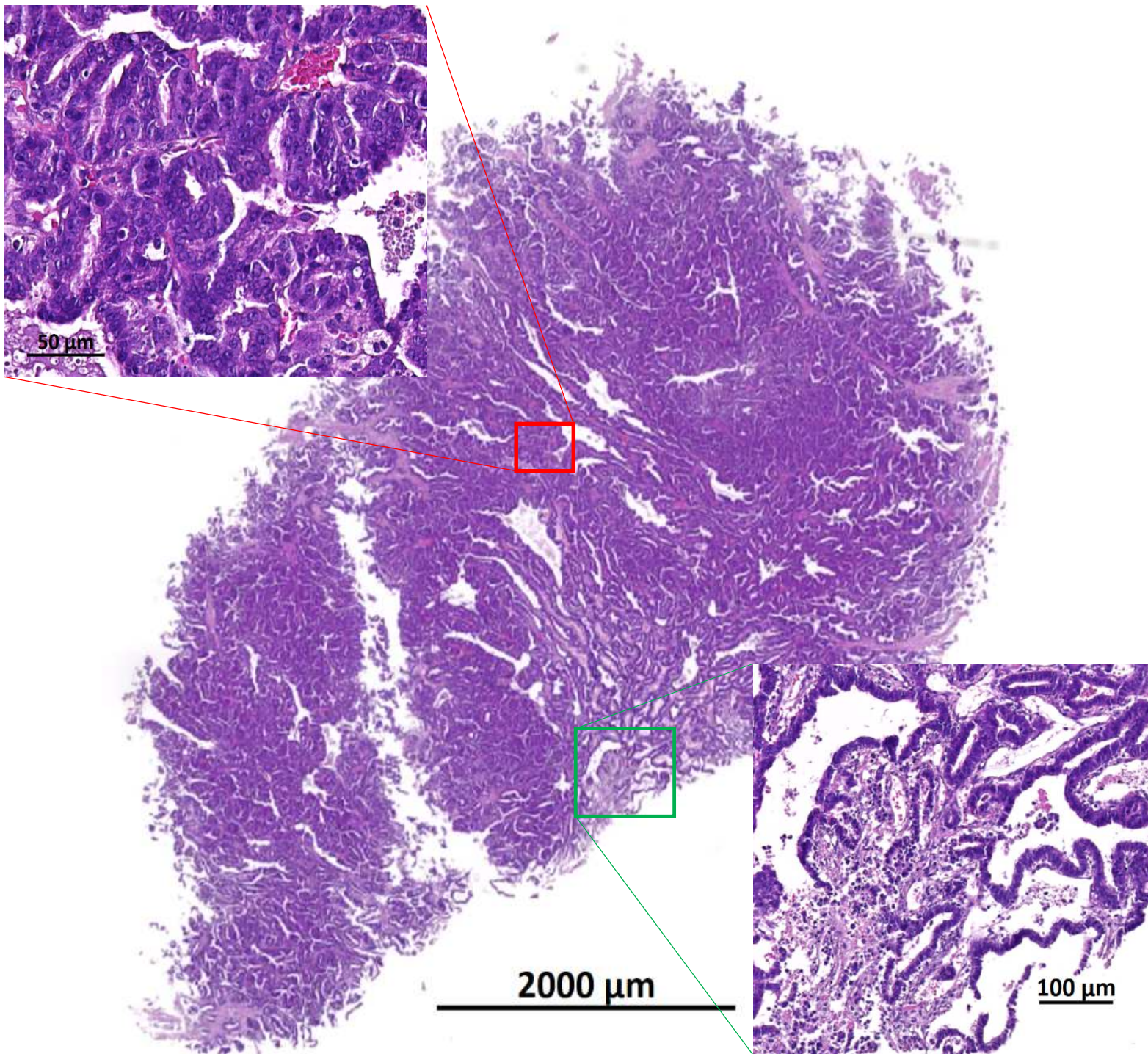
The neoplasm 005-17 is similar to neoplasm 0023-14 from the subcutis (see [Figure 36](#)), with a somewhat more papillo-tubular than tubular and less desmoplastic morphology **Source file:** 2019-02-04 15_42_24-10445_tu_rue__0023-14__0005-17.czi - ZEN 2.3 lite.png

Figure 38: Case 0005-17: High magnification reveals the tubulopapillary structure with necrotic cells in lumens and supportive stroma



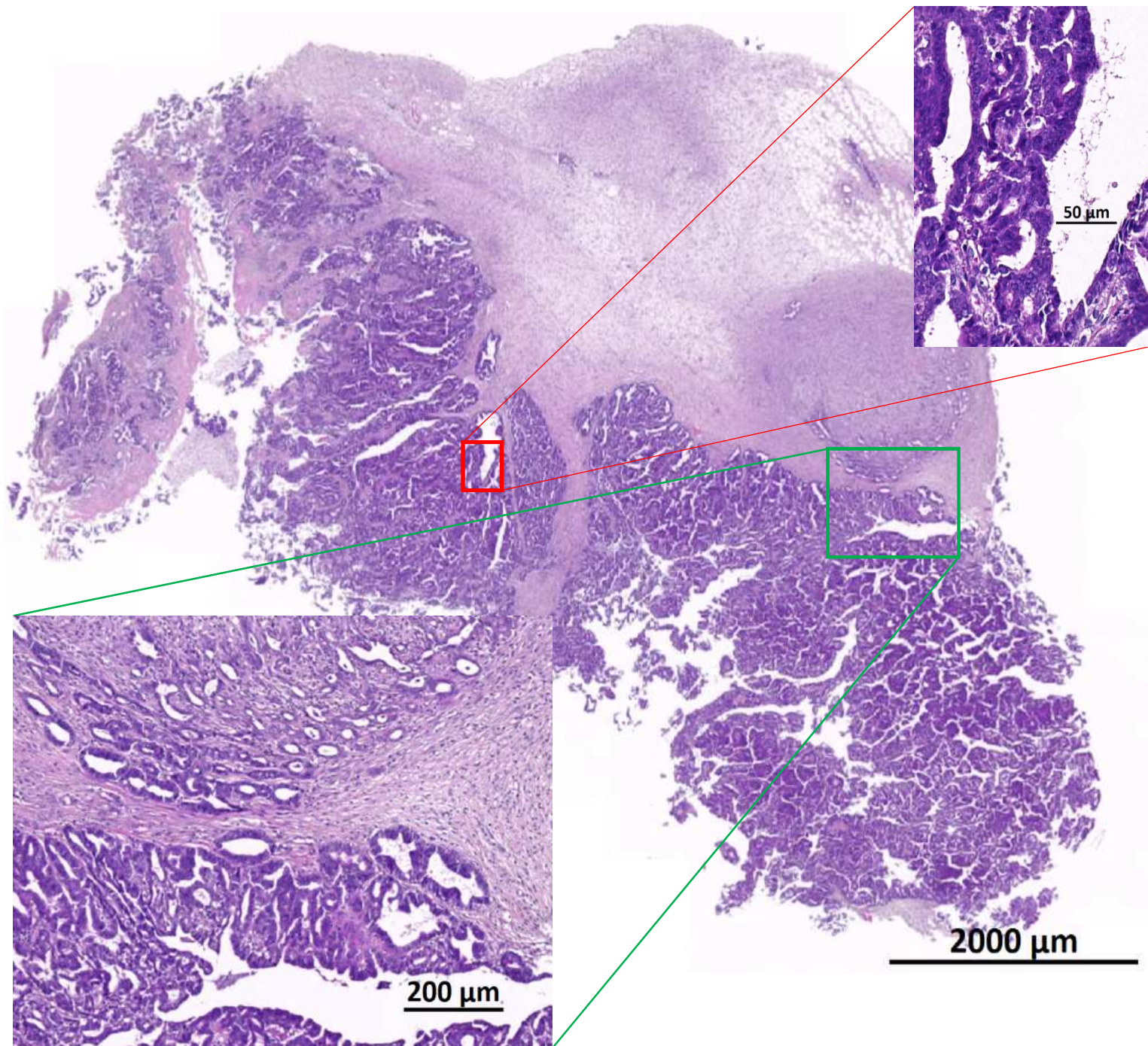
High magnification is more cellular than the index tumor from the subcutis (see [Figure 36](#)).

Figure 39: Lineage tumor aspect in kidney: example of **0001-17**



Notice the tumor aspect is very different from the renal tumor from the index case 0023-14 (see [Figure 35](#)) but similar morphologically to all other tumors from the lineage (see [Figure 38](#), [Figure 40](#), [Figure 41](#) and [Figure 42](#)), including the subcutaneous index mammary cancer ([Figure 36](#)). High magnification is identical to the lineage tumor 0005-17 ([Figure 38](#)). There is no evidence of normal renal tissue on the section examined. The tubulopapillary pattern is present, as well as the host immune response (see lower inset of the [green square](#))

Figure 40: Lineage tumor aspect in subcutaneous tissue: example of 1620-16



This daughter subcutaneous tumor is like all the tumors of the lineage, with however regions with more distinct desmoplasia and abundant lymphoid infiltration (see **green square** inset). Cytological aspect of the tubulopapillary proliferations are very similar in all the tumors from this lineage, indicating phenotypic stability.

Figure 41: Spontaneous neoplasms (study #10445): papillary cystic adenocarcinoma, female mouse 0547/17, hematoxylin and eosin stain, subcutis

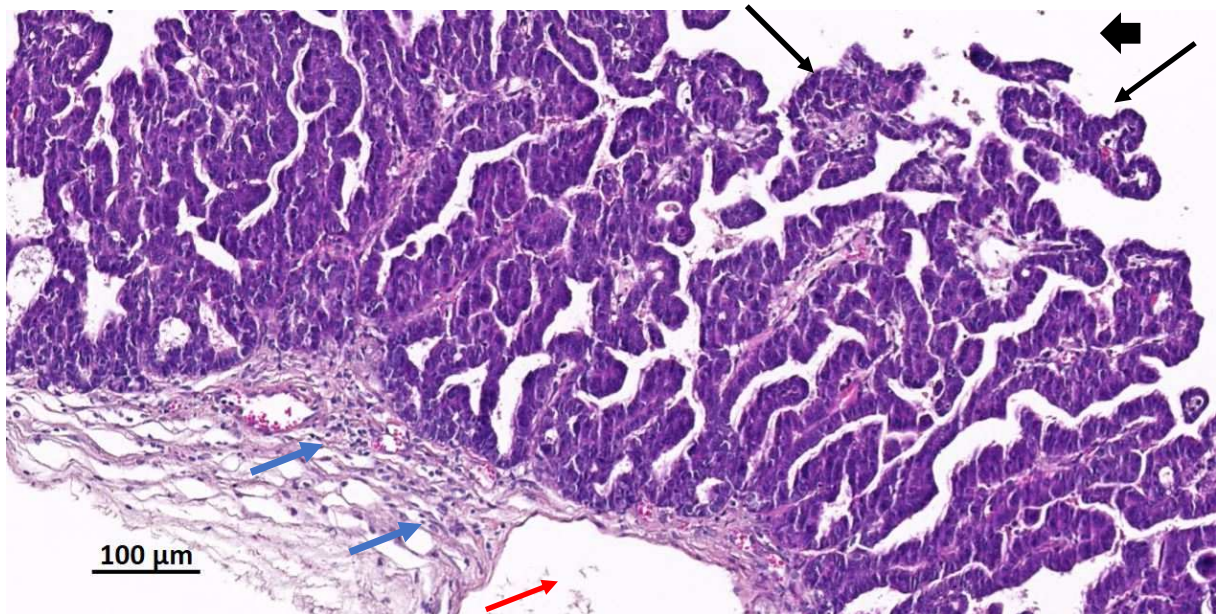


Image ID: 2017-10-25 15_23_04-TPL811_17_HE_10445_Tu_0547_17.czi - ZEN 2.3 lite

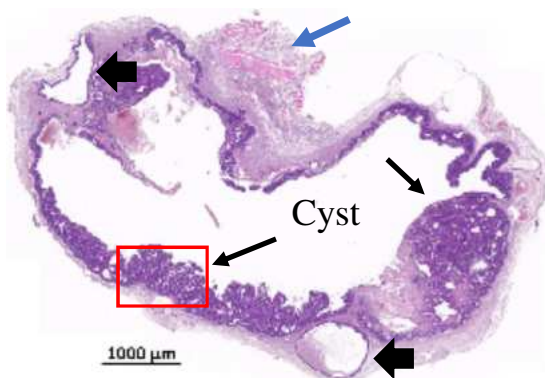
Index case: mouse ID number 023-14, strain C3H/HeJ ♀. Female C3H/HeJ 0547/17

The index case was previously studied in phase study TPL Path Labs TPL780-17.

The malignant proliferation is characterized by epithelial cell proliferation forming tubules and papillar (glandular) differentiation (**black arrows**), developed in a 6.8-millimeter long, multi-locular cystic cavity (arrowhead **◄**). Accompanying this epithelial malignant tumor of glandular origin are slight to moderate, stromal mononuclear leukocyte infiltrates, associating both small lymphocytes (**blue arrows**) and some macrophages. A lymphatic vessel is markedly dilated (**red arrow**).

Morphological diagnosis: Adenocarcinoma (Adk), papillary-cystic, mammary gland.

Low magnification of tumor aspect overview (thumbnail):



The **red rectangle** indicates the part of the cyst wall, which is depicted above at higher magnification.

Source photo file: 2017-10-25 14_55_01-TPL811_17_HE_10445_Tu_0547_17.czi - ZEN 2.3 lite

Low magnification view of tumor case ID # 0547. The neoplasia is developed in 7x4-mm cyst, with a multi-locular pattern (development of secondary cysts – see arrowheads **◄**).

Figure 42: Spontaneous neoplasms (study #10445): papillary cystic adenocarcinoma, female mouse 0544/17, skin

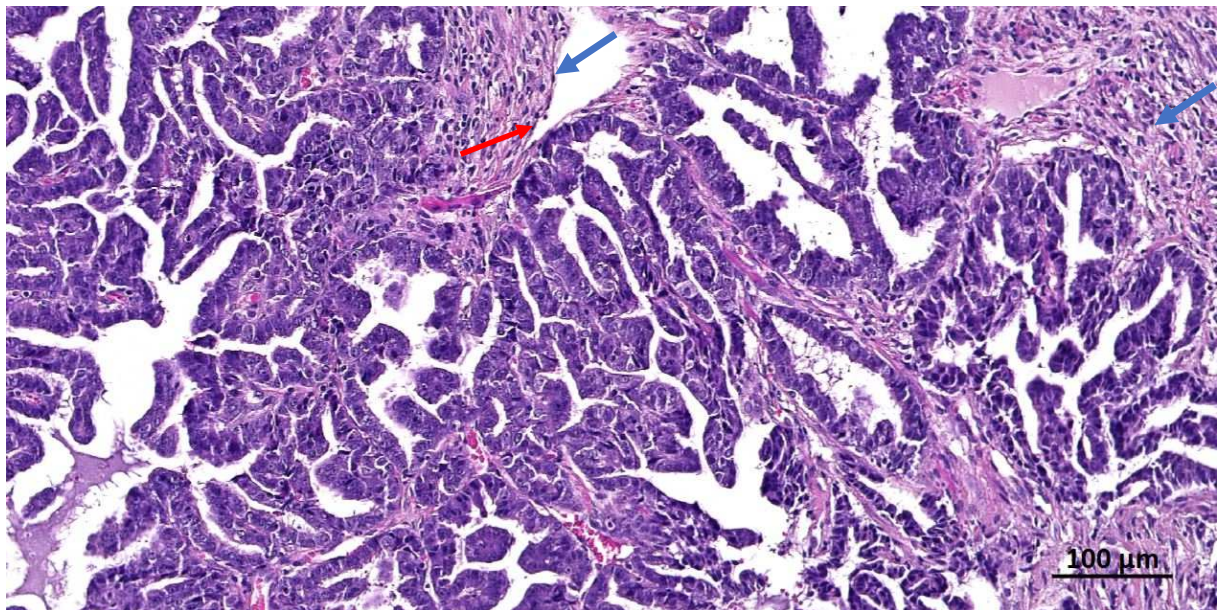


Image ID: 2017-10-25 15_20_49-TPL811_17_HE_10445_Tu_0544_17-Rotate-01 - ZEN 2.3 lite

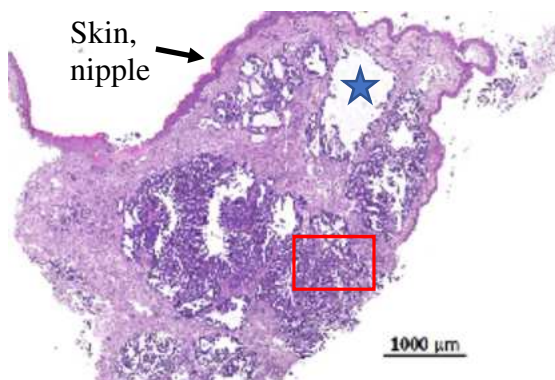
Index case: mouse ID number 023-14, strain C3H/HeJ ♀. Female C3H/HeJ 0544/17

Hematoxylin and eosin stain

Notice the striking similarity in morphology when comparing with neoplasms from animals 0001-17 or 0005-17 ([Figure 37](#), [Figure 38](#), [Figure 39](#)) to 0547/17 (see [Figure 41](#)). Stromal infiltration with mononuclear cells is of similar nature and degree (**blue arrows**). Stroma also has similar levels of tumor-infiltrating lymphocytes (TIL). Although rather well differentiated, this neoplasm is clearly malignant, with good seeding potential, with also compression related dilated lymphatic vessels (**red arrow**). Cytological features of this tumor and the ones from all JA0023 derived tumors are very similar, near identical. The neoplasm is strikingly invasive in the adjacent stroma (not shown).

Morphological diagnosis: Adenocarcinoma (AdK), papillary-cystic, skin, mammary gland.

Low magnification of tumor aspect overview (thumbnail):



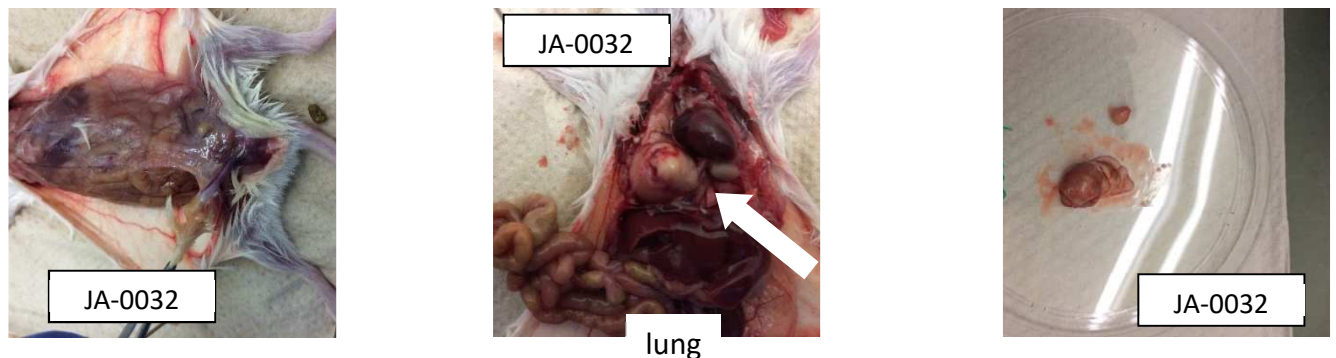
The **red rectangle** indicates the part of the tumor, which is depicted above at higher magnification.

Source photo file: 2017-10-25 15_08_41-TPL811_17_HE_10445_Tu_0544_17-Rotate-01 - ZEN 2.3 lite

At sub-gross examination, this ~ 3.6-mm thick tumor is developed in several multi-lobulated dilated or cystic (★) spaces, composed of tubule and papillary proliferations.

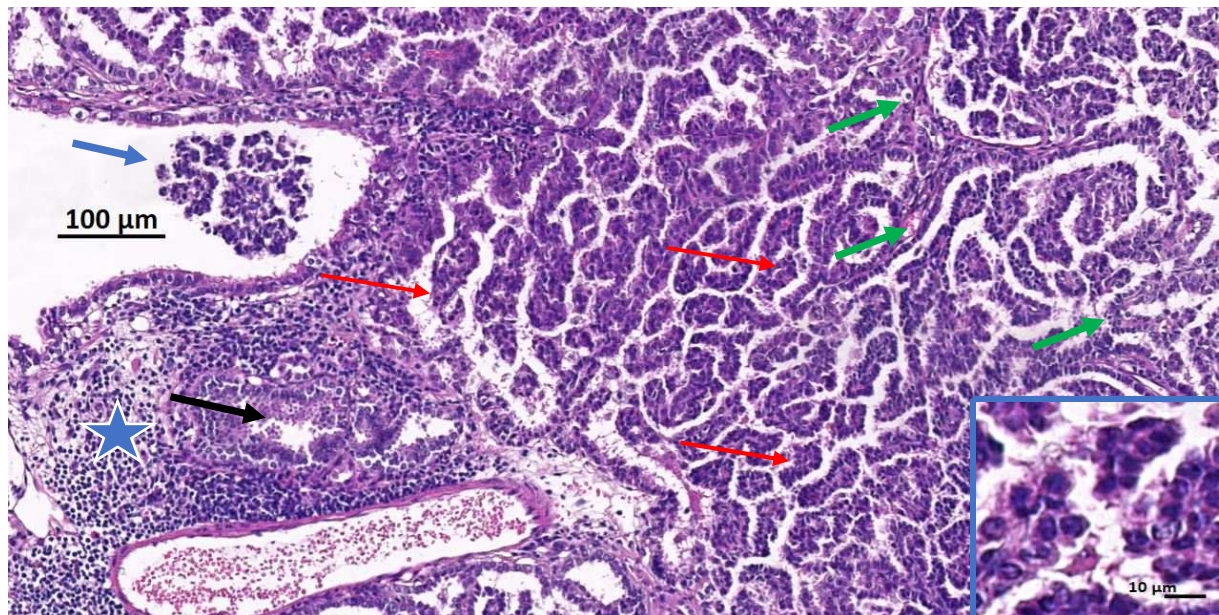
JA-0032 sMDI: Adenocarcinoma, Lung

JA-0032/ 0055-17 (Fig. 3). The original index sample was identified as a typical bronchiolo-alveolar papillary adenocarcinoma



Adenocarcinoma, papillary, lung

Figure 43: Spontaneous neoplasms (study #10445): papillary adenocarcinoma, lung, male mouse 0032/14



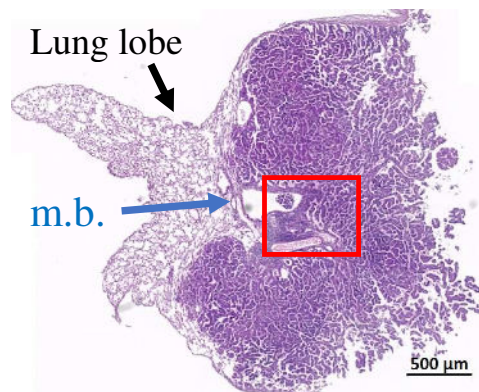
Index case: mouse ID number 0032-14, strain BALB/c, sex ♂.

Developed and invading the alveolar parenchyma are small cords, festoons and papillary structures supported by a delicate stroma, composed of mid-sized (~ 10 μm) cuboidal cells resembling type II pneumocytes (see **inset** and **red arrows**). This proliferative alveolar tissue invades the nearby main bronchus (**blue arrow**). The pre-existing alveolar walls, obscured by the proliferative tissue, as well as the delicate stroma induced by the neoplastic tissue is variably thickened by collagenous tissue and infiltrated by moderate numbers of small mononuclear cells (**green arrows**). The BALT has moderate lymphoid depletion (★) and focal invasion by neoplasm (**black arrow**).

Image ID: 2017-10-25 15_17_08-TPL811_17_HE_10445_Tu_32_15_3_4_17_Lu.czi - ZEN 2.3 lite

Morphological diagnosis: Adenocarcinoma (AdK), papillary-cystic

Low magnification of tumor aspect overview (thumbnail):



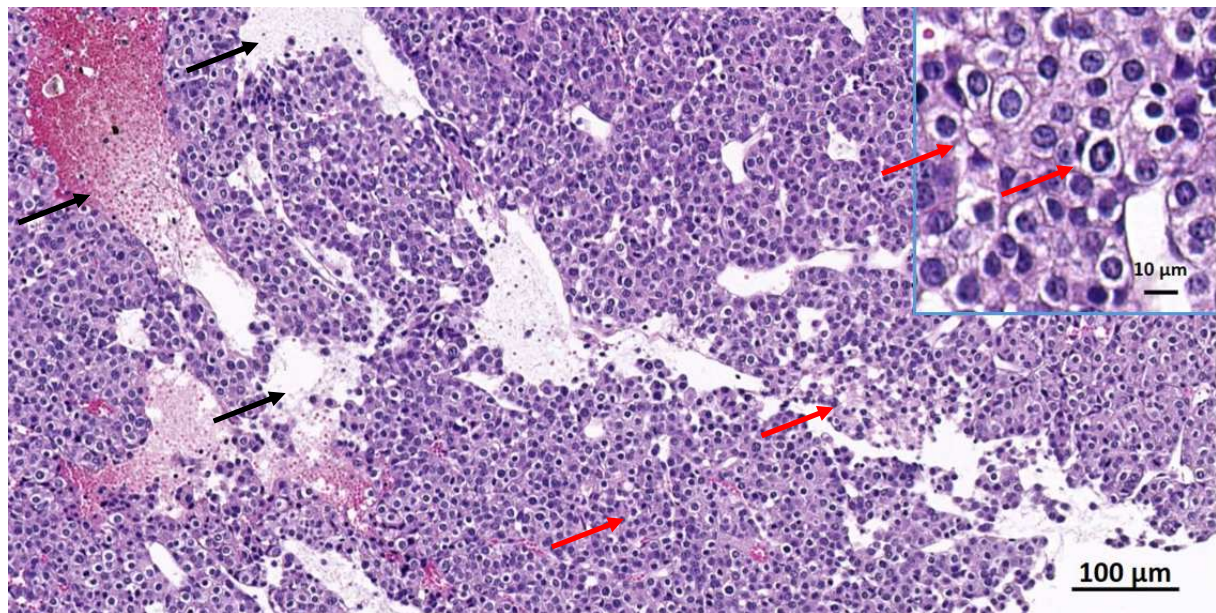
The **red rectangle** indicates the part of the neoplasm, which is depicted above

Blue arrow, **m.b.** = main bronchus

Source photo file: 2017-10-25 15_15_07-TPL811_17_HE_10445_Tu_32_14_3_4_17_Lu.czi
- ZEN 2.3 lite

At sub-gross examination, this ~ 3.5-mm long neoplasm is developed in several multi-lobulated dilated or cystic () spaces, composed of tubule and papillary proliferations.

Figure 44: Spontaneous neoplasms (study #10445): adenocarcinoma, solid, clear cells, subcutis, male mouse 0055/17



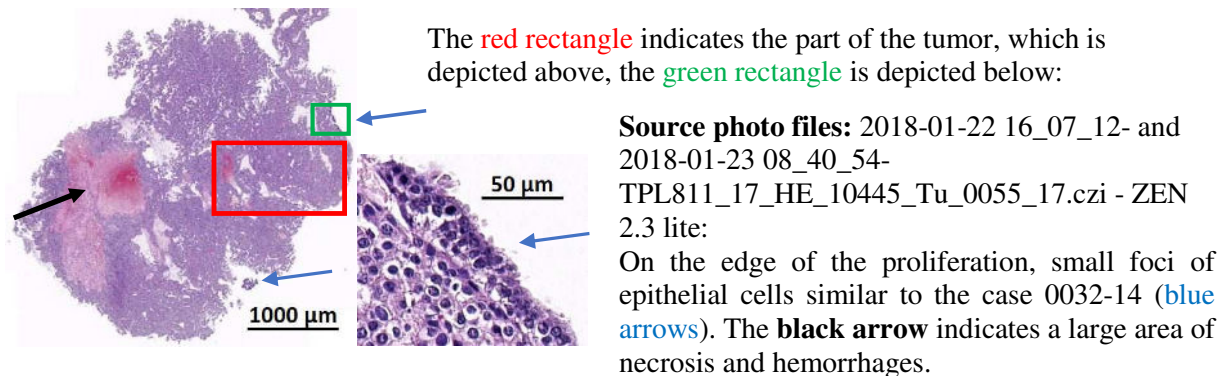
Source: 2017-10-25 15_19_23-TPL811_17_HE_10445_Tu_0055_17.czi - ZEN 2.3 lite

Index case: mouse ID number 0032-14, strain BALB/c, sex ♂

This case is not straightforward because the aspect of the source index case (see [Figure 43](#)) is morphologically very different from this derived one: in male 055/17, there is solid very fragile (due to nearly absent supportive stroma and secondary tearing and hemorrhage – see **black arrows**) solid proliferation of mid-sized ~ 10 μm polyhedral to cuboidal epithelial cells with characteristically clear (“rarefied”) cytoplasm (see **red arrows**). Anisopoikilocytosis and nuclear variability are slight to moderate. This tumor is developed in the subcutis, locally when transplanted.

Morphological diagnosis: Adenocarcinoma (Adk), solid, clear cells, subcutis.

Figure 45: Low magnification of tumor aspect overview and high view detail (**thumbnails**)



Comments on JA-0032 sMDI:

This tumor from 0055-17 is most probably derived from the index lung Adk. The clear cell aspect most probably is to be related to surfactant secreting type II pneumocytes - IHC would be useful to prove this hypothesis. Standard HE histology cannot prove it.

This situation is a frequent encounter, when the sites of grafting is different from the original organ of origin. An orthotopic (matching site in the lung) engraftment would be desirable if one is willing to recreate the original morphology (see the recent publication in [Reference 2](#) for the pancreatic cancer situation.

In this particular case, if further used in research and development, orthotopic engraftments would be highly recommended, although heterotopic (ectopic) may be used, as long as the presence of key characteristics such as the surfactant and areas of alveolar morphology can be demonstrated

Literature cited:

[Reference 1](#) James E. Talmadge, Marc E. Key and Ian R. Hart, 1981; "Characterization of murine ovarian reticulum cell sarcoma of histiocytic origin" May 1981 *Cancer Research* vol. 41(4):1271-80

[Reference 2](#): Wanglong Qiu, and Gloria H Su. 2013; "Development of orthotopic pancreatic tumor mouse models" *Methods in molecular biology (Clifton, N.J.)* vol. 980 (): 215-23. <https://www.ncbi.nlm.nih.gov/pmc/articles/PMC4049460/>

1.4 Doc. S2-sMDI - Material, Methods & Results: Efficacy studies with anti-mPD-1 and anti-mCTLA-4 in seven syngeneic standard mouse tumor models

Implantation protocol for efficacy studies using immune checkpoint antibodies for cell line-based syngeneic tumor models: Cells from tissue culture were washed twice and suspended in PBS. On day 0 between 1×10^5 and 1×10^6 colon carcinoma cells MC38-CEA (CPQ 449*) in female C57BL/6N, colon carcinoma cells CT26.WT (CPQ 238) in female BALB/c, lung carcinoma cells LL/2 (CPQ 423) in female C57BL/6N, melanoma Clone M3 cells (CPQ 422) in female DBA/2N, mamma carcinoma 4T1 cells (CPQ 272) in female BALB/c, renal carcinoma RENCA cells (CPQ 307) in female BALB/c, and melanoma B16.F10 cells (CPQ 365**) in female C57BL/6N were injected subcutaneously according the respective tumor model.

*Cell lines are stock of ProQinase GmbH, In Vivo Pharmacology (CPQ-numbered), and derived from ATCC, LGC Standards GmbH, Germany. Carcinoembryonic Antigen (CEA) transfected MC38-CEA were kindly provided from Joanna Bereta, PhD, Jagiellonian University, Krakow, Poland. **B16.F10 cells were regularly selected for high metastatic capacity by i.v. application to induce *in vivo* metastases, followed by *in vitro* re-culturing of lung metastasis [1].

Study design for efficacy studies using immune checkpoint antibodies for cell line-based syngeneic standard tumor models: Mice were implanted with above mentioned cell lines according implantation protocol. Tumor sizes were calculated according to the formula $W^2 \times L / 2$ (L= length and W= the perpendicular width of the tumor, $L > W$). When mean tumor size achieved a volume of about 100 - 200 mm³, tumor-bearing animals were randomized (between days 4 – 20 – according respective tumor model) into 3 groups of 8 - 12 animals. For randomization, a robust automated random number generation within individual blocks was used (MS-Excel 2016).

Results are shown in Figure S1. Both colon carcinoma models, MC38-CEA and CT26.WT were significantly sensitive to anti-ICPI treatment: MC38-CEA growth was significantly reduced both, by anti-mCTLA-4 and anti-mPD-1 treatment. Growth of CT26.WT was significantly reduced by anti-mCTLA-4 treatment but showed only a non-significant reduction by anti-mPD-1 treatment. The other cell line-based syngeneic tumor standard models displayed no or no significant inhibition. A reduction of tumor growth that was not significant was observed in Clone M3 for treatment with anti-mCTLA4 antibodies and in B16.F10 for treatment with anti-mPD-1 treatment.

The strong inhibition of MC38-CEA contrasts with results of others [2], not seeing any effects by anti-ICPI antibodies in the MC38 model which probably results from transfection with CEA which acts as potential neoantigen in the cells (see also Doc. S2 and Fig. S2). As demonstrated by flow cytometry, the number and subpopulations of tumor-infiltrating immune cells does already differ in the two model subvariants (Fig. 4b) and [2]. Probability (P) was tested with parametric unpaired t test (GraphPad Prism 5.04) compared to PBS vehicle control. Differences were determined as not significant with $ns > 0.050$ and significant * with $p < 0.050$, ** with $p < 0.010$, or *** with $p < 0.001$.

1.5 Fig. S2- sMD - Efficacy studies with anti-mPD-1 and anti-mCTLA-4 in seven syngeneic standard mouse tumor models

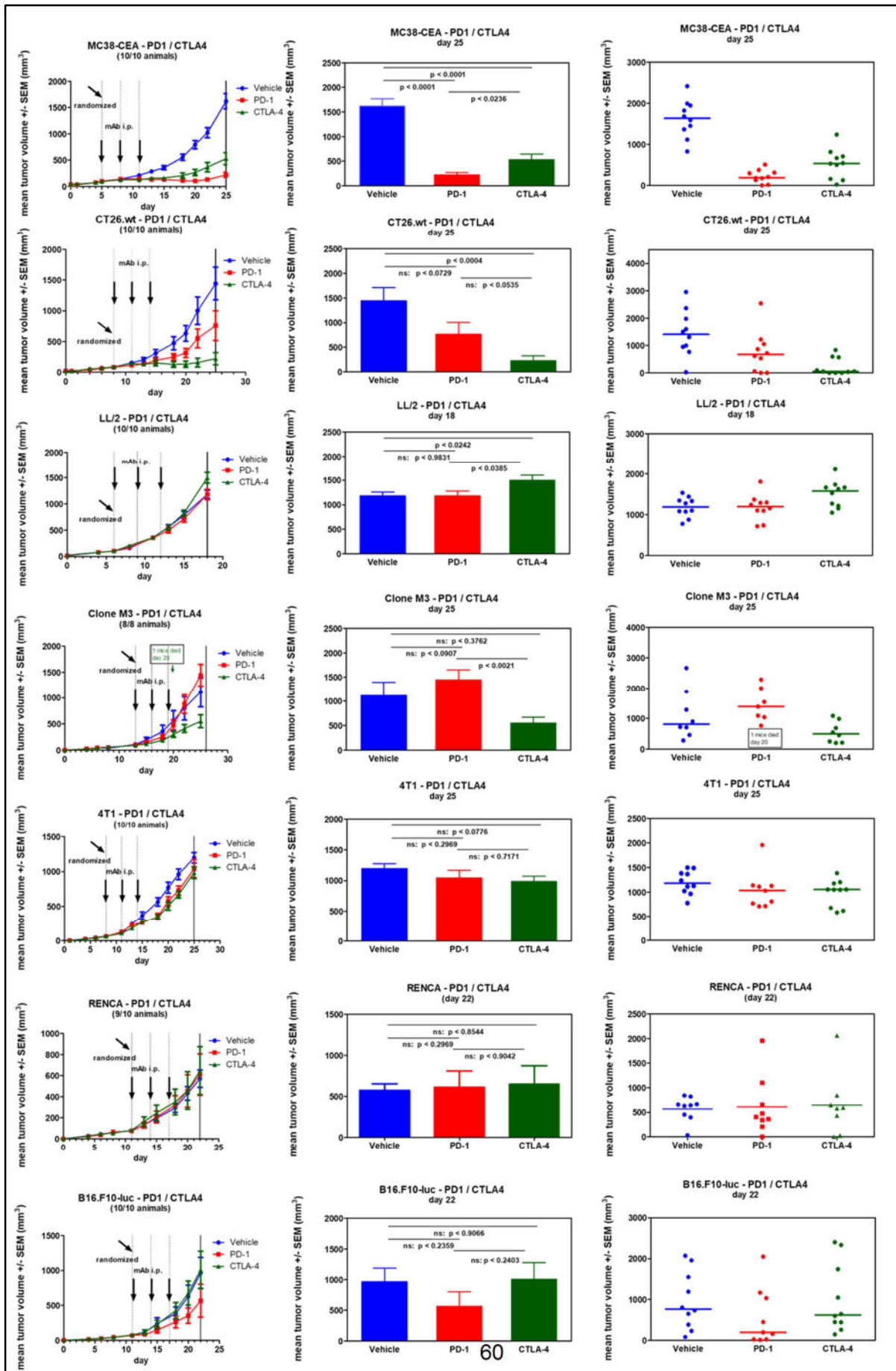


Fig. S1-sMDI - Efficacy of anti-ICPI antibodies in seven established syngeneic standard mouse tumor models

The tumors cells of colon carcinoma MC38-CEA, colon carcinoma CT26.WT, lung carcinoma LL/2, melanoma Clone M3, mamma carcinoma 4T1, renal carcinoma RENCA, and melanoma B16.F10 were each implanted subcutaneously into mice. Animals were randomized at tumor volumes of 100 - 200 mm³ between days 5 - 13 according to the respective model into 8 mice per group. Mice were treated three times (dotted lines) i.p. with anti-ICPI antibodies and PBS as vehicle control: vehicle – blue (10 ml/kg), anti-mPD-1 – green (10 mg/kg), and anti-mCTLA-4 – red (10 mg/kg). Tumor volumes are shown as growth curve (curve chart), mean of groups (bar graphs), and individual values of single mouse per group (dot plots). Probability (P) was tested with parametric unpaired t test (GraphPad Prism 5.04) compared to PBS vehicle control. Differences were determined as not significant with ns > 0.050 and significant * with p < 0.050, ** with p < 0.010, or *** with p < 0.001.

1.6 Doc. S3-sMDI - Material, Methods & Results: Establishment, efficacy and characterization of mPD-1-resistant MC38-CEA relapsed subline

Establishment of MC38-CEA-PD1-res: A PD-1-resistant subline of MC38-CEA was established (Fig. S2A) from mouse 0007-15 which was part of the comparative study of seven standard syngeneic *in vivo* mouse tumor models (Fig. S1). The MC38-CEA tumor was completely regressed by 3-fold anti-mPD-1 treatment after day 25. Extended monitoring of this mouse showed weak, but again spontaneously regressing tumor growth between days 30 - 40. A striking relapse started with day 50. Re-treatment with mPD-1 starting on day 60 did no longer inhibit, in contrast to primary treatment (Fig. S1), tumor growth during further monitoring (Fig. S2A). On day 88 the mouse was sacrificed, tumor was removed sterile, cut into small pieces and cultured with RPMI 1640 medium in petri dishes. From outgrowing cells, a stable cell line was established by *in vitro* culture, frozen stored and designated as mPD-1-resistant MC38-CEA (MC38-CEA-PD1-res).

Implantation protocol and study design: Implantation and study design for MC38-CEA-PD1-res cell line was performed according the MC38-CEA protocols as described in Doc.S1-sMDI

Efficacy testing of MC38-CEA-PD1-res tumors: mPD1 resistant MC38-CEA cell line was implanted day 0. Since growth of the resistant cells was delayed compared to parental cells, randomization at tumor volumes of 40 - 80 mm³ in 8 animals per group was performed only on day 13 (versus day 5 in parental cells – Fig. S2B). Starting on randomization day, mice with relapse-derived, MC38-CEA-PD-1 resistant tumors (Fig. S2C 1-3) were treated three times (dotted lines) i.p. with anti-ICPI antibodies and PBS as vehicle control: vehicle – blue (10 ml/kg), anti-mPD-1 – green (10 mg/kg), and anti-mCTLA-4 – red (10 mg/kg). As shown in Figs. S2C growth of the PD1-resistant tumors was insensitive to renewed mPD-1 treatment till day 25. Although anti-mCTLA-4 antibodies showed an about 50 % reduction of growth, also this difference was not significant. In contrast, parental colon carcinoma MC38-CEA was sensitive to mPD-1 as well as mCTLA-4 treatment (Fig. S2B). Probability (P) was tested with parametric unpaired t test (GraphPad Prism 5.04) compared to PBS vehicle control. Differences were determined as not significant with ns > 0.050 and significant * with p < 0.050, ** with p < 0.010, or *** with p < 0.001.

Flow cytometric analysis: Expression of Carcinoembryonic Antigen (CEA) in transfected MC38-CEA and PD1-resistant MC38-CEA-PD1-res cells was compared using a panel of CEA-specific or CEA-family specific (13H10, HD11, CC11, AH119 or control (anti-PD-L1) antibodies [3,4] according flow cytometric analysis performed in the main paper. FACS buffer was used as vehicle control. The data clearly show that mPD-1-res MC38-CEA cells do actually express lower amount or no CEA anymore, whereas the parental cells express. Since ATCC MC38 was not anti-mPD-1 sensitive [2], we assume that probably CEA was the neoantigen on MC38 tumors, which was targeted by anti-mPD-1 treatment in MC38-CEA parental cells. Loss of this antigen made the cells insensitive to anti-mPD-1 immunotherapy. If the insignificant effect of mCTLA-4 also results from reduced CEA expression or might result from the fact that tumor volume in the vehicle group of mPD-1 resistant cells was only a half of tumor volume of parental cells at study end on day 25, remains to be verified.

Conclusion: Long-term observation of e.g. immuno- or chemotherapeutic treatment-dependent tumor regression as well as relapse later on, opens possibilities to establish actually therapy resistant sublines or -models, e.g. potential therapy-resistant MDI-models. This provides new possibilities to test clinically relevant concepts against tumors getting therapy resistant.

1. Jantscheff, P.; Schlesinger, M.; Fritzsche, J.; Taylor, L.A.; Graeser, R.; Kirfel, G.; Furst, D.O.; Massing, U.; Bendas, G. Lysophosphatidylcholine pretreatment reduces VLA-4 and P-selectin-mediated B16.F10 melanoma cell adhesion in vitro and inhibits metastasis-like lung invasion in vivo. *Mol Cancer Ther* 2011, 10, 186-197.
2. Mosely, S.I.; Prime, J.E.; Sainson, R.C.; Koopmann, J.O.; Wang, D.Y.; Greenawalt, D.M.; Ahdesmaki, M.J.; Leyland, R.; Mullins, S.; Pacelli, L., et al. Rational selection of syngeneic preclinical tumor models for immunotherapeutic drug discovery. *Cancer Immunol Res* 2017, 5, 29-41.
3. Jantscheff, P.; Bottger, V.; Price, M.; Micheel, B.; Kaiser, G.; Zotter, S.; Kotzsch, M.; Grossmann, H.; Karsten, U. Production and characterization of monoclonal antibodies against carcinoembryonic antigen (cea). *Biomed Biochim Acta* 1991, 50, 1261-1267.
4. Jantscheff, P.; Terracciano, L.; Lowy, A.; Glatz-Krieger, K.; Grunert, F.; Micheel, B.; Brummer, J.; Laffer, U.; Metzger, U.; Herrmann, R., et al. Expression of ceacam6 in resectable colorectal cancer: A factor of independent prognostic significance. *J Clin Oncol* 2003, 21, 3638-3646.

1.7 Fig. S3– sMDI - Establishment, efficacy and characterization of mPD-1-resistant MC38-CEA subline with anti-ICPI antibodies in syngeneic standard mouse tumor models

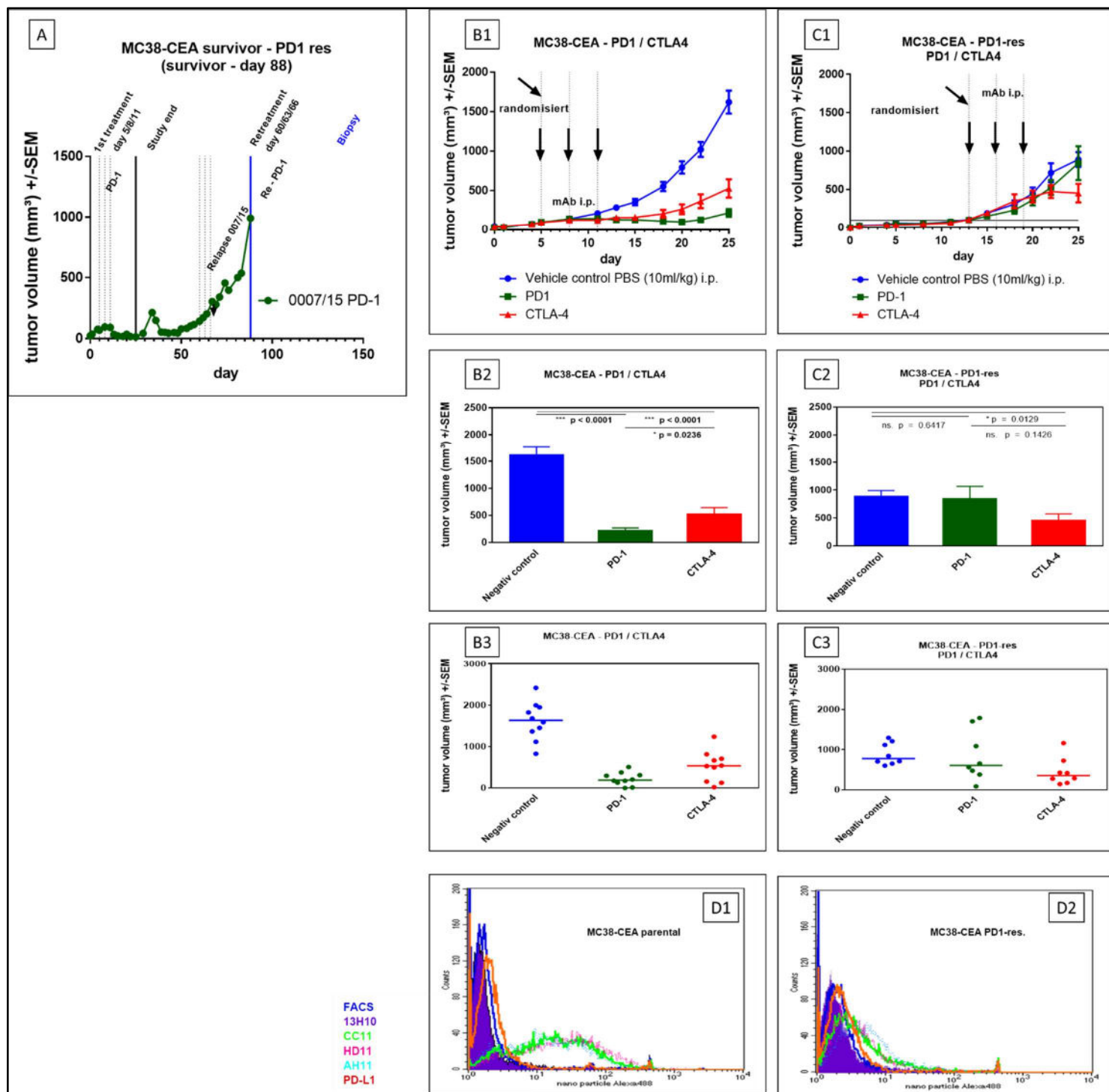


Fig. S2-sMDI - Establishment, efficacy and characterization of mPD-1-resistant MC38-CEA subline with anti ICPI antibodies in syngeneic standard mouse tumor models

Long-term observation of anti-mPD1 treatment caused regression of subcutaneous MC38-CEA colon carcinoma tumor growth in C57BL/6N female mouse 0007-15*, showed striking relapse with day 50 (A). Whereas MC38-CEA parental cells were sensitive to mPD1 as well as CTLA-4 treatment (B), newly established cell line MC38-CEA-PD1-res was insensitive (C) to three-fold (dotted lines) i.p. treatment with anti-ICPI antibodies, compared with PBS as vehicle control [vehicle (10 ml/kg), anti-mPD-1 (10

mg/kg), and anti-mCTLA-4 (10 mg/kg)]. Parental MC38-CEA (D1) and resistant subline (D2) also displayed striking different surface CEA expression as determined by flow cytometry analysis.

*Mouse 007/15 was part of the comparative study of seven standard syngeneic *in vivo* mouse tumor models which is shown in Fig. S1